

**ADAPTIVE ALGORITHMS FOR SPARSE
CHANNEL ESTIMATION FOR MILLIMETER
WAVE HYBRID MIMO SYSTEMS**

Ph.D. Thesis

by

VIDYA BHASKER SHUKLA



**DEPARTMENT OF ELECTRICAL ENGINEERING
INDIAN INSTITUTE OF TECHNOLOGY
INDORE**

May, 2024

**ADAPTIVE ALGORITHMS FOR SPARSE
CHANNEL ESTIMATION FOR MILLIMETER
WAVE HYBRID MIMO SYSTEMS**

A THESIS

*Submitted in partial fulfillment of the
requirements for the award of the degree*

of

DOCTOR OF PHILOSOPHY

by

VIDYA BHASKER SHUKLA



**DEPARTMENT OF ELECTRICAL ENGINEERING
INDIAN INSTITUTE OF TECHNOLOGY
INDORE**



INDIAN INSTITUTE OF TECHNOLOGY INDORE

CANDIDATE'S DECLARATION

I hereby certify that the work which is being presented in the thesis entitled “**ADAPTIVE ALGORITHMS FOR SPARSE CHANNEL ESTIMATION FOR MILLIMETER WAVE HYBRID MIMO SYSTEMS**” in the partial fulfillment of the requirements for the award of the degree of DOCTOR OF PHILOSOPHY and submitted in the DEPARTMENT OF ELECTRICAL ENGINEERING, Indian Institute of Technology Indore, is an authentic record of my own work carried out during the time period from July 2019 to May 2024 under the supervision of Prof. Vimal Bhatia, Professor, Indian Institute of Technology Indore, India.

The matter presented in this thesis has not been submitted for the award of any other degree of this or any other institute.

May 20, 2024

Signature of the student with date
(VIDYA BHASKER SHUKLA)

This is to certify that the above statement made by the candidate is correct to the best of my knowledge.

Signature of Thesis Supervisor with date
(Prof. VIMAL BHATIA)

Vidya Bhasker Shukla has successfully given his Ph.D. Oral Examination held on September 19, 2024.

Signature of Thesis Supervisor with date
(Prof. VIMAL BHATIA)

ACKNOWLEDGEMENTS

There is always a sense of gratitude with which one expresses an offer for the helpful and needy services someone renders during all the phases of life. First of all, I would like to thank the almighty God because he choose this esteemed institute for me, without whose blessings I could never achieve this milestone.

I express my sincere gratitude to my Ph.D. supervisor Prof. Vimal Bhatia for his motivation, guidance, and continuous support throughout my thesis work. I am thankful for all the freedom he gave me to explore various research topics and was always available for discussion despite his busy schedule. I would also like to thank my PSPC committee members Prof. Mukesh Kumar and Prof. Neminath Hubballi for their fruitful discussions and suggestions towards my research.

I would like to thank the IIT Indore and Chankya fellowship project proposal titled “CFP/2022/077 - Performance Improvement of IRS-Assisted Millimeter Wave MIMO for IoT and its Applications” Fellowship Program 2022-23 by IIT Bombay for providing financial assistance.

I am truly thankful to all the faculty members and the staff of IIT Indore for their invaluable cooperation throughout my thesis work. I would also like to thank all the members of the Signal and Software group (SaSg) for their encouragement and support that helped me to face the hard phase of my life and never let me feel lonely along this long journey. Specially, I would like to extend my appreciation to my seniors Dr. Rangeet Mitra, Dr. Abhijeet Bishnu, Dr. Praveen Kumar Singya, Dr. Mahendra Singh Thakur, and Dr. Shaik Parvez who helped me every time wherever I required. I would like to thank my friends Deepak Kumar, Justin Jose, Abhinav Singh Parihar, Vaishali Sharma, Shubham Bisen, Anupma Sharma, Amit Baghel, and other colleagues who helped me in several ways during my thesis work.

Moreover, whatever little I have achieved in my life, the credit goes to my teachers and family members: my mother, my maternal uncle, my in-laws, my sister, my wife and my lovely sons whom I take great pride in dedicating this thesis. They have always been a source of inspiration for me and have kept trust and faith in whatever I did.

VIDYA BHASKER SHUKLA

Dedicated to my family

ABSTRACT

With the increase in high-speed data demand and lower latency for upcoming fifth-generation (5G) and beyond communication systems, millimeter-wave (mmWave) multiple-input multiple-output (MIMO) has emerged as one of the promising physical layer technique for existing radio frequency (RF) communication systems. Although promising, it suffers from much greater attenuation compared to conventional cellular bands (sub-6 GHz band) due to penetration losses, reflection, and signal atmosphere. However, thanks to the short wavelength of mmWave signals, large antenna arrays can be packed into a small area. Hence, a large number of antennas can be adopted at both the transmitter and receiver to provide significant beamforming gains. However, the large number of antennas makes fully digital beamforming (in which each antenna is connected with a separate RF chain) impractical due to the huge power consumption caused by devices operating at radio frequency (RF). Therefore, hybrid (combination of analog and digital) architectures have been proposed, which can reduce hardware costs and power consumption with a reduced number of RF chains.

Due to the hybrid architecture and the large number of antennas, it is difficult to obtain the channel state information (CSI), which is crucial for obtaining desirable beamforming gains. Further, due to high blockage and lower scattering, the mmWave channel is sparse, meaning that impulse responses are dominated by a small number of clusters of significant paths. Hence, this thesis develops a novel sparse adaptive online channel estimator (signifying that the estimator continually adapts to changes in the input data stream as it is received, rather than processing the entire dataset at once as a block update) based on the zero attractor least mean square (ZALMS) algorithm for mmWave hybrid MIMO systems. In this algorithm, l_0 and l_1 norm penalties are introduced in the least mean square (LMS) algorithms, which introduces a zero attractor in the LMS weight update recursion. This process shrinks the coefficients of inactive taps and hence reduces the steady-state mean square error (MSE) floor, consequently increasing the estimation accuracy and maximizing the overall spectral efficiency (SE) of mmWave hybrid MIMO systems.

Commonly, to make mmWave hybrid MIMO systems cost-effective and power-efficient, generally inexpensive components are deployed, which lead to hardware impairments (HIs) such as quantization error, I/Q imbalance, non-linear power amplifier, and phase noise, introducing the transmitter and receiver distortion. The power of transmitter and receiver distortion is non-stationary due to their dependence on signal power and current channel gain. Due to HIs, training pilots and received signals get contaminated, and consequently, channel estimation performance degrades. Hence, we propose a novel sparse aware adaptive filtering approach based on ZALMS and sparse initiated ZALMS (SI-ZALMS) algorithm for narrowband mmWave hybrid MIMO system considering HIs. As adaptive method have inherent tracking capability (hence can track any variation in estimated channel and can reduce distortion noise) so it is well suited for channel estimation of mmWave hybrid MIMO system with non-ideal hardware and outperform existing algorithms e.g., orthogonal matching pursuit (OMP), sparse Bayesian learning (SBL), and Bayesian compressive sensing (BCS).

Further, in mmWave communications, large antenna arrays are typically used to generate highly directional beams that compensate for substantial path loss compared to the sub-6 GHz band. However, this high directivity makes mmWave com-

munication more susceptible to signal obstruction from foliage, men, car, and buildings. To overcome the blockage intelligent reflecting surface (IRS) is seen as a promising solution due to their ability to create favorable line-of-sight propagation environments and ultimately increase the coverage of mmWave communication systems in blocked and deep fading scenarios. However, accurate CSI is necessary for joint active and passive beamforming to maximize the benefits of IRS and mmWave MIMO. Therefore, we propose a variable step size zero attracting least mean square (VSS-ZALMS)-based online channel estimator for the cascaded channel in the IRS-aided mmWave hybrid MIMO system. Which provide higher estimation accuracy and SE at lower computational complexity compared to existing method like OMP and SBL.

Further, to improve the estimation accuracy and SE of IRS-aided mmWave hybrid MIMO system compared to VSS-ZALMS, OMP, and SBL, a recursive least square (RLS) based adaptive online channel estimator with a shorter sliding-window known as sparse exponential forgetting window least mean square (SEFWLMS) algorithm is proposed, which is obtained by adding l_0 norm penalty function in the cost function of EFWLMS. The proposed technique offers lower computational complexity and storage, resulting in higher estimation speed (i.e., lower latency) since no matrix inversion is involved in the cascade channel estimation.

Finally, through extensive simulations and analysis, the proposed algorithms demonstrate significant improvements in channel estimation accuracy, complexity, and latency compared to existing methods. These findings contribute to the advancement of mmWave communication systems and pave the way for future generations of wireless networks.

Contents

ABSTRACT	i
LIST OF FIGURES	vi
LIST OF TABLES	ix
LIST OF ABBREVIATIONS/ACRONYMS	x
List of Notations	xiv
1 Introduction	1
1.1 Overview	1
1.2 Millimeter Wave Spectrum	2
1.2.1 Distinctive mmWave Characteristics	4
1.2.2 Advantages of mmWave Communication	6
1.3 Millimeter Wave Propagation	7
1.3.1 Channel models	7
1.4 MIMO Architectures at mmWave	9
1.4.1 Analog Beamforming	10
1.4.2 Digital Beamforming	11
1.4.3 Hybrid Beamforming	12
1.5 Channel Estimation	13
1.5.1 Channel Estimation with 1-bit ADCs	14
1.5.2 Channel Estimation in the Analog Architecture	15
1.5.3 Channel Estimation Based on the Hybrid Architecture	16
1.6 Sparse Channel Estimation Algorithms	17
1.6.1 Convex Relaxation	18
1.6.2 Greedy Pursuits	19
1.6.3 Adaptive Algorithms	19
1.7 Intelligent Reflecting Surface	21
1.8 Hardware Imperfections	24
1.8.1 Non-Linear Power Amplifier	24
1.8.2 Transceiver Hardware Impairments	25
1.9 Motivation	26
1.10 Thesis Flowchart, Outline, and Contributions	28
2 ZALMS based Channel Estimator for mmWave Hybrid MIMO System	32
2.1 System Model	34

2.1.1	Sparse Formulation for mmWave Channel Estimation	36
2.2	Adaptive Filtering Framework for Channel Estimation	37
2.2.1	LMS Framework for mmWave Hybrid MIMO System	37
2.2.2	Proposed ZALMS Framework for mmWave Hybrid MIMO System	38
2.3	Parameter Analysis	40
2.3.1	Mean Behavior Analysis	41
2.3.2	Excess MSE Analysis	42
2.4	Simulation Results	44
2.5	Summary	46
3	SI-ZALMS based Channel Estimator for mmWave Hybrid MIMO System with HI	48
3.1	System Model	51
3.1.1	Hardware Impairments	51
3.1.2	MmWave Channel Model	54
3.1.3	Sparse Formulation of MmWave Hybrid MIMO Channel	55
3.1.4	Hybrid Processing Model with Hardware Impairments	56
3.2	Adaptive Filtering Approach	57
3.2.1	LMS Algorithms for Channel Estimation	57
3.2.2	Proposed ZALMS algorithms	58
3.3	Parameter Analysis	61
3.3.1	Bound of Step Size	61
3.3.2	Selection of Regularization Parameter	64
3.3.3	MSD Analysis	65
3.3.4	Complexity Analysis	66
3.3.5	Impact of RTHIs on the SE	66
3.4	Simulation Results	67
3.5	Summary	73
4	VSS-ZALMS based Channel Estimator for IRS-Aided mmWave Hybrid MIMO System	75
4.1	System and Channel Model	77
4.1.1	Channel Model for IRS aided mmWave System	79
4.1.2	Beamspace Representation of Channel	80
4.1.3	Problem Formulation	81
4.2	Adaptive Filtering Framework	82
4.2.1	VSS-LMS Framework	83
4.2.2	Proposed VSS-ZALMS Framework	84
4.3	Parameter Analysis For Performance Improvements	87
4.3.1	Convergence Analysis of VSS-ZALMS	87
4.3.2	Range of Regulariation Parameter ρ	88
4.3.3	SE Analysis	91
4.3.4	Computational Complexity	92
4.3.5	Training Overhead	92
4.3.6	IRS Deployment	93
4.4	Simulation and Analytical Results	94
4.5	Summary	98

5 SEFWLMS based Channel Estimator for IRS-Aided mmWave Hybrid MIMO System	100
5.1 System and Channel Model	102
5.1.1 IRS-Aided mmWave MIMO Channel Model	103
5.1.2 Sparse Representation of IRS-Aided mmWave Channel	104
5.2 Problem Formulation	105
5.3 SEFWLMS Framework	106
5.3.1 SEFWLMS Framework	107
5.3.2 Complexity Analysis	109
5.3.3 Spectral Efficiency	110
5.4 Simulation Results	110
5.5 Summary	113
6 Conclusion and Future Work	115
6.1 Conclusion	115
6.2 Future Work	116
REFERENCES	118
LIST OF PUBLICATIONS	136

List of Figures

1.1	Millimeter wave in spectrum band [http://surl.li/ttxgs].	3
1.2	Attenuation versus frequency in mmWave band [1].	5
1.3	The transceiver of the analog BF architecture.	10
1.4	The transceiver of Digital BF structure.	12
1.5	The transceiver of hybrid BF architecture.	13
1.6	Block diagram channel estimation using adaptive algorithms.	20
1.7	Reconfigurable metasurface with substantial number of passive scattering/reflecting elements.	22
1.8	Generalized transmission with hardware impairments.	25
1.9	Flowchart of the thesis.	29
2.1	Block diagram of mmWave hybrid MIMO transceiver.	34
2.2	MSE performance of LMS, ZALMS- l_1 , and ZALMS- l_0 with optimal and true channel. Simulation parameter are $N_T = 32$, $N_R = 32$, $\mu = .05$, $\rho_1 = 5 \times 10^{-5}$, $\rho_0 = 5 \times 10^{-6}$, $\nu = 20$	45
2.3	Comparison of spectral efficiency with estimated CSI from different estimator to the perfect CSI for the mmWave MIMO system, with $N_T = 32$, $N_R = 32$, $N_{RF} = 8$, $L = 2$, and pathloss component 3.	45
3.1	Generalized transmission with hardware impairments.	52
3.2	Millimeter wave hybrid MIMO transceiver block diagram with non-ideal hardware.	53
3.3	Graphical representation of received signal \mathbf{y}	57
3.4	NMSE versus number of iterations performance of LMS, block LMS, and ZALMS with two impairments level $\kappa_t = \kappa_r = 0.05^2$ and $\kappa_t = \kappa_r = 0.15^2$ with $N_{RF} = 8$, $N_T = N_R = 32$, $L = 2$, $\rho_0 = 5 \times 10^{-5}$, $\rho_1 = 1 \times 10^{-6}$, $\mu = 0.03$, and SNR = 20 dB.	68
3.5	NMSE versus SNR performance of OMP, BCS, SBL, ZALMS- l_1 , and ZALMS- l_0 with impairment level $\kappa_t = \kappa_r = 0.1^2$, $N_{RF} = 8$, $N_T = N_R = 32$, $L = 2$, $\rho_0 = 5 \times 10^{-5}$, $\rho_1 = 1 \times 10^{-6}$, $\mu = 0.03$	68
3.6	NMSEE versus number of iterations performance of zero-initiated and sparse-initiated ZALMS- l_0 , ZALMS- l_1 , with $\kappa_t = \kappa_r = 0.05^2$, $N_{RF} = 8$, $N_T = N_R = 32$, $L = 2$, $\rho_0 = 5 \times 10^{-5}$, $\rho_1 = 1 \times 10^{-6}$, $\mu = 0.03$, and SNR = 20 dB.	69
3.7	MSE versus iterations performance of ZALMS- l_0 for different values of ρ at impairments level $\kappa_t = \kappa_r = 0.05^2$, $L = 2$, $N_T = N_R = 32$, $N_{RF} = 8$, $\mu = .03$, and SNR = 20 dB.	69
3.8	Simulation and analytical performance plot of NMSEE versus iterations of ZALMS- l_0 , at different impairments level.	70

3.9	MSE versus iterations performance of LMS, ZALMS- l_1 , and ZALMS- l_0 for different μ	71
3.10	MSE versus ρ performance of ZALMS- l_0 for different μ	71
3.11	MSEE vs μ simulation and analytical plots of ZALMS- l_0 for various ρ . The analytical MSEE for ZALMS- l_0 have been evaluated using (3.60).	72
3.12	SE versus the SNR performance plot of ZALMS- l_0 for different values of κ_t and κ_r with $N_T = 32$, $N_R = 32$ and $N_{RF} = 8$	72
4.1	Diagram of the IRS-assisted communication system.	76
4.2	Diagram illustrating the channel estimation for an IRS-assisted mmWave hybrid MIMO transceiver.	78
4.3	IRS installation in point-to-point communication system.	93
4.4	NMSE versus number of iterations performance for VSS-LMS, VSS-ZALMS- l_1 , and VSS-ZALMS- l_0 , estimators for the considered system.	94
4.5	NMSE versus SNR performance of the proposed and existing estimators.	95
4.6	SE versus SNR performance of SBL, OMP, VSS-ZALMS, and oracle LS.	96
4.7	Capacity versus number of reflecting elements M performance of SBL, VSS-ZALMS- l_1 , and VSS-ZALMS- l_0 , OMP, and oracle LS estimators.	97
4.8	Receive SNR versus IRS-User (UE) horizontal distance d for different reflecting elements M	97
5.1	Diagram illustrating the channel estimation for an IRS-assisted mmWave hybrid MIMO transceiver.	102
5.2	NMSE versus number of iterations performance the SEFWLMS, OMP, SBL, and oracle LS estimators.	111
5.3	NMSE versus SNR performance the SEFWLMS, OMP, SBL, and oracle LS estimators.	112
5.4	SE versus SNR performance the SEFWLMS, OMP, SBL, and oracle LS estimators.	113

List of Tables

3.1	Complexity comparison of different algorithms	66
4.1	Parameters for Simulation	93
5.1	Simulation parameters	111

List of Abbreviations/Acronyms

3GPP 3rd Generation Partnership Project.

4G Fourth Generation.

5G Fifth Generation.

ADC Analogue-to-Digital Converter.

AoA Angle of Arrival.

AoD Angle of Departure.

AWGN Additive White Gaussian Noise.

B5G Beyond 5G.

BER Bit Error Rate.

BPSK Binary Phase-Shift Keying.

BS Base Station.

CS Compressive Sensing.

CSI Channel State Information.

DAC Digital-to-Analog Converter.

DFT Discrete Fourier Transform.

EE Energy Efficiency.

EFWLMS Exponential Forgetting Window Least Mean Square.

EM Electromagnetic.

EVM Error Vector Magnitude.

FDD Frequency-Division Duplexing.

HI Hardware Impairment.

i.i.d. Independent and Identically Distributed.

- I/Q** In-Phase/Quadrature.
- IEEE** Institute of Electrical and Electronics Engineers.
- IRS** Intelligent Reflecting Surface.
- LMS** Least Mean Square.
- LoS** Line-of-Sight.
- LS** Least Squares.
- LTE** Long Term Evolution.
- MIMO** Multiple-Input Multiple-Output.
- MMSE** Minimum Mean-Squared Error.
- mmWave** Millimeter Wave.
- MSE** Mean-Squared Error.
- NLD** Non-Linear Distortion.
- NLoS** Non-Line-of-Sight.
- NLPA** Non-Linear Power Amplifier.
- NMSE** Normalized MSE.
- OFDM** orthogonal frequency division multiplexing.
- OMP** Orthogonal Matching Pursuit.
- PA** Power Amplifier.
- PAPR** Peak-to-Average-Power Ratio.
- PDF** probability density function.
- RF** radio frequency.
- RTHI** Residual Transceiver Hardware Impairment.
- RV** Random Variable.
- SBL** Sparse Bayesian Learning.
- SE** Spectral Efficiency.
- SI** Sparse Initiated.
- SISO** Single-Input Single-Output.
- SNR** Signal-to-Noise Ratio.

SVD Singular Value Decomposition.

TDD Time-Division Duplexing.

UE User Equipment.

ULA Uniform Linear Array.

UPA Uniform Planer Array.

VSS Variable Step Size.

ZA Zero Attractor.

ZF Zero-Forcing.

List of Notations

$ \cdot $: Absolute value.
$\ \cdot\ _0$: l_0 -norm, evaluated as the number of nonzero elements.
$\ \cdot\ _1$: l_1 -norm, evaluated as sum of absolute value of all elements.
$\ \cdot\ _2$: l_2 -norm.
$\ \cdot\ _F$: Frobenius norm.
\otimes	: Kronecker product.
\odot	: Khatri-Rao product.
\circ	: Hadamard product.
x	: Scalar.
\mathbf{x}	: Vector.
\mathbf{X}	: Matrix.
$\mathbf{X}(i, j)$: The element in the row i and the column j of matrix \mathbf{X} .
\mathbf{X}^T	: Transpose of \mathbf{X} .
\mathbf{X}^H	: Conjugate transpose of \mathbf{X} .
\mathbf{X}^*	: Complex conjugate of \mathbf{X} .
\mathbf{X}^\dagger	: Pseudo inverse of \mathbf{X} .
$[\mathbf{X} \mathbf{Y}]$: Horizontal concatenation.
\mathbb{C}	: Set of complex numbers.
$\text{tr}(\cdot)$: Trace of matrix.
μ	: Step size parameter.
ρ	: Regularization parameter.
ν	: Accuracy parameter.
$\Re(\cdot)$: Real part of the complex argument.
$\Im(\cdot)$: Imaginary part of the complex argument.
$\mathbf{0}_n$: $n \times 1$ sized all-zero vector.
$\mathbf{1}_n$: $n \times 1$ sized all-ones vector.
\mathbf{I}_n	: $n \times n$ sized identity matrix.
$\mathbb{E}[\cdot]$: Statistical expectation operator
$\mathcal{P}(\cdot)$: Statistical probability operator
$f_X(\cdot)$: Probability density function (PDF) of a RV X
$F_X(\cdot)$: Cumulative distribution function (CDF) of a RV X
$\mathcal{CN}(\mu, \sigma^2)$: Complex normal distribution with mean μ and variance σ^2 .
Δf	: First order derivative (gradient) of function f .
$\Delta^2 f$: Second order derivative (Hessian) of function f .
$\frac{\delta f}{\delta x}$: First order partial derivative of a multi-variate function f with respect to variable x .

Chapter 1

Introduction

1.1 Overview

In wireless communication, ultra-high data rates and energy efficiency, ultra-reliable and low-latency communication (URLLC), enhanced mobile broadband (eMBB), global coverage and connectivity, and massive machine-type communication (mMTC) are stringent requirements for beyond 5G/6G networks [2]. At the physical layer, the speed of the cellular links has increased manyfold from 50 kbps in 2G systems, 144 kbps in 2.5G systems, approximately 2 Mbps in 3G systems to around 100 Mbps in 4G systems (3GPP-LTE and WiMAX), around 1 Gbps in 5G and around 1 Tbps in 6G systems [3]. Similarly, the speed of indoor wireless local area networks (LANs) has increased from 11 Mbps in IEEE 802.11b to 300 Mbps in IEEE 802.11n within the last 20 years [4]. The above demand can not be fulfilled despite efficient use of the existing spectrum, the available bandwidth does not commensurate with the increase in demand. To this end, there has been increased interest in standardizing the spectrum above 6 GHz for mobile communications. As the Data traffic capacity (bits/s/Km²) = Cell density(cells/Km²) × Spectral efficiency (bits/s/Hz/cell) × Available spectrum (in Hz). Hence, to address the 5G/6G design targets, the information theory suggests that there are predominantly three key approaches to achieve several orders of magnitude increase in system capacity.

1. **Ultra-dense networks (UDNs):** The network densification already has been adopted in existing 4G wireless cellular networks, which is essentially known as small cell technology, and a denser network can further boost the

network capacity [5].

2. **Large quantities of new bandwidth:** Migrating toward higher frequencies will release a large amount of bandwidth available to achieve higher capacity. In particular, the millimeter-wave (“mmWave,” for carrier frequencies of 30–300 GHz) communications can be a promising candidate [6].
3. **High spectrum efficiency:** By using a large number of antennas, multiple-input multiple-output (MIMO) or intelligent reflecting surface (IRS) can significantly improve the spectrum efficiency by extensively harnessing the available space resources [7].

Hence, current and future research is directed toward next-generation wireless communication technologies such as millimeter wave (mmWave) spectrum, multiple-input multiple-output (MIMO) system and intelligent reflecting surfaces (IRSs), which are discussed as follows.

1.2 Millimeter Wave Spectrum

Millimeter wave represents a wireless technology facilitating high-speed data transmission, reaching multi-gigabit per second rates in communication systems. It operates within wavelengths ranging from 1 to 10 mm, corresponding to frequencies spanning 30 to 300 GHz that is shown in Figure 1.1. These frequency bands have been firmly established over time and are effectively utilized for various communication needs. Bose showcased the initial mmWave communication over a century ago. Today, mmWave bands find extensive application in satellite communication, fronthaul networks, and point-to-point communication systems.

Coverage of up to approximately 200 meters is achievable with 1 watt of transmit power using mmWave links. To attain high data rates while ensuring efficient power usage and long-distance transmission, mmWave communications rely on line-of-sight (LoS) transmission.

The IEEE 802.11ad standard, developed in 2014 for outdoor backhaul, outlines the physical and MAC layers for frequencies above 40 GHz, supporting wireless transmission at multi Gbps rates but with limited range [8].

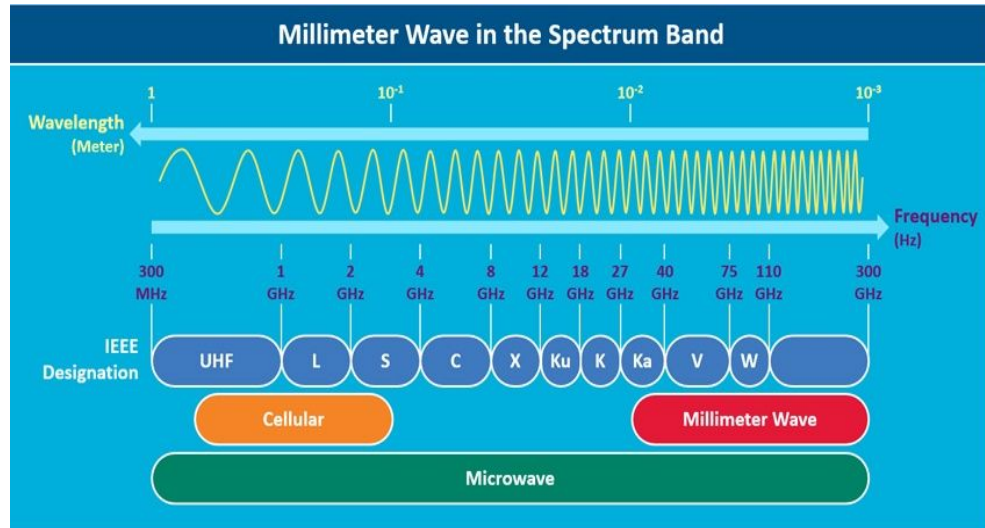


Figure 1.1: Millimeter wave in spectrum band [<http://surl.li/ttxgs>].

Recent studies demonstrate that point-to-point systems utilizing mmWave, either in V-band (57-64 GHz) or E-band (71-76 GHz and 81-86 GHz), can achieve high data rates (up to 10 Gbit/s) while mitigating interference over long distances. Most countries and regions worldwide regulate or are considering regulation for the deployment of communication systems within the V-band and E-band spectra [9].

The proposal of mmWave in V-band (57-64 GHz) in 2009 allowed for very high data rates exceeding 2 Gbit/s. Advantages of this band include interference mitigation, security, and quality of service (QoS) as it operates in an unlicensed spectrum. However, V-band encounters challenges such as high atmospheric attenuation (approximately 15 dB/km) and limitations on transmitted power (< 0.5 W) [10].

E-band mmWave (71-76 GHz and 81-86 GHz bands) is favorable for high-rate and long-range wireless communication due to minimal atmospheric attenuation (0.5 dB/km) [11]. Additionally, E-band technology offers advantages over other wireless communication methods, including low construction costs, rapid development, flexibility, high reliability, and security. Moreover, E-band systems can operate with up to 3 watts of output power, utilizing highly focused signals and high-gain antennas. However, E-band operation requires a licensed spectrum and entails a high antenna gain.

1.2.1 Distinctive mmWave Characteristics

The unique properties of high-frequency transmission suggest that the technologies commonly utilized at lower frequencies cannot be directly transferred to mmWave communications. The essential attributes crucial for modeling mmWave systems and comprehending signal propagation at these frequencies are outlined below.

- **Isotropic Path Loss:** In all wireless communication systems, the transmitted signal experiences attenuation based on distance. According to Friis Law, the isotropic path loss increases proportionally to the inverse of the squared wavelength, represented as $\frac{P_{TX}}{P_{RX}} \propto \lambda^{-2}$ [12]. This suggests that mmWave propagation will encounter greater path loss compared to conventional systems operating at lower frequencies. However, directional transmissions can offset this increased path loss through the use of directional antenna gains [13]. Hence, employing large arrays becomes necessary to achieve these gains. Fortunately, implementing large antenna arrays at both the transmitter and receiver of mmWave systems is feasible due to the smaller wavelengths associated with these higher frequencies. Consequently, Multiple Input Multiple Output (MIMO) antenna arrays play a crucial role in ensuring high-quality mmWave communications.
- **Signal absorption and blockages:** In contrast to conventional wireless systems, mmWave signals are more prone to obstruction since most objects in the propagation environment, such as walls, lampposts, birds, and people, are larger than the signal wavelength. Nonetheless, reflection and scattering mechanisms enable transmission between a transmitter and a receiver when steerable antennas are utilized to locate objects that reflect or scatter energy [14]. Hence, antenna arrays capable of directional and adaptive beamforming are indispensable for ensuring successful communication in mmWave systems [15]. Additionally, mmWave signals are influenced by atmospheric conditions like temperature and humidity, which affect the molecular components of air and water, leading to atmospheric absorption of signals with small wavelengths. Figure 1.2 illustrates the attenuation alongside free space loss across the mmWave spectrum. It is evident that severe attenuation occurs at

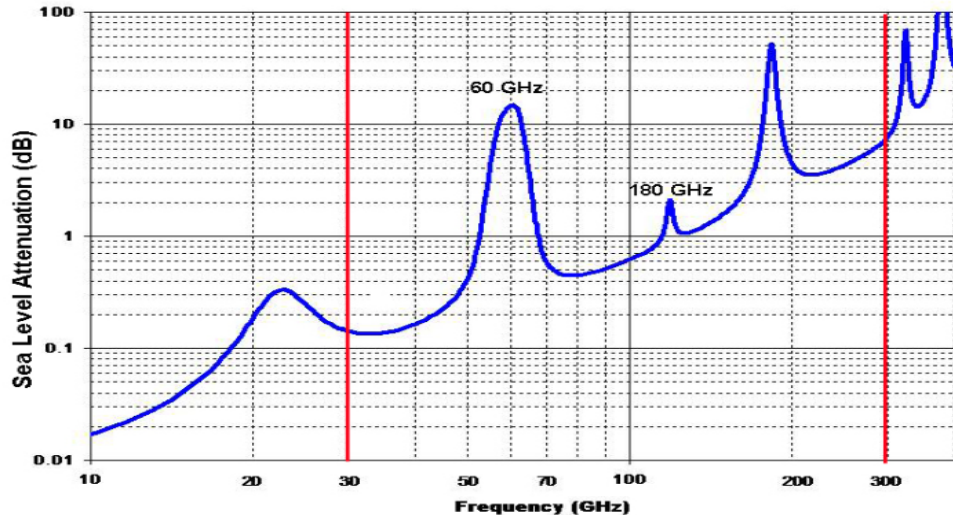


Figure 1.2: Attenuation versus frequency in mmWave band [1].

certain spectrum bands, such as 60 and 180 GHz. Consequently, these frequencies are suitable for short-range wireless technologies. Conversely, there is minimal attenuation (below 1 dB/km) in the 30-50, 70-90, 120-160, and 200-300 GHz bands, making them well-suited for longer distances and viable candidates for future mobile and cellular communications. Furthermore, adaptive antenna arrays can be employed to compensate for specific atmospheric losses as they can be adjusted to accommodate particular levels of interference in the low-attenuation bands [14].

- **Sparse channels:** In contrast to standard wireless systems, mmWave channels typically exhibit sparse characteristics regarding the number of significant scatterers contributing to the multi-path components of a transmitted signal [16]. This assertion is supported by measurements conducted on the 28 and 73 GHz channels as detailed in [17]. The findings reveal that, on average, mmWave channels feature two clusters contributing to propagation paths, with the angles of arrivals closely aligned with the boresight direction. The sparsity observed in mmWave channels underscores the necessity for alternative channel models distinct from existing standard wireless channel models.

1.2.2 Advantages of mmWave Communication

The benefits of mmWave technology can be measured by the solutions it provides for upcoming 5G cellular networks. In comparison to current 4G-LTE networks, mmWave presents several notable advantages, including [18].

- **Bandwidth allocations:** Clearly, the utilization of mmWave carrier frequencies, typically in the gigahertz range, enables the allocation of larger channel bandwidths. This directly leads to higher data rates and indirectly contributes to reduced latencies, as insufficient bandwidth can exacerbate network latency. Consequently, service providers will be capable of accommodating data-intensive applications for users with minimal latency.
- **Capacity gain:** Furthermore, apart from widening the channel bandwidth, mmWave technology can be employed to diminish coverage areas, facilitating the establishment of densely interconnected communication links and leveraging spatial reuse to achieve enhanced capacity gains. Additionally, the performance benefits derived from employing MIMO over SISO configurations in conventional wireless systems are also applicable to mmWave communications, given that mmWave frequencies can utilize massive MIMO techniques. These advantages encompass the following.
 1. **Interference suppression:** In multi-user systems, employing multiple antennas at both the transmitter and receiver enhances the capability to mitigate intra-channel interference. This is accomplished through precoding at the transmitter, combining at the receiver, or a combination of both methods. However, the precoding technique utilized in mmWave systems differs from that used in standard transmissions.
 2. **Diversity gain:** Spatial diversity in mmWave systems can be harnessed by employing multiple antennas at both ends, aiming to reduce the effects of channel variations and signal losses.
 3. **Multiplexing gain:** By utilizing multiple antennas at the transmitter, it becomes possible to transmit parallel streams to the user without requiring additional bandwidth or power. This effectively augments the

number of spatial dimensions available for communication.

1.3 Millimeter Wave Propagation

The fundamental structure of mmWave communications typically involves a point-to-point link, where a single transmitter equipped with a sizable array of antennas communicates with a multi-antenna receiver. The signal transmitted is influenced by its surrounding environment, encountering multiple paths due to scatterers and reflectors, which results in various distorted versions of the transmitted signal reaching the receiver. These propagation effects are commonly referred to as small-scale fading. Alongside small-scale channel effects, each version of the signal experiences distance-dependent attenuation and shadowing loss from obstacles, known as large-scale fading. These propagation phenomena, combined with potential blockages, constitute the essential elements of mmWave communications.

Fortunately, mmWave communication integrates MIMO antenna arrays, allowing for the exploitation of these large arrays to achieve directional transmissions through directional beamforming. This approach not only compensates for distance-related path loss but also effectively manages interference using advanced beam shaping techniques [19].

1.3.1 Channel models

Narrowband channel model

In the case of mmWave propagation, the channel presents a number of characteristics that differentiate it from the standard MIMO channel. Hence, the statistical fading distributions employed in latter cannot be directly applied for mmWave communications. With these characteristics, the Saleh-Valenzuela model extended to mmWave channels [20] enables us to describe the structure of a mmWave channel mathematically by means of a narrowband clustered channel model. From a physical point of view, it represents a geometric model with N_p scatterers, where each scatterer is assumed to contribute a signal propagation path given as

$$\mathbf{H} = \sqrt{\frac{N_T N_R}{N_p}} \sum_{l=1}^{N_p} \alpha_l \mathbf{a}_R(\phi_R^l, \theta_R^l) \mathbf{a}_T^H(\phi_T^l, \theta_T^l), \quad (1.1)$$

where α_l is the path gain of the l^{th} path. The transmit and receive steering vectors (SVs) of the l^{th} path in \mathbf{H} are given by $\mathbf{a}_R(\phi_R^l, \theta_R^l)$ and $\mathbf{a}_T(\phi_T^l, \theta_T^l)$, respectively, and $\phi_R^l(\theta_R^l)$ and $\phi_T^l(\theta_T^l)$ as the azimuth (elevation) angle of arrival (AoA) and angle of departure (AoD), respectively, for the l^{th} path in the channel \mathbf{H} . Here, we consider that uniform planar array (UPA) is applied at the transmitter, and IRS. For a uniform planar array in the yz -plane with W and H elements on the y and z axes respectively, the array response vector is given by [21]

$$\mathbf{a}^{UPA}(\phi, \theta) = \frac{1}{\sqrt{N}} \left([1, \dots, e^{jkd(m \sin(\phi) \sin(\theta) + n \cos(\theta))}, \dots, \dots, e^{jkd((W-1) \sin(\phi) \sin(\theta) + (H-1) \cos(\theta))}] \right)^T, \quad (1.2)$$

where $0 < m < W - 1$ and $0 < n < H - 1$ are the y and z index of an antenna element respectively and $N = WH$, d is antenna spacing, and $k = \frac{2\pi}{\lambda}$.

Furthermore, the combination of the high dimensionality and the highly directional nature of mmWave propagation means that the narrowband channel can alternatively be represented by its beamspace [13]. In other words, the array steering vectors can be used to define the communication space of the channel. Accordingly, equation (1.1) can be rewritten as

$$\mathbf{H} = \mathbf{A}_R \mathbf{H}_\alpha \mathbf{A}_T^H, \quad (1.3)$$

where $\mathbf{A}_R \in \mathbb{C}^{N_R \times N_p}$, and $\mathbf{A}_T \in \mathbb{C}^{N_T \times N_p}$ are the array response vectors of the receiver and transmitter, respectively, and $\mathbf{H}_\alpha = \text{diag}(\boldsymbol{\alpha})$ contains the complex gains of all paths with $\boldsymbol{\alpha} = [\alpha_1, \alpha_2, \dots, \alpha_{N_p}]$. The channel in equation (1.3) is commonly referred to as the virtual channel representation [22] and is useful for channel estimation. Since the beamspace and antenna space are related by a spatial Fourier transform, the virtual channel can also be expressed as [23]

$$\mathbf{H} = \mathbf{U}_R \mathbf{H}_\alpha \mathbf{U}_T^H, \quad (1.4)$$

where $\mathbf{U}_R \in \mathbb{C}^{N_R \times N_R}$, and $\mathbf{U}_T \in \mathbb{C}^{N_T \times N_T}$ are the unitary discrete Fourier transform

(DFT) matrices. The beamspace of an N -dimensional uniform linear array (ULA) is represented by spatial angles, $\phi_i, i = 0, \dots, N - 1$ with uniform spacing and the corresponding array response vectors results in an orthonormal basis for the signal space. Specifically, the unitary DFT matrix is expressed as [22]

$$\mathbf{U} = \frac{1}{\sqrt{N}} [\mathbf{a}(\phi_0), \dots, \mathbf{a}(\phi_{N-1})]. \quad (1.5)$$

Wideband channel model

For wideband operations in non-line-of-sight environments, the impact of the multi-path delay spread is more significant. Hence, each path is characterised by a time delay in addition to the complex gain and angles of departure and arrival [24]. Accordingly, the wideband channel model is used to incorporate the multi-path delays and is given as [25]

$$\mathbf{H}_w = \sqrt{\frac{N_T N_R}{N_p}} \sum_{l=1}^L \alpha_l p_{rc}(\delta T_s - \tau_l) \mathbf{a}_R(\phi_R^l, \theta_R^l) \mathbf{a}_T^H(\phi_T^l, \theta_T^l), \quad (1.6)$$

where \mathbf{H}_w denotes the channel response at delay δ , $p_{rc}(\tau)$ is the raised cosine pulse shaping filter generating pulses of the signal at T_s intervals evaluated at τ seconds, and τ_l is the time delay of the l -th path. Note that the channel characteristics are assumed to be constant within the coherence time of $t = \delta T_s$ seconds.

1.4 MIMO Architectures at mmWave

The MIMO architecture commonly used in conventional wireless communications, where all signal processing occurs at the baseband level, is depicted in Figure 1.4. An important characteristic of existing commercial MIMO standards is that the technology typically supports a limited number of antennas, typically ranging from (2 to 8) [13]. This limitation arises because baseband processing necessitates a separate RF chain comprising data converters and signal mixers for each antenna. However, in mmWave systems, which allow for tightly packed antenna arrays typically consisting of (32 to 256) array elements [26], the substantial costs associated with complexity and power consumption render baseband processing impractical for

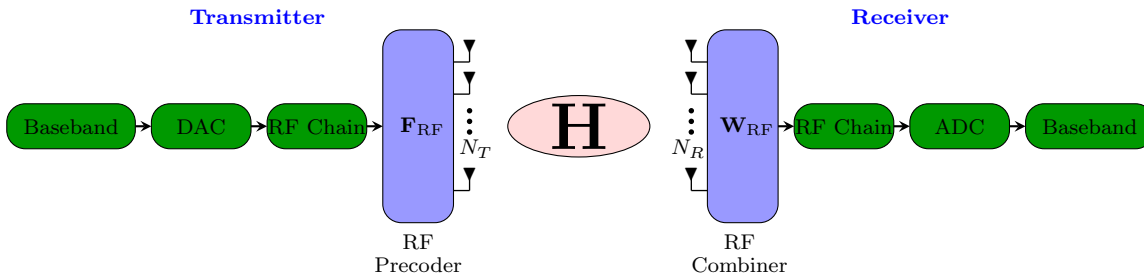


Figure 1.3: The transceiver of the analog BF architecture.

communications at mmWave frequencies. Considering these hardware constraints, several alternative architectures have been proposed for use in mmWave systems given as follows.

1.4.1 Analog Beamforming

Analog beamforming (BF) operates by employing analog phase shifters in the RF domain [24]. In a mmWave system utilizing analog BF, depicted in Figure 1.3, multiple antennas are amalgamated using phase shifters and linked to a single RF chain. Analog BF transmits a phase-shifted version of the same signal across the antenna elements, generating a beam directed toward a specific angular direction. Consequently, analog BF cannot multiplex multiple users. Additionally, the BF gains with analog BF are diminished compared to digital BF due to the utilization of quantized phase shifts and constant amplitude. However, analog BF proves to be the most cost-effective BF method for single-user communications, requiring only one RF chain and one analog-to-digital converters (ADCs)/digital-to-analog converters (DACs) pair. Despite some performance limitations compared to digital BF, the reduced cost of analog BF makes it a promising architecture for constructing large antenna array systems in mmWaves. Furthermore, analog BF suffices for Line-of-Sight (LOS) single-user mmWave communications, positioning it as a preferable alternative to digital BF in the literature [25].

In [25], a general BF criterion, dependent on a single parameter, has been proposed for analog BF under orthogonal frequency division multiplexing (OFDM) transmissions. Moreover, [16] presents a binary search beam training algorithm based on a multi-resolution BF codebook to discover and refine the optimal beams for wireless personal area networks. An analog BF algorithm for mmWave sys-

tems, directly enhancing baseband equalization performance, is proposed in [27]. However, analog BF becomes inefficient for mmWave channels characterized by multipath propagation and frequency-selective fading [28]. Additionally, the RF constraints stemming from quantized phase shifters and constant modulus of phase shifters restrict the performance of analog BF. Despite these limitations, analog BF has garnered significant interest in the industry due to its reduced cost compared to digital BF. Wireless communication standards, including IEEE 802.15.3c, IEEE 802.11ad, and Wireless HD, utilize analog BF for single-stream transmission [29].

1.4.2 Digital Beamforming

Digital beamforming (BF) is entirely implemented in the baseband domain by connecting a baseband precoder with multiple antenna elements through ADC/DAC and RF chains, as depicted in Figure 1.4. In the digital BF architecture, each antenna element is fed by a separate ADC/DAC and RF chain. Digital control over the phase and amplitude of the signal sent from each antenna provides high flexibility, allowing for the attainment of maximum BF gain. Additionally, digital BF supports multi-user communication, enabling the transmission of the superposition of any number of beams to each mobile user. With the flexibility of digital BF, beams can be adapted to multipath propagation and frequency-selective fading. By transmitting different beams in each subcarrier, the effects of multipath propagation and frequency-selective fading can be compensated for.

For conventional MIMO systems operating below 6 GHz, implementing BF in the baseband domain is preferred, given the acceptable hardware cost. However, in the context of massive MIMO systems, the hardware implementation of digital BF poses a significant challenge due to the requirement of a large number of ADCs/DACs and RF chains [30]. Placing a large number of antenna elements and ADCs/DACs in a confined area is challenging, and each ADC/DAC pair consumes a considerable amount of power, further complicating digital BF implementation. Nonetheless, research has also explored the hardware design of mmWave systems with a fully digital architecture [31].

In [31], it has been demonstrated that digital BF architectures employing low-resolution ADCs can achieve power efficiency with negligible loss in the overall ca-

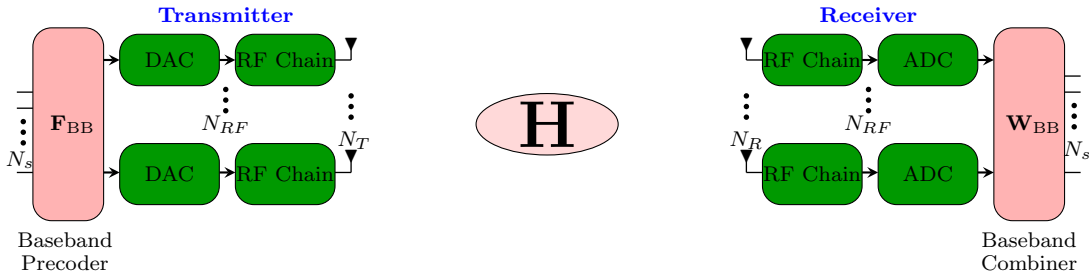


Figure 1.4: The transceiver of Digital BF structure.

capacity of the cellular system. To further mitigate power consumption in digital BF architectures, 1-bit or fewer bit ADCs/DACs can be utilized [32]. In such a digital BF setup, a pair of ADCs/DACs with a limited number of bits are employed to process the in-phase and quadrature components of the demodulated signal received from the RF chain. Consequently, power consumption can be significantly reduced compared to conventional digital BF architectures utilizing the same number of RF chains.

1.4.3 Hybrid Beamforming

Hybrid BF strikes a balance between system performance and hardware complexity. Hybrid BF at the transmitter and the receiver are called hybrid precoding and hybrid combining, respectively, which is shown in Figure 1.5. Both the hybrid precoding and combining operations are divided into analog and digital domains. In hybrid BF, a set of analog phase shifters, each connected to antenna elements, are fed by a separate RF chain from the baseband precoder. The number of RF chains in hybrid BF is lower-bounded by the number of transmitted data streams [33]. By maximizing hardware reuse, hybrid BF reduces the power consumption significantly compared to digital BF. Moreover, the number of antenna elements in hybrid BF can be set as high as in digital BF [34]. Since BF gain depends on the number of antenna elements, BF gain of digital BF can be achieved with hybrid BF by using a few numbers of RF chains and ADC/DAC pairs. Therefore, the cost and power consumption can be significantly reduced with hybrid BF compared to digital BF, which allows deployment of mmWave massive MIMO systems in places with a small area such as building corners, lamp posts, etc [35]. Various use cases of hybrid BF have shown its applicability to many challenging scenarios such as autonomous

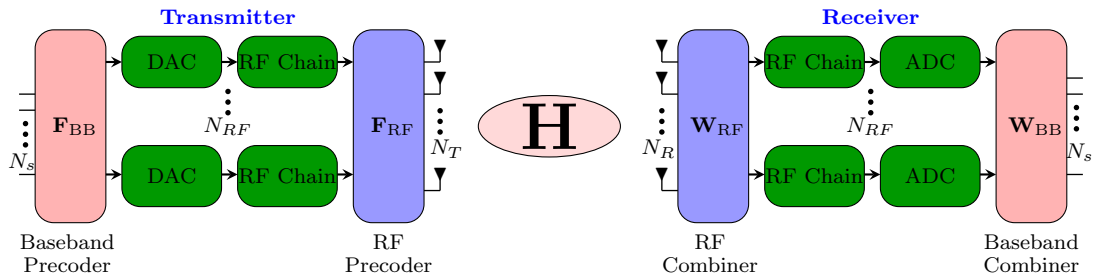


Figure 1.5: The transceiver of hybrid BF architecture.

vehicles, IoT, ultra-low-latency communication in 5G, etc [36].

With hybrid BF, device-to-device (D2D) with low latency and without inter-device interference can be enabled using the same time and frequency resources. Moreover, hybrid BF in mmWave massive MIMO can be used for back-hauling and small cell systems [37].

1.5 Channel Estimation

Channel estimation holds significance in the practical deployment of any wireless communication system since the assumption of perfect channel knowledge is often unrealistic. Typically, available CSI is derived from channel estimates. In mmWave systems, channel estimation is especially crucial for designing analog and digital beamformers. The strategies employed for channel estimation in mmWave systems differ from traditional methods used to estimate channels in standard wireless systems in several aspects [38].

- The mmWave channel matrices are significantly large owing to the extensive antenna arrays inherent in their propagation characteristics. Employing traditional techniques would necessitate training an immense number of channel coefficients, leading to a problematic level of training overhead.
- Accessing the entries of a mmWave channel directly is not feasible, as the measurements of the channel in the baseband are intertwined with the RF precoders and combiners.
- Applying traditional estimation techniques directly would require long training sequences due to the wide channel bandwidths available in mmWave systems.

This leads to elevated noise power, resulting in a low signal-to-noise ratio (SNR) before constructing the beamformers.

In view of this, we present a brief overview of channel estimation strategies suitable for mmWave communication.

1.5.1 Channel Estimation with 1-bit ADCs

Channel estimation techniques for mmWave systems using low-resolution receivers also depend on the sparsity of the channel and make use of the narrowband virtual channel model. Consequently, the sparse recovery problem can be defined. The quantized processed signal is expressed as

$$\mathbf{y} = \text{sgn}(\mathbf{H}\mathbf{s} + \mathbf{n}). \quad (1.7)$$

If the transmitter uses G_T beamforming vectors to transmit the training symbols, the received signal obtained by concatenating G_R received vectors is given by [25]

$$\mathbf{Y} = \text{sgn}(\mathbf{H}\mathbf{X} + \mathbf{N}), \quad (1.8)$$

where $\mathbf{X} \in \mathbb{C}^{N_T \times K}$ is the training sequence with K representing the length of the sequence, and \mathbf{N} is the noise matrix. Using the virtual channel model from (1.4) and setting $\mathbf{X} = \mathbf{U}_T \mathbf{Z}$, we have

$$\mathbf{Y} = \text{sgn}(\mathbf{U}_R \mathbf{H}_\alpha \mathbf{U}_T^H \mathbf{U}_T \mathbf{Z} + \mathbf{N}), \quad (1.9)$$

$$= \text{sgn}(\mathbf{U}_R \mathbf{H}_\alpha \mathbf{Z} + \mathbf{N}). \quad (1.10)$$

Exploiting the sparse nature of the mmWave channel through vectorization, we obtain

$$\begin{aligned} \text{vec}(\mathbf{Y}) &= \text{sgn}(\text{vec}(\mathbf{U}_R \mathbf{H}_\alpha \mathbf{Z} + \mathbf{N})), \\ \mathbf{y}_v &= \text{sgn}((\mathbf{Z}^T \otimes \mathbf{U}_R) \mathbf{h}_\alpha + \text{vec}(\mathbf{N})), \end{aligned} \quad (1.11)$$

where equation (1.11) follows from the identity $\text{vec}(\mathbf{ABC}) = (\mathbf{C}^T \otimes \mathbf{A})\text{vec}(\mathbf{B})$, and $\mathbf{h}_\alpha = \text{vec}(\mathbf{H}_\alpha)$. The formulation of \mathbf{y}_v in equation (1.11) represents the sparse recov-

ery formulation for channel estimation using 1-bit ADCs and it involves estimating \mathbf{h}_α given \mathbf{Z} . Accordingly, the compressive sensing framework can be applied to recover the sparse vectors. Assuming prior information about the distribution of \mathbf{h}_α is available, the generalised approximate message passing (GAMP) algorithm can be employed to estimate the channel in quick steps [25]. Other algorithms which do not require prior information of \mathbf{h}_α , such as expectation maximisation (EM) can be used to detect the non-zero elements of \mathbf{h}_α [39].

1.5.2 Channel Estimation in the Analog Architecture

Beam training is the primary approach for configuring analog beamformers in mmWave systems, allowing for adaptive adjustment without requiring precise channel state information. It utilizes a codebook containing various beam patterns at different resolutions and relies on iterative information exchange between the transmitter and receiver. This iterative process gradually narrows down the beamwidth until the optimal angular directions are determined, representing the combination of departure and arrival angles that maximize signal strength between the transmitter and receiver. Several codebook beam-training protocols have been developed [40–42]. In [41], the codebooks categorize beam patterns based on their resolution, ranging from quasi-omni antenna patterns covering broad regions to high-resolution beam patterns. The beamforming training protocol aims to configure the beamformers efficiently and is divided into three stages: D2D linking, sector-level searching, and beam-level searching. In [40], a beamforming technique employs a distance-based hierarchical codebook to adaptively sample the channel subspace and search for the beam pair maximizing the received SNR. These codebook beam-training strategies are desirable as they obviate the need for explicit channel estimation and have been adopted in recent standards for mmWave systems such as IEEE 802.11ad and IEEE 802.15.3c. However, the information provided by beam training may not be sufficient for complex processing applications like interference cancellation and multi-user MIMO, leading these standards to assume single-stream transmission [13, 43]. Additionally, the training time involved in beam-training can be prohibitive [42], and these strategies may not robustly identify non-line-of-sight (NLOS) paths [44].

1.5.3 Channel Estimation Based on the Hybrid Architecture

In the hybrid architecture, which integrates analog and digital beamforming, channel estimates are acquired using compressed sensing (CS) techniques to leverage the inherent sparsity of mmWave channels. Since the mmWave channel can be characterized by a small set of parameters, such as the angle of arrival (AoA)/angle of departure (AoD) and the complex gain of each path, channel estimation involves estimating these key parameters [38].

The fundamental concept of CS is to reconstruct a compressible (sparse) signal from a limited number of measurements. Specifically, for the hybrid architecture, the hybrid precoders and combiners serve as the measurement matrices. Referring to Figure 1.5, suppose the transmitter employs G_T beamforming vectors to transmit training symbols \mathbf{s} , and the receiver utilizes G_R measurement vectors to detect the transmitted signal. Then, the received signal of size $G_R \times G_T$ can be expressed as

$$\mathbf{y} = \mathbf{W}_{\text{BB}}^H \mathbf{W}_{\text{RF}}^H \mathbf{H} \mathbf{F}_{\text{RF}} \mathbf{F}_{\text{BB}} \mathbf{s} + \mathbf{W}_{\text{BB}}^H \mathbf{W}_{\text{RF}}^H \mathbf{n}. \quad (1.12)$$

Which can be rewritten as

$$\mathbf{Y} = \mathbf{W}^H \mathbf{H} \mathbf{F} \mathbf{X} + \tilde{\mathbf{N}}, \quad (1.13)$$

where $\tilde{\mathbf{n}} = \mathbf{W}^H \mathbf{n}$, $\mathbf{F} = \mathbf{F}_{\text{RF}} \mathbf{F}_{\text{BB}} \in \mathbb{C}^{N_T \times G_T}$, and $\mathbf{W} = \mathbf{W}_{\text{RF}} \mathbf{W}_{\text{BB}} \in \mathbb{C}^{N_R \times G_R}$ is the hybrid combiner. $\mathbf{X} = \sqrt{P} \mathbf{I}_{G_T}$ is the diagonal matrix containing G_T transmitted training symbols. Now substituting the value of \mathbf{H} from equation (1.3), the equation (1.13) can be written as

$$\mathbf{Y} = \mathbf{W}^H \mathbf{A}_R \mathbf{H}_\alpha \mathbf{A}_T^H \mathbf{F} \mathbf{X} + \tilde{\mathbf{N}}, \quad (1.14)$$

To exploit the sparsity of the mmWave channel, the received signal matrix in equation (1.13) is vectorized and expressed as [43]

$$\mathbf{y} = \sqrt{P} (\mathbf{F}^T \otimes \mathbf{W}^H) \mathbf{A}_D \mathbf{h}_\alpha + \tilde{\mathbf{n}}, \quad (1.15)$$

where equation (1.15) is obtained from applying the virtual channel representation

in equation (1.13), with quantised AoAs/AoDs taken from a uniform grid of M points, $\mathbf{A}_D = (\mathbf{A}_T^* \otimes \mathbf{A}_R) \in \mathbb{C}^{N_T N_R \times M^2}$. Further, $\mathbf{h}_\alpha = \text{vec}(\mathbf{H}_\alpha)$ denotes the $M^2 \times 1$ vector containing the path gains corresponding to the quantised directions. From equation (1.15), the channel estimation problem can be formulated as [13]

$$\min_{\mathbf{h}_\alpha} \|\mathbf{h}_\alpha\|_0, \quad \text{subject to } \|\mathbf{y} - \sqrt{P}(\mathbf{F}^T \otimes \mathbf{W}^H) \mathbf{A}_D \mathbf{h}_\alpha\|_2^2 \leq \epsilon, \quad (1.16)$$

Equations (1.16) describe the generalized channel estimation problem based on hybrid architecture. Additional constraints may be imposed depending on the hardware utilized for analog processing. Specifically, if phase shifters are employed, the RF precoding and combining matrices must feature unit norm entries. Conversely, if switches are used, each column of the RF precoding and combining matrices must contain exactly one at the index of the selected antenna and zero elsewhere [45]. However, our primary objective is to detect the non-zero elements of \mathbf{h}_α (i.e., the dominant paths of the channel) alongside their corresponding AoAs and AoDs to resolve the channel estimation problem outlined by equations (1.16). Thus, these equations present a sparse recovery problem, for which various approaches and their derivatives have been elucidated in the literature.

1.6 Sparse Channel Estimation Algorithms

Although CS is a new concept emerged recently, searching for the sparse solution to an under-determined system of linear equations has always been of significant importance in signal processing and statistics. The main idea is to obtain the sparse solution by adding sparse constraint. The sparsest solution can be acquired by taking l_0 norm into account

$$\min_{\mathbf{s}} \|\mathbf{s}\|_0, \quad \text{subject to } \mathbf{A}\mathbf{s} = \mathbf{y}, \quad (1.17)$$

where \mathbf{A} is sensing matrix, \mathbf{y} is received signal vector, and \mathbf{s} is a column vector. Unfortunately, this criterion is not convex, and the computational complexity of optimizing it is non-polynomial (NP) hard. To overcome this difficulty, l_0 norm has

to be replaced by simpler ones in terms of computational complexity. For example, the convex l_1 norm is used

$$\min_{\mathbf{s}} \|\mathbf{s}\|_1, \quad \text{subject to } \mathbf{A}\mathbf{s} = \mathbf{y}. \quad (1.18)$$

This idea is known as basis pursuit (BP), and it can be recasted as a linear programming (LP) issue. A recent body of related research shows that perhaps there are conditions guaranteeing a formal equivalence between the l_0 norm solution and the l_1 norm solution [46]. Many approaches and their variants to these problems have been described in the literature. They mainly fall into three basic categories.

1.6.1 Convex Relaxation

The first kind of convex optimization techniques for addressing problems (1.17)–(1.18) encompass interior-point (IP) methods [47], [48], which convert these problems into convex quadratic ones. While standard IP methods struggle with large-scale scenarios, numerous enhanced IP methods leverage rapid algorithms for matrix-vector operations, enabling them to handle such situations effectively, as evidenced in [49] and [50]. Noteworthy implementations of these IP methods, like l_1 -magic [51] and PDCO [52], utilize iterative algorithms such as conjugate gradients (CG) or LSQR algorithm [53] to determine the search step. A recently introduced IP method, distinct from earlier approaches, has emerged as the fastest for solving (1.18).

The alternative category of convex optimization methods for tackling problems (1.17)–(1.18) involves the homotopy method and its variations. The homotopy method traces the complete solution path for all non-negative scalar parameter values in the aforementioned problems. When the solution is notably sparse, methods outlined in [54–56] exhibit remarkable speed [57]. However, for large-scale problems, the path-following methods tend to be slow. Recent computational methodologies encompass coordinate-wise descent methods [58], fixed-point continuation methods [59], sequential subspace optimization methods [60], bound optimization methods [61], iterated shrinkage methods [62], gradient methods [63], gradient projection for sparse reconstruction algorithm (GPSR) [64], sparse reconstruction by separable

approximation (SpaRSA) [65], and the Bregman iterative method [66], [67]. Certain methods, like GPSR, SpaRSA, and the Bregman iterative method, demonstrate efficient handling of large-scale problems.

Beyond l_0 norm, another prevalent function for representing sparsity is l_1 norm. This problem is non-convex, often converted into a solvable convex problem. Common methods include FOCal under-determined system solver (FOCUSS) [68] and iteratively reweighted least squares (IRLS) [69], [70]. However, compared to norm-based approaches, these methods typically require more computational time.

1.6.2 Greedy Pursuits

Instead of globally minimizing an objective function, these approaches opt for a locally optimal selection following an approximation buildup at each iteration. Matching pursuit (MP) and orthogonal matching pursuit (OMP) [71], [72] represent early examples of greedy pursuit techniques, succeeded by advancements like stagewise OMP (StOMP) [73] and regularized OMP [74]. The computational complexity for reconstructing with these algorithms is lower than that of BP methods. However, achieving perfect reconstruction typically demands more measurements, and in certain scenarios, these methods may not pinpoint the sparsest solution, unlike optimization-based methods. More recently, subspace pursuit (SP) [75], compressive sampling matching pursuit (CoSaMP) [76], and the iterative hard thresholding method (IHT) [77] have emerged, incorporating backtracking concepts. Theoretically, they promise comparable reconstruction quality and lower reconstruction complexity akin to LP methods. Nonetheless, all these approaches assume the availability of the sparsity parameter, which may not always be the case in practical applications. Additionally, all greedy algorithms impose higher memory requirements.

1.6.3 Adaptive Algorithms

A key drawback of the many schemes proposed in the existing literature is that they estimate the mmWave MIMO channel only after receiving all the pilot beams, thereby increasing the processing delay. Moreover, the existing sparse channel estimation schemes such as MP, OMP, Bayesian compressive sensing (BCS), and

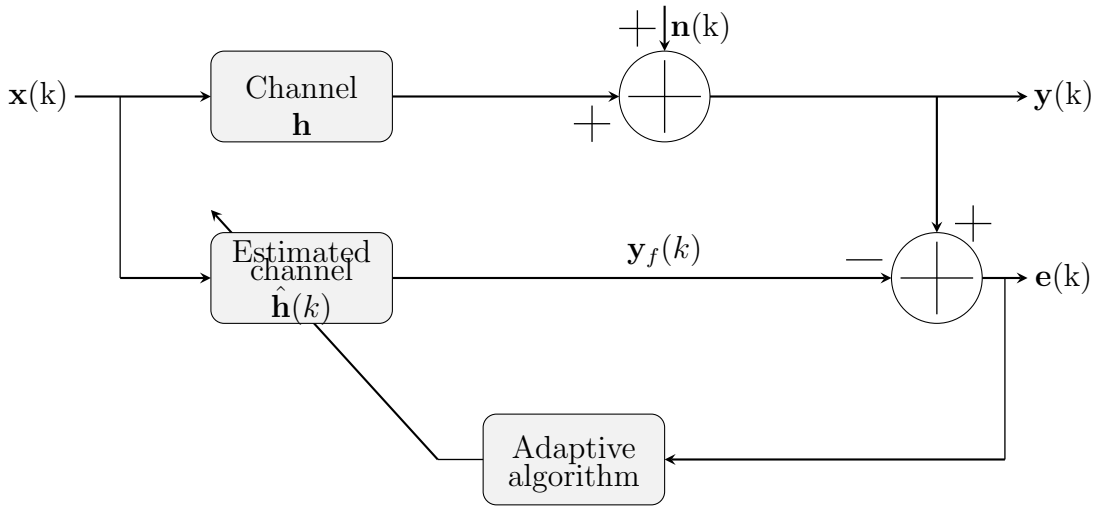


Figure 1.6: Block diagram channel estimation using adaptive algorithms.

sparse Bayesian learning (SBL) are computationally complex due to the requirement of several matrix inversions. Hence, to overcome the drawbacks of the existing schemes adaptive online channel estimation techniques capable of accurate tracking and learning capabilities and also offer low complexity are eminently suitable for practical channel estimation. The two capabilities of learning and tracking are the main reasons behind the widespread use of stochastic-gradient methods (and the corresponding adaptive filters). It is because of these abilities that tend to describe adaptive filters as “smart systems”; smart in the sense that they can learn the statistics of the underlying signals and adjust their behavior to variations in the “environment” in order to keep the performance level at check.

- In adaptive channel estimation, the estimator dynamically adjusts its parameters or characteristics based on the received signals and feedback information to accurately track changes in the channel conditions. This adaptability is essential in environments where the channel characteristics may vary over time due to factors like mobility, environmental changes, or interference.
- The motivation behind adaptive estimator is to reduce complexity, minimize delays, and enhance both estimation accuracy and spectral efficiency.
- Basic update equation is given as follows

$$\hat{\mathbf{h}}_{\text{next}} = \hat{\mathbf{h}}_{\text{prev}} + (\text{step size})(\text{input vector})(\text{observation error}). \quad (1.19)$$

Equivalently, the result may be written in the form of three basic relations as follows:

1. Filter output:

$$\mathbf{y}_f(k) = \hat{\mathbf{h}}^H(k)\mathbf{x}(k) \quad (1.20)$$

2. Estimation error:

$$\mathbf{e}(k) = \mathbf{y}(k) - \mathbf{y}_f(k) \quad (1.21)$$

3. Tap-weight adaptation:

$$\hat{\mathbf{h}}(k+1) = \hat{\mathbf{h}}(k) + \mu\mathbf{x}(k)\mathbf{e}(k) \quad (1.22)$$

Equations (1.20) and (1.21) define the estimation error $\mathbf{e}(k)$, the computation of which is based on the current estimate of the tap-weight vector, $\hat{\mathbf{h}}(k)$. The second term, $\mu\mathbf{x}(k)\mathbf{e}(k)$, on the right-hand side of equation (1.22) represents the correction that is applied to the current estimate of the tap-weight vector, $\hat{\mathbf{h}}(k)$. The iterative procedure is started with an initial guess $\hat{\mathbf{h}}(0)$. As from equation (1.22), no matrix inversion is involved in adaptation process, hence, it offers lower computation cost.

1.7 Intelligent Reflecting Surface

In mmWave communications, large antenna arrays are typically used to generate highly directional beams that compensate for substantial path loss compared to the sub-6 GHz band. However, this high directivity makes mmWave communication more susceptible to signal obstruction from foliage, men, car, and buildings. To overcome the blockage intelligent reflecting surface (IRS) is seen as a promising solution. The IRS is one of the most promising and revolutionizing paradigm to achieve smart and reconfigurable wireless channel/radio propagation environments for beyond 5G/6G wireless communication systems [2]. It can enhance the spectrum and/or energy efficiency of wireless communication systems. IRS is a planar surface composed of various passive reflecting elements (REs), where each of the REs can independently influence the incident signal to vary in amplitude and/or phase. The reflected signals can be reconfigured to propagate in the desired directions by carefully adjusting the amplitude/phase shifts of all the REs. The wireless channels

between transmitters and receivers can be easily modified by smartly placing IRSs in a network and carefully coordinating their reflection coefficients. Due to rapid developments in metamaterials, the reflection coefficient of each element can be re-configured in real-time to adapt the dynamically fluctuating wireless propagation environment.

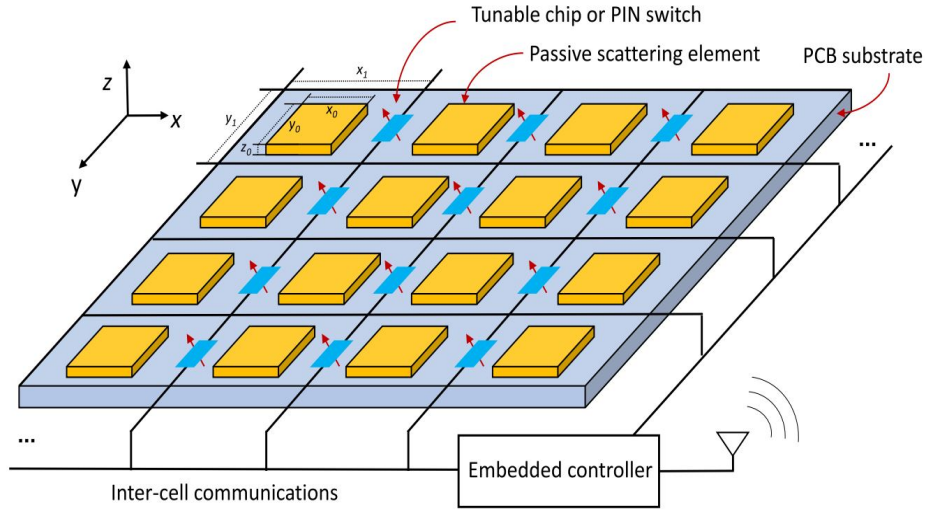


Figure 1.7: Reconfigurable metasurface with substantial number of passive scattering/reflecting elements.

The metasurface is a type of two-dimensional (i.e., with nearly zero thickness) artificial material that shows special electromagnetic properties depending on its structural parameters. As shown in Figure 1.7, the metasurface is made up of a large number of passive scattering elements or REs, such as metallic or dielectric particles, which can alter the impinging electromagnetic waves in various ways [78]. The direction and strength of the reflected waves are governed by the sub-wavelength structural arrangement of the REs, which affects how the incident waves are transformed. The IRS is made of a programmable metasurface that allows for complete control over the phase shifts experienced by various REs. This can be accomplished by applying external stimuli to the REs, which will modify their physical parameters and change the metasurface's electromagnetic properties without refabrication. A joint phase control of the REs allows the IRS to reconfigure its electromagnetic characteristics. This suggests integrating tunable chips into the metasurface's structure, with each tunable chip interacting locally with a RE and communicating with a central controller i.e., IRS controller [79]. In particular, the IRS controller can be

implemented in a field-programmable gate array and the tunable chips are typical PIN or varactor diodes. As shown in Figure 1.7, the embedded IRS controller can communicate and receive reconfiguration requests from external devices, and then optimize and distribute its phase control decisions to all tunable chips. Each tunable chip modifies its state after receiving the control input, allowing the corresponding scattering element to alter its behavior. The IRS controller can use this sensing data to automatically alter its configuration and maintain consistent EM behavior with dynamic environmental conditions. By adjusting the phase of specific REs, the IRS can be reconfigured. The inter-cell communication among the tunable chips works together to control the REs of the metasurface that exhibits the desired tunable functions for the IRS's reconfigurability. A wide variety of tunable functions such as perfect absorption, anomalous reflection, beam shaping, and steering can be supported by the IRS [80]. The advantages of IRS-aided systems can be summarized as:

1) Flexible reconfiguration: The phase shift of all the REs i.e., passive beamforming can be achieved by coherent focused signal reflection in the desired receiver and null in the other directions. It can play an important role in performance improvement in wireless communication. The transmit beamforming, resource allocation, and power allocation can be jointly optimized to achieve performance gains [78].

2) Easy to deploy: The IRS is made of low-cost passive REs embedded in the metasurface. It is highly flexible in terms of both deployment and replacement because it can take on any shape. The IRS can be deployed on several structures such as building facades, indoor walls, aerial platforms, roadside billboards, highway polls, vehicle windows, etc.

3) Spectral/Energy efficiency enhancement: The IRS can modify the wireless propagation environment by compensating for the power loss over long distances. The sum-rate performance and better QoS can be achieved by the IRS-assisted wireless network. In contrast to AF and DF relaying protocols, IRS is capable of shaping the incoming signal by controlling the phase shift of each RE instead of employing a power amplifier. Thus, deploying IRS is more energy-efficient and environmentally friendly than AF and DF systems.

4) Compatibility: The IRS supports a full-duplex (FD) mode of operation for transmission because it can only reflect electromagnetic waves. Additionally, IRS-aided wireless communication systems are compatible with the standards and hardware of existing wireless networks [81].

1.8 Hardware Imperfections

In practice, hardware suffers from various types of imperfections that limit the performance of wireless communication systems. In this section, various hardware imperfections such as high power amplifier (PA) non-linearity and transceiver hardware impairments (HIs) are discussed.

1.8.1 Non-Linear Power Amplifier

In wireless communication, when the information signal is propagated through the wireless channel, it may suffer from significant path loss in the medium as well as long-distance communication due to the fading impairments of the channel. To minimize this path loss, highly efficient PAs are used at the transmitter. In practice, there is a finite peak level for which any PA can produce output power without exceeding that power constraint. This peak constraint varies within a specific defined range and is mostly amplifier-dependent. A non-linear distortion (NLD) over the peak is introduced if the amplifier is unable to supply the required power [82]. The high PA can be categorized into memoryless and with memory. In the case of memoryless, the frequency response of the amplifier is constant over the operating frequency range and can be modeled as Rapp models such as soft envelope limiter, traveling wave tube amplifier, and solid-state PA [83]. On the other hand, in the case of memory, the frequency response of the amplifier depends on the frequency component and can be modeled as the Volterra, Wiener, Hammerstein, and memory polynomial models [84]. Further, according to the Bussgang linearization theory, the output of the NLPA circuit can be expressed in terms of a linear scale parameter A_D of the input signal and a non-linear distortion N_D which is uncorrelated with

the input signal [83]. The output of the NLPA can be expressed as

$$y^{\text{NLPA}} = A_D x + N_D, \quad (1.23)$$

where A_D is a constant and $N_D \sim \mathcal{CN}(0, \sigma_N^2)$.

1.8.2 Transceiver Hardware Impairments

Transceiver signal in practical mmWave hybrid MIMO system experience distortion due to imperfect behavior of hardware components such as, mixer, oscillator, filter, converter, and amplifier. Many compensation techniques can be applied at the transceiver to mitigate the impairment, even after some residual impairments remain. Total residual impairments at the transceiver are modeled as independent additive distortion noise as done in [85] and [86]. The distortion noise is well-known to be non-stationary because it is proportional to the instantaneous signal power P and the current channel gain $\|\mathbf{H}\|_2^2$.

A generalized system model that represents the impact of residual transceiver impairments is given in Figure 1.8,

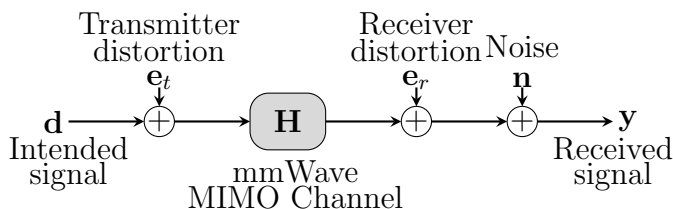


Figure 1.8: Generalized transmission with hardware impairments.

where \mathbf{e}_t and \mathbf{e}_r denotes the additive distortion noise due to residual impairments at the transmitter and the receiver. From the existing works [85], it is known that $\mathbf{e}_t \sim \mathcal{CN}(\mathbf{0}_{N_T}, \mathbf{\Upsilon}_t)$ and $\mathbf{e}_r \sim \mathcal{CN}(\mathbf{0}_{N_R}, \mathbf{\Upsilon}_r)$ follows a Gaussian distribution with its average power proportional to the average signal power at each antenna where $\mathbf{\Upsilon}_t = \kappa_t \text{diag}(q_{1,1}, q_{2,2}, \dots, q_{N_T, N_T})$, $\mathbf{\Upsilon}_r = \kappa_r \mathbf{H}^H \text{tr}\{\mathbf{Q}\} \mathbf{H}$, $\kappa_t, \kappa_r \geq 0$ are proportionality coefficients, and $(q_{1,1}, q_{2,2}, \dots, q_{N_T, N_T})$ are the diagonal elements of signal covariance matrix \mathbf{Q} . The proportionality coefficient κ_t and κ_r are related to the error vector magnitude (EVM) and characterize the level of hardware impairments. The EVM

at transmitter is given by [85]

$$\text{EVM} = \sqrt{\frac{\mathbb{E}\{\|\mathbf{e}_t\|_2^2\}}{\mathbb{E}\{\|\mathbf{x}\|_2^2\}}} = \sqrt{\frac{\kappa_t \text{tr}\{\mathbf{Q}\}}{\text{tr}\{\mathbf{Q}\}}} = \sqrt{\kappa_t}. \quad (1.24)$$

For practical application such as long term evolution (LTE), the EVM has a range of [0.08, 0.175] [87].

The mmWave hybrid MIMO system with considered transceiver hardware impairments can be accurately modeled as,

$$\mathbf{y} = \mathbf{W}^H \mathbf{H}(\mathbf{x} + \mathbf{e}_t) + \mathbf{W}^H \mathbf{e}_r + \mathbf{W}^H \mathbf{n}. \quad (1.25)$$

Since low-cost hardware is used in practical deployed mmWave systems MIMO, which leads to large EVM, which, in-turn limits the system performance [85].

1.9 Motivation

Millimeter-wave (mmWave) communication holds great promise for enabling high data rates and ultra-low latency in wireless networks. However, mmWave signals are highly susceptible to path loss and blockage, making channel estimation a critical challenge, especially in complex MIMO systems. Here are some specific motivations for adaptive sparse channel estimation in mmWave hybrid MIMO systems:

Exploiting Channel Sparsity: In mmWave channels, due to the high path loss and sparse scattering environment, the channel impulse response often exhibits sparsity. Leveraging this sparsity can significantly reduce the overhead and complexity of channel estimation, making it essential to develop adaptive sparse channel estimation algorithms according to mmWave environments.

Reducing Overhead: Traditional channel estimation methods often require extensive training sequences, which consume valuable resources in mmWave systems with limited bandwidth. Adaptive sparse channel estimation can mitigate this overhead by efficiently estimating the channel with fewer measurements, allowing more resources to be allocated to data transmission.

Improving System Performance: Accurate channel estimation is crucial for beamforming, spatial multiplexing, and interference suppression in MIMO systems.

Adaptive sparse channel estimation techniques can provide more reliable estimates, leading to improved system performance in terms of throughput, coverage, and reliability.

Enabling Dynamic Environments: mmWave channels are inherently dynamic, with rapidly changing propagation conditions due to blockages and mobility. Adaptive sparse channel estimation algorithms can adapt to these variations in real-time, ensuring robust performance even in dynamic environments.

In addition to the challenges posed by mmWave propagation, hardware impairments in transceivers can further degrade the performance of MIMO systems. Here's why adaptive sparse channel estimation is crucial in such scenarios:

Compensating for Imperfect Hardware: Non-linear power amplifiers, phase noise, and other hardware impairments can distort the received signals, leading to inaccuracies in channel estimation. Adaptive sparse channel estimation algorithms can mitigate these effects by adaptively adjusting to the imperfections in the hardware.

Maintaining Performance: Hardware impairments can degrade the performance of conventional channel estimation techniques, leading to increased error rates and reduced system capacity. Adaptive sparse channel estimation algorithms can maintain performance by exploiting the sparsity of the channel while compensating for hardware imperfections.

Reducing Complexity: Traditional channel estimation methods may require complex calibration procedures or extensive computational resources to compensate for hardware impairments. Adaptive sparse channel estimation algorithms offer a lower-complexity alternative that can operate efficiently even in the presence of hardware imperfections.

IRS have emerged as a promising technology for enhancing the performance of mmWave communication systems. Here's why adaptive sparse channel estimation is crucial in IRS-aided mmWave hybrid MIMO systems:

Exploiting Spatial Diversity: IRS introduces additional degrees of freedom by manipulating the phase of reflected signals, enabling spatial diversity and improving the performance of mmWave MIMO systems. Adaptive sparse channel estimation allows efficient utilization of this spatial diversity by accurately estimating the chan-

nels between the transmitter, reflectors, and receiver.

Handling Increased Complexity: IRS-aided mmWave systems introduce additional complexity due to the presence of multiple reflecting elements. Adaptive sparse channel estimation techniques can handle this increased complexity by efficiently estimating the channels while exploiting the sparsity of the channel responses.

Adapting to Dynamic Environments: IRS configurations can be dynamically adjusted to optimize system performance in response to changing environmental conditions. Adaptive sparse channel estimation algorithms enable real-time adaptation to these changes, ensuring robust performance in dynamic environments.

Improving System Efficiency: By accurately estimating the channels between the transmitter, IRS, and receiver, adaptive sparse channel estimation contributes to maximizing the spectral efficiency and overall system capacity of IRS-aided mmWave hybrid MIMO systems.

The motive of this thesis is to address various issues of channel estimation in mmWave hybrid MIMO system and IRS-aided mmWave hybrid MIMO system.

1.10 Thesis Flowchart, Outline, and Contributions

The flowchart of the thesis is shown in Figure 1.9 which shows the system model and proposed channel estimator for that. The thesis is organized into 6 chapters, which are briefly described with their contributions as follows:

Chapter 1. Introduction : In Chapter 1, a brief introduction to mmWave wireless communication, hybrid MIMO, mmWave hybrid MIMO channel, IRS, hardware imperfections such as non-linear power amplifiers and transceiver hardware impairments, compressive sensing, adaptive channel estimation, and finally, the motivation and major contributions of the work presented in the thesis are provided.

Chapter 2. ZALMS Based Channel Estimator for mmWave Hybrid MIMO System: In this chapter, we propose ZALMS-based sparse channel estimation algorithms for narrowband mmWave hybrid MIMO systems. We analyze and validate its mean square error (MSE) through simulations over mmWave MIMO systems. Additionally, we present simulation results for MSE versus the number of

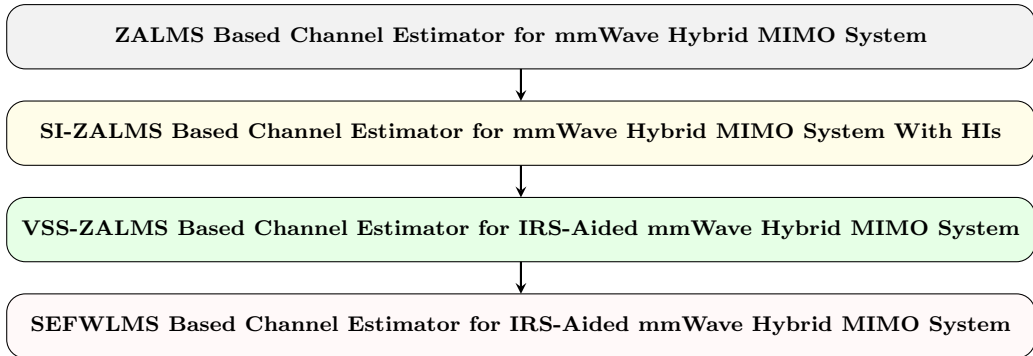


Figure 1.9: Flowchart of the thesis.

iterations and spectral efficiency (SE) versus SNR to assess estimation accuracy and overall system performance.

Chapter 3. SI-ZALMS Based Channel Estimator for mmWave Hybrid MIMO System With HIs: This chapter investigates the impact of various hardware impairments on mmWave hybrid MIMO systems at the transceiver while estimating narrowband mmWave hybrid MIMO channels. We propose low-complexity adaptive online channel estimators based on ZALMS to exploit the sparsity of mmWave hybrid MIMO systems. Furthermore, to enhance the convergence of ZALMS, SI-ZALMS is proposed. The theoretical mean square deviation (MSD) and MSE, along with the related equations for their asymptotic values, are determined. Analytical ranges are derived for possible step-size and regularization parameter values. Additionally, simulations are provided to assess accuracy and SE for different levels of impairments. Lastly, the impact of RTHI on SE is derived and analytically validated.

Chapter 4. VSS-ZALMS Based Channel Estimator for IRS-Aided mmWave Hybrid MIMO System: In this chapter, we explore the challenges of channel estimation in a millimeter-wave hybrid MIMO system aided by IRS. We formulate a sparse recovery problem from the cascaded channel estimation problem and propose the VSS-ZALMS algorithm. To achieve lower normalized MSE (NMSE) and a faster convergence rate, we derive the range of regularization and step-size parameters for the VSS-ZALMS-based estimator. Additionally, we analyze the computational complexity, IRS location, and SE for the considered system. Finally, we present the SE versus SNR and SE versus the number of reflecting elements' per-

formance for several estimators.

Chapter 5. SEFWLMS Based Channel Estimator for IRS-Aided mmWave Hybrid MIMO System: This chapter investigates the channel estimation problem of the IRS-aided mmWave hybrid MIMO system. For the system under consideration, we utilize the characteristics of Kronecker products to develop a cascaded channel estimation approach. Further, to solve the CS reconstruction problem, which can be viewed as a sparse channel estimation problem, we propose an adaptive online sparse forgetting window least mean square (SEFWLMS)-based channel estimator. This estimator is an l_0 -variant of the exponential forgetting window least mean square (EFWLMS) algorithm for sparse channel identification. The proposed technique offers lower computational complexity and storage, resulting in higher estimation speed (i.e., lower latency) since no matrix inversion is involved in the composite channel estimation. Lastly, the SE versus SNR and NMSE versus SNR performance for several estimators are presented.

Chapter 6. Conclusions and Future Works: All the contributions of the thesis have been summarized in this chapter, and important insights and conclusions have been presented. Furthermore, the scope for future work is also discussed.

Chapter 2

ZALMS based Channel Estimator for mmWave Hybrid MIMO System

Next generation (5G/B5G) wireless networks promise disruptively high data rates, ultra reliable low latency communication, and enhanced machine type communication [88]. To this end, mmWave multiple input multiple output (MIMO) is a key physical layer method to fulfill the above demands for 5G and B5G wireless systems [89]. In particular, mmWave signals refer to wavelengths from 1 mm to 10 mm, and corresponding to frequencies approximately in the range of 30–300 GHz [90]. Due to the availability of a large bandwidth in the mmWave band, this allows for high data rates and dense connectivity, which enhances its suitability for backhaul, fronthaul, transportation networks, indoor wireless system such as wireless personal area network (WPAN) IEEE 802.15.3c, wireless local area network(WLAN) IEEE 802.11ad, sensor networks, and 5G new radio (5G NR) [91]. Despite the aforementioned applications and potentials for ultra high data rates, the mmWave MIMO systems are impaired due to high path loss, severe penetration loss, extremely high power consumption, and hardware impairments [90], which need to be addressed to achieve high data rates. The high propagation loss in the mmWave MIMO systems is generally mitigated by a large antenna array that is mounted in a tiny area due to the typically small wavelength of mmWave frequencies.

Besides, the mmWave channel is known to be sparse due to scattering and block-

age [13]. Due to this sparsity, channel matrices only have some dominant singular values which makes them deficient [92], i.e., the effective singular values are considerably smaller than the total number of transmitting and receiving antennas [93, 94]. Based on the above facts, hybrid precoding and combining is proposed which is a cascade of the digital and analog beamformer for mmWave MIMO system [19], [95]. The rank of the channel matrix determines the number of RF chains in a hybrid structure. For designing hybrid precoding and combining, accurate channel state information (CSI) are required [19], which is generally obtained through channel estimation. Works on channel estimation has been investigated in various research works such as [13, 43, 93, 96, 97]. In details, the traditional channel estimation methods, such as the minimum mean square error (MMSE) and least square (LS) based methods are complex for mmWave MIMO systems due to inversion of large channel matrices. This impairs the convergence and the practical viability of these approaches, since these methods do not exploit the inherent channel sparsity, and are thus ill-suited for the channel estimation for mmWave MIMO [13]. Among existing works, the techniques aligned with multiple signal classification are ill-suited for this purpose due to their sensitivity to antenna position and antenna gain [96]. Also, greedy algorithm based methods, such as OMP and its variants, heavily depend on the selection of stopping criteria and minor variations cause large convergence errors that lead to performance degradation [98]. Further, existing works report a large processing delay due to offline processing that allows for channel estimation after receiving all pilot beams, which adds to their complexity due to matrix inversion operations.

The key contributions of this work are summarized as follows:

- Motivated by the inherent tracking capability and low computational complexity, this work develops novel ZALMS-based adaptive channel estimation schemes for narrowband mmWave hybrid MIMO systems. To this end, a computationally efficient channel estimation model is developed for narrowband mmWave hybrid MIMO systems, which substantially simplifies the channel estimation procedure.
- A sparse channel estimation model is developed using the beamspace domain model of the mmWave MIMO channel, which utilizes a suitable sparsifying

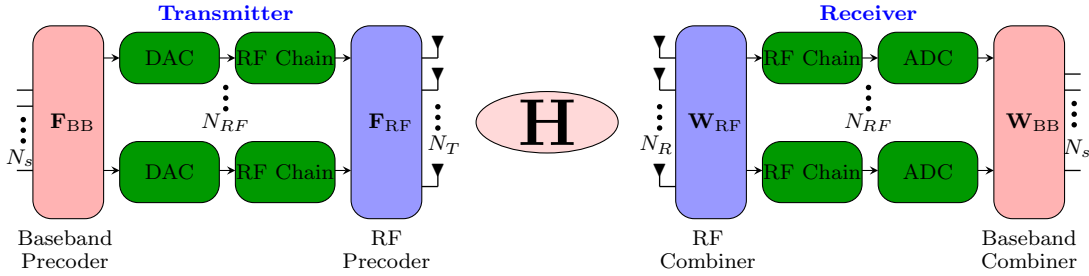


Figure 2.1: Block diagram of mmWave hybrid MIMO transceiver.

dictionary comprised of the quantized receive and transmit array response vectors.

- The proposed ZALMS technique does not require knowledge of the first and second order statistical information of the narrowband mmWave hybrid MIMO channel, and therefore it is eminently suited for both stationary and non-stationary environments, strengthening its practical importance.
- Analytical bound and simulation results are presented for characterizing the performance of the proposed ZALMS based schemes, which are benchmarked against the existing techniques.

2.1 System Model

The system architecture of the considered model is given in Figure 2.1 that consists of N_T transmit antennas, N_R receive antennas, with N_{RF} denoting the number of RF chains at the transmitting and receiving side. Further, let N_S denote the number of parallel data streams, which is less than or equal to number of RF chains assuming that the number of RF chains is small compared to number of transmit and receive antenna, $N_S \leq N_{RF} \ll \min(N_T, N_R)$ [43]. The RF precoder $\mathbf{F}_{RF} \in \mathbb{C}^{N_T \times N_{RF}}$ and the baseband precoder $\mathbf{F}_{BB} \in \mathbb{C}^{N_{RF} \times N_S}$ are cascaded at the transmitter. Additionally, the receiver consists of a baseband combiner $\mathbf{W}_{BB} \in \mathbb{C}^{N_{RF} \times N_S}$ and an RF combiner $\mathbf{W}_{RF} \in \mathbb{C}^{N_R \times N_{RF}}$. The RF precoder and combiner matrices consist of networks of digitally controlled phase shifters and are assumed to have constant magnitudes [13].

In this work, downlink channel estimation problem with a single transmitter (BS) and receiver (MS) equipped with a uniform linear antenna array (ULA) is consid-

ered. We consider a dense urban environment scenario; in particular, we consider a narrow band geometric channel model with L scatterers, with each scatterer contributing a single propagation path between the transmitter or base station (BS) and the receiver or mobile station (MS). The channel \mathbf{H} is expressed as follows [43]:

$$\mathbf{H} = \sqrt{\frac{N_T N_R}{\beta}} \sum_{l=1}^L \alpha_l \mathbf{a}_R(\theta_l) \mathbf{a}_T^H(\phi_l), \quad (2.1)$$

where α_l is the path gain of l^{th} path and its amplitude is assumed to be Rayleigh distributed and β is the average path loss between transmitter (BS) and receiver (MS). The variables $\theta_l \in [0, 2\pi]$ and $\phi_l \in [0, 2\pi]$ are the azimuth angle of arrival/departure (AoA/AoD) of the transmitter and receiver respectively. $\mathbf{a}_R(\theta_l)$ and $\mathbf{a}_T(\phi_l)$ are the antenna array response vector at the transmitter and receiver. $\mathbf{a}_R(\theta_l)$ can be written as

$$\mathbf{a}_R(\theta_l) = \frac{1}{\sqrt{N_R}} [1, e^{-j2\pi(d/\lambda)\cos(\theta_l)}, \dots, e^{-j(N_R-1)2\pi(d/\lambda)\cos(\theta_l)}], \quad (2.2)$$

where d is antenna spacing and λ is the signal wavelength. $\mathbf{a}_T(\phi_l)$, can be written in similar way.

The channel (2.1) is represented in the beamspace domain as

$$\mathbf{H} = \mathbf{A}_R \mathbf{H}_a \mathbf{A}_T^H, \quad (2.3)$$

where \mathbf{H}_a is the beamspace channel matrix it is sparse in nature, \mathbf{A}_R and \mathbf{A}_T are the receive and transmit array response dictionary matrices can be given as,

$$\mathbf{H}_a = \text{diag}\left(\sqrt{\frac{N_T N_R}{\beta}} [\alpha_1, \alpha_2, \dots, \alpha_L]^T\right), \quad (2.4)$$

$$\mathbf{A}_T = [\mathbf{a}_T(\phi_1), \mathbf{a}_T(\phi_2), \dots, \mathbf{a}_T(\phi_L)], \quad (2.5)$$

and

$$\mathbf{A}_R = [\mathbf{a}_R(\theta_1), \mathbf{a}_R(\theta_2), \dots, \mathbf{a}_R(\theta_L)]. \quad (2.6)$$

2.1.1 Sparse Formulation for mmWave Channel Estimation

We consider the span of AoD and AoA to be partitioned into G points at both transmitter and receiver in the interval $[0, \pi)$ with $G \geq \max\{N_T, N_R\}$. Further, we consider a uniformly spaced AoD grid Φ_T and AoA grid Θ_R that are defined as

$$\Phi_T = \left\{ \phi_g : \phi_g = \frac{\pi(g-1)}{G}, \forall 1 \leq g \leq G \right\} \quad (2.7)$$

and

$$\Theta_R = \left\{ \theta_g : \theta_g = \frac{\pi(g-1)}{G}, \forall 1 \leq g \leq G \right\} \quad (2.8)$$

We further denote $\mathbf{A}_R(\Theta_R) \in \mathbb{C}^{N_R \times G}$ and $\mathbf{A}_T(\Phi_T) \in \mathbb{C}^{N_T \times G}$ as receive and transmit array response dictionary matrices, that are defined as $\mathbf{A}_R(\Theta_R) = [\mathbf{a}_R(\theta_1), \mathbf{a}_R(\theta_2), \dots, \mathbf{a}_R(\theta_G)]$ and $\mathbf{A}_T(\Phi_T) = [\mathbf{a}_T(\phi_1), \mathbf{a}_T(\phi_2), \dots, \mathbf{a}_T(\phi_G)]$. The transmit and receive array response dictionary matrices satisfy the condition $\mathbf{A}_T(\Phi_T)\mathbf{A}_T^H(\Phi_T) = \frac{G}{N_T}\mathbf{I}_{N_T}$ and $\mathbf{A}_R(\Theta_R)\mathbf{A}_R^H(\Theta_R) = \frac{G}{N_R}\mathbf{I}_{N_R}$ [99].

In the beamspace domain the channel matrix \mathbf{H} can be represented as (ignoring the quantization error):

$$\mathbf{H} = \mathbf{A}_R(\Theta_R)\mathbf{H}_b\mathbf{A}_T^H(\Phi_T), \quad (2.9)$$

where $\mathbf{H}_b \in \mathbb{C}^{G \times G}$ is the equivalent beamspace channel matrix corresponding to \mathbf{H} . Then vectorized form of channel is represented as $\mathbf{h} = \text{vec}(\mathbf{H}) = (\mathbf{A}_T^*(\Phi_T) \otimes \mathbf{A}_R(\Theta_R))\mathbf{h}_b$, where $\mathbf{h}_b \triangleq \text{vec}(\mathbf{H}_b) \in \mathbb{C}^{G^2 \times 1}$ is beamspace vector. Further, the beamspace channel vector \mathbf{h}_b is considered sparse. The pilot matrix $\sqrt{P}\mathbf{I}_{N_T}^{Beam}$ and the output signal matrix \mathbf{Y} are given by:

$$\mathbf{Y} = \sqrt{P}\mathbf{W}_{BB}^H\mathbf{W}_{RF}^H\mathbf{H}\mathbf{F}_{RF}\mathbf{F}_{BB}\mathbf{I}_{N_T}^{Beam} + \mathbf{N}, \quad (2.10)$$

where \mathbf{W}_{BB} , \mathbf{W}_{RF} are baseband and RF combining matrices and \mathbf{F}_{BB} , \mathbf{F}_{RF} are baseband and RF precoding matrices and \mathbf{N} is noise matrix. For channel estimation, it is necessary to vectorize the received signal matrix \mathbf{Y} [93]:

$$\mathbf{y} = \sqrt{P}\mathbf{Q}\mathbf{h}_b + \mathbf{n}, \quad (2.11)$$

where $\mathbf{y} = \text{vec}(\mathbf{Y}) \in \mathbb{C}^{N_T^{Beam} N_R^{Beam} \times 1}$, $\mathbf{h}_b = \text{vec}(\mathbf{H}_b) \in \mathbb{C}^{N_T N_R \times 1}$ and $\mathbf{Q} = \mathbf{F}_{BB}^T \mathbf{F}_{RF}^T \mathbf{A}_T^* \otimes \mathbf{W}_{BB}^H \mathbf{W}_{RF}^H \mathbf{A}_R \in \mathbb{C}^{N_T^{Beam} N_R^{Beam} \times N_T N_R}$ is equivalent sensing matrix, that is written from the identity, $\text{vec}(\mathbf{PQR}) = (\mathbf{R}^T \otimes \mathbf{P})\text{vec}(\mathbf{Q})$, $\mathbf{n} = \text{vec}(\mathbf{N})$. In the next section, online adaptive filtering based framework of LMS and ZALMS for mmWave MIMO channel estimation is developed.

2.2 Adaptive Filtering Framework for Channel Estimation

2.2.1 LMS Framework for mmWave Hybrid MIMO System

Let $\hat{\mathbf{h}}$ denote estimate of channel \mathbf{h}_b . Let mean square error (MSE) cost function be defined as:

$$J(k) = \mathbb{E}\{\|\mathbf{y}(k) - \mathbf{Q}^H(k)\hat{\mathbf{h}}(k)\|^2\}. \quad (2.12)$$

After applying the steepest descent algorithms [100], the estimate $\hat{\mathbf{h}}(k)$ is updated as:

$$\hat{\mathbf{h}}(k+1) = \hat{\mathbf{h}}(k) - \frac{\mu}{2} \nabla_{\hat{\mathbf{h}}(k)}(J(k)), \quad (2.13)$$

where μ is step size parameter. Upon defining auto covariance matrix

$$\mathbf{R} = \mathbb{E}\{\mathbf{Q}^H(k)\mathbf{Q}(k)\} \in \mathbb{C}^{G^2 \times G^2}$$

and cross covariance vector $\mathbf{p} = \mathbb{E}\{\mathbf{Q}^H(k)\mathbf{y}(k)\} \in \mathbb{C}^{G^2 \times 1}$, gradient of the cost function $J(k)$ is given by:

$$\nabla_{\hat{\mathbf{h}}(k)}(J(k)) = 2\mathbf{R}\hat{\mathbf{h}}(k) - 2\mathbf{p}. \quad (2.14)$$

By substituting the value of gradient of the cost function from (2.14) to (2.13) the weight update equation is given as:

$$\hat{\mathbf{h}}(k+1) = \hat{\mathbf{h}}(k) + \mu(\mathbf{p} - \mathbf{R}\hat{\mathbf{h}}(k)). \quad (2.15)$$

Upon using the stochastic gradient approach \mathbf{R} and \mathbf{p} are replaced by their instantaneous estimates, $\hat{\mathbf{R}} = \mathbf{Q}^H(k)\mathbf{Q}(k)$ and $\hat{\mathbf{p}} = \mathbf{Q}^H(k)\mathbf{y}(k)$. By putting the instantaneous values of auto covariance matrix and cross covariance vector final expression for weight update equation is given as:

$$\hat{\mathbf{h}}(k+1) = \hat{\mathbf{h}}(k) + \mu\mathbf{Q}^H(k)\mathbf{e}(k), \quad (2.16)$$

where $\mathbf{e}(k) \in \mathbb{C}^{N_{RF} \times 1}$ is the instantaneous observation error vector given by:

$$\mathbf{e}(k) = \mathbf{y}(k) - \mathbf{Q}^H(k)\hat{\mathbf{h}}(k). \quad (2.17)$$

2.2.2 Proposed ZALMS Framework for mmWave Hybrid MIMO System

Assuming that \mathbf{h}_b is a sparse vector, the channel estimation problem is described as a non-convex combinatorial problem that is formulated as:

$$\min_{\mathbf{h}_b} \|\mathbf{h}_b\|_0, \quad \text{s.t. } \|\mathbf{y} - \mathbf{Q}\mathbf{h}_b\|_2^2 \leq \epsilon, \quad (2.18)$$

where $\epsilon > 0$ is error tolerance parameter. Different offline methods for sparse signal recovery, such as OMP [93] and SBL [101] etc., exist in the literature to solve the above problem. However, these algorithms cause a high propagation delay due to their offline nature and prohibitively high computational complexity due to matrix inversions in each iteration. The ZALMS framework, which is developed next, addresses these issues. The MSE cost function for ZALMS [102] is therefore defined as:

$$J_{ZA}(k) = \mathbb{E}\{\|\mathbf{y}(k) - \mathbf{Q}^H(k)\hat{\mathbf{h}}(k)\|^2\} + \gamma f(\hat{\mathbf{h}}(k)), \quad (2.19)$$

where γ is regularization parameter and $f(\cdot)$ is sparsity inducing penalty term. After employing steepest descent algorithm [100] the estimate $\hat{\mathbf{h}}(k+1)$ is iteratively updated as:

$$\hat{\mathbf{h}}(k+1) = \hat{\mathbf{h}}(k) - \frac{\mu}{2}\nabla_{\hat{\mathbf{h}}(k)}(J_{ZA}(k)). \quad (2.20)$$

The gradient of this cost function is expressed as follows:

$$\nabla_{\hat{\mathbf{h}}(k)}(J_{ZA}(k)) = 2\mathbf{R}\hat{\mathbf{h}}(k) - 2\mathbf{p} - \rho g(f(\hat{\mathbf{h}}(k))), \quad (2.21)$$

where $g(f(\hat{\mathbf{h}}(k))) = \nabla_{\hat{\mathbf{h}}(k)}(f(\hat{\mathbf{h}}(k)))$ represents the gradient of the sparsity inducing penalty function $f(\cdot)$ and $\rho = \frac{\gamma\mu}{2}$ denotes regularization step size. By substituting the value of gradient of the cost function from (2.21) to (2.20), weight update equation is simplified as:

$$\hat{\mathbf{h}}(k+1) = \hat{\mathbf{h}}(k) + \mu(\mathbf{p} - \mathbf{R}\hat{\mathbf{h}}(k)) - \rho g(f(\hat{\mathbf{h}}(k))). \quad (2.22)$$

Applying stochastic-gradient approach, final update expression can be obtained as:

$$\hat{\mathbf{h}}(k+1) = \hat{\mathbf{h}}(k) + \mu\mathbf{Q}^H(k)\mathbf{e}(k) - \rho g(f(\hat{\mathbf{h}}(k))), \quad (2.23)$$

where $\mathbf{e}(k)$ similar to (2.17), represents the instantaneous observation error.

Algorithm 1 Proposed ZALMS Algorithm

Input: Received signal $\mathbf{y} \in \mathbb{C}^{N_T^{Beam} N_R^{Beam} \times 1}$ and sensing matrix $\mathbf{Q} \in \mathbb{C}^{N_T^{Beam} N_R^{Beam} \times N_T N_R}$.

Output: $\hat{\mathbf{H}}$.

- 1: **Initialization:** $\hat{\mathbf{h}}(0) = \mathbf{0}_{G^2 \times 1}$.
 - 2: **for** $n = 1, 2, \dots$ **Do**.
 - 3: $\mathbf{e}(k) = \mathbf{y}(k) - \mathbf{Q}^H(k)\hat{\mathbf{h}}(k)$.
 - 4: Update $\hat{\mathbf{h}}(k+1)$ using (2.23).
 - 5: **End For**
 - 6: $\hat{\mathbf{H}} = \mathbf{A}_R(\Theta_R)\text{vec}^{-1}(\hat{\mathbf{h}})\mathbf{A}_T^H(\Phi_T)$
-

ZALMS using l_0 -norm approximation

The l_0 norm penalty function, denoted by $f_0(\cdot)$, is defined as:

$$f_0(\hat{\mathbf{h}}(k)) = \|\hat{\mathbf{h}}(k)\|_0 = \sum_{k=1}^{G^2} \mathcal{I}(|\hat{\mathbf{h}}(k)| > 0), \quad (2.24)$$

where $\mathcal{I}(\cdot)$ denotes the indicator function. Now employ a suitable approximation, as in [102], $\sum_{k=1}^{G^2} \mathcal{I}(|\hat{\mathbf{h}}(k)| > 0) \approx \sum_{k=1}^{G^2} (1 - e^{-\nu(|\hat{\mathbf{h}}(k)|)})$, where ν is the accuracy of

the approximation parameter. Thus, the gradient term $g(f_0(\hat{\mathbf{h}}(k)))$ is given as:

$$g(f_0(\hat{\mathbf{h}}(k))) = \nu e^{-\nu(|\hat{\mathbf{h}}(k)|)} \times \text{sgn}(\hat{\mathbf{h}}(k)). \quad (2.25)$$

Substituting the value of $g(f_0(\hat{\mathbf{h}}(k)))$ from (2.25) into (2.23), the update equation for ZALMS- l_0 , is obtained as:

$$\hat{\mathbf{h}}(k+1) = \hat{\mathbf{h}}(k) + \mu \mathbf{Q}^H(k) \mathbf{e}(k) - \rho_0 \nu e^{-\nu(|\hat{\mathbf{h}}(k)|)} \times \text{sgn}(\hat{\mathbf{h}}(k)), \quad (2.26)$$

where ρ_0 is regularization parameter for ZALMS- l_0 .

ZALMS using l_1 -norm approximation

The l_1 -norm penalty function is represented as $f_1(\cdot)$, is defined as [102]

$$f_1(\hat{\mathbf{h}}(k)) = \|\hat{\mathbf{h}}(k)\|_1 = \sum_{k=1}^{G^2} |\hat{\mathbf{h}}(k)|. \quad (2.27)$$

The gradient term $g(f_1(\hat{\mathbf{h}}(k)))$ is computed as follows:

$$g(f_1(\hat{\mathbf{h}}(k))) = \text{sgn}(\hat{\mathbf{h}}(k)). \quad (2.28)$$

The update equation for ZALMS- l_1 -norm is given as:

$$\hat{\mathbf{h}}(k+1) = \hat{\mathbf{h}}(k) + \mu \mathbf{Q}^H(k) \mathbf{e}(k) - \rho_1 \text{sgn}(\hat{\mathbf{h}}(k)). \quad (2.29)$$

Upon adaptation as per (2.29), the tap coefficients are attracted to zero by the third term present in (2.26) and (2.29), known as zero attractor. The strength of zero attractor depends on regularization step size ρ . The speed of convergence increases when the $\hat{\mathbf{h}}(k)$ is sparse, i.e., the majority of coefficients are zero.

2.3 Parameter Analysis

In this section, an expression is derived for mean weight error vector and excess mean square error (EMSE) for ZALMS- l_1 norm approximation. We prove that

steady state MSE floor for ZALMS- l_1 approximation is lower as compared to LMS.

2.3.1 Mean Behavior Analysis

We define the weight error vector $\tilde{\mathbf{h}}(k)$ as follows:

$$\tilde{\mathbf{h}}(k) = \mathbf{h}_b^{\text{opt}} - \hat{\mathbf{h}}(k), \quad (2.30)$$

where $\mathbf{h}_b^{\text{opt}}$ is weight of optimal filter. Subtracting $\mathbf{h}_b^{\text{opt}}$ both side from (2.23) and upon expectation, the update equation for weight error vector $\tilde{\mathbf{h}}(k)$ of ZALMS is given by:

$$\begin{aligned} \mathbb{E}\{\tilde{\mathbf{h}}(k+1)\} &= \mathbb{E}\{\tilde{\mathbf{h}}(k)\} - \mu \mathbb{E}\{\mathbf{Q}^H(k)\mathbf{Q}(k)\tilde{\mathbf{h}}(k)\} \\ &\quad + \mu \mathbb{E}\{\mathbf{Q}^H(k)\mathbf{n}(k)\} - \rho \mathbb{E}\{g(f(\hat{\mathbf{h}}(k)))\}, \end{aligned} \quad (2.31)$$

Assuming the independence of sensing matrix $\mathbf{Q}(k)$, $\mathbf{n}(k)$, and $\tilde{\mathbf{h}}(k)$, $\mathbb{E}\{\mathbf{Q}^H(k)\mathbf{n}(k)\}$ will be zero, and $\mathbb{E}\{\mathbf{Q}^H(k)\mathbf{Q}(k)\tilde{\mathbf{h}}(k)\} = \mathbf{R}\mathbb{E}\{\tilde{\mathbf{h}}(k)\}$. Combining these, the resultant equation is expressed as:

$$\mathbb{E}\{\tilde{\mathbf{h}}(k+1)\} = (\mathbf{I} - \mu\mathbf{R})\mathbb{E}\{\tilde{\mathbf{h}}(k)\} - \rho \mathbb{E}\{g(f(\hat{\mathbf{h}}(k)))\}. \quad (2.32)$$

For l_1 norm approximation the gradient of penalty induced function $g(f(\hat{\mathbf{h}}(k))) = \rho \mathbb{E}\{\text{sgn}(\hat{\mathbf{h}}(k))\}$ that is bounded between $-\rho\mathbf{1}$ and $\rho\mathbf{1}$, where $\mathbf{1}$ is vector of 1's. Thus, $\mathbb{E}\{\tilde{\mathbf{h}}(k+1)\}$ is guaranteed to converge if the maximal eigenvalue of $(\mathbf{I} - \mu\mathbf{R})$ is less than 1. From (2.32), it is concluded that $\mathbb{E}\{\tilde{\mathbf{h}}(k)\}$ converges under the condition $0 < \mu < \frac{2}{\lambda_{max}}$. Where λ_{max} is maximum eigenvalue of \mathbf{R} . After simplification, mean coefficient vector for ZALMS- l_1 in (2.32) is rewritten as:

$$\lim_{n \rightarrow \infty} \mathbb{E}\{\hat{\mathbf{h}}(k)\} = \mathbf{h}_b^{\text{opt}} - \frac{\rho}{\mu} \mathbf{R}^{-1} \mathbb{E}\{\text{sgn}(\mathbf{h}_b^{\text{opt}})\}. \quad (2.33)$$

Therefore, it is proved that for a sparse channel and for a proper value of ρ , the ZALMS attains lower MSE than classical LMS.

2.3.2 Excess MSE Analysis

In this section, excess MSE for ZALMS- l_1 and difference of EMSE of ZALMS- l_1 and classical LMS is derived.

Excess MSE of ZALMS- l_1 norm

From (2.30), the weight error vector $\tilde{\mathbf{h}}(k) = \mathbf{h}_b^{\text{opt}} - \hat{\mathbf{h}}(k)$, and the update equation is expressed as:

$$\tilde{\mathbf{h}}(k+1) = \tilde{\mathbf{h}}(k) - \mu \mathbf{Q}^H(k) \mathbf{e}(k) + \rho \text{sgn}(\tilde{\mathbf{h}}(k) + \mathbf{h}_b^{\text{opt}}). \quad (2.34)$$

Multiplying both sides by $\mathbf{Q}(k)$ and by the definition of a priori estimation error $\mathbf{e}_a(k) = \mathbf{Q}(k) \tilde{\mathbf{h}}(k)$ and a posteriori $\mathbf{e}_p(k) = \mathbf{Q}(k) \tilde{\mathbf{h}}(k+1)$ estimation error,

$$\mathbf{e}_p(k) = \mathbf{e}_a(k) - \mu \|\mathbf{Q}(k)\|^2 \mathbf{e}(k) + \rho \mathbf{Q}(k) \text{sgn}(\tilde{\mathbf{h}}(k) + \mathbf{h}_b^{\text{opt}}). \quad (2.35)$$

Output estimation error $\mathbf{e}(k)$ is written as:

$$\mathbf{e}(k) = \frac{1}{\mu \|\mathbf{Q}(k)\|^2} \{ \mathbf{e}_a(k) - \mathbf{e}_p(k) + \rho \mathbf{Q}(k) \text{sgn}(\tilde{\mathbf{h}}(k) + \mathbf{h}_b^{\text{opt}}) \}. \quad (2.36)$$

Substituting the value of $\mathbf{e}(k)$ from (2.36) to (2.34), weight error update equation can be written as $\tilde{\mathbf{h}}(k+1) = \tilde{\mathbf{h}}(k) - \frac{\mathbf{Q}^H(k)}{\|\mathbf{Q}(k)\|^2} \{ \mathbf{e}_a(k) - \mathbf{e}_p(k) + \rho \mathbf{Q}(k) \text{sgn}(\tilde{\mathbf{h}}(k) + \mathbf{h}_b^{\text{opt}}) \} + \rho \text{sgn}(\tilde{\mathbf{h}}(k) + \mathbf{h}_b^{\text{opt}})$. After simplification, squaring, and taking expectation weight error update expression expression is given by:

$$\begin{aligned} \mathbb{E}\{\|\tilde{\mathbf{h}}(k+1)\|^2\} + \mathbb{E}\left\{\frac{|\mathbf{e}_a(k)|^2}{\|\mathbf{Q}(k)\|^2}\right\} &= \mathbb{E}\left\{\|\tilde{\mathbf{h}}(k)\|^2\right\} \\ &+ \mathbb{E}\left\{\frac{|\mathbf{e}_p(k)|^2}{\|\mathbf{Q}(k)\|^2}\right\}. \end{aligned} \quad (2.37)$$

Equation (2.37) is commonly known as the energy conservation relation. At steady state, $\mathbb{E}\{\|\tilde{\mathbf{h}}(k)\|^2\} = \mathbb{E}\{\|\hat{\mathbf{h}}(k)\|^2\}$, which leads us to conclude:

$$\mathbb{E}\left\{\frac{|\mathbf{e}_a(k)|^2}{\|\mathbf{Q}(k)\|^2}\right\} = \mathbb{E}\left\{\frac{|\mathbf{e}_p(k)|^2}{\|\mathbf{Q}(k)\|^2}\right\}. \quad (2.38)$$

Upon substituting $\mathbf{e}_p(k)$ from (2.35) to (2.38),

$$\mathbb{E} \left\{ \frac{1}{\|\mathbf{Q}(k)\|^2} |\mathbf{e}_a(k)|^2 \right\} = \mathbb{E} \left\{ \frac{1}{\|\mathbf{Q}(k)\|^2} |\mathbf{e}_a(k) - \mu \|\mathbf{Q}(k)\|^2 \mathbf{e}(k) + \rho \mathbf{Q}(k) \text{sgn}(\tilde{\mathbf{h}}(k) + \mathbf{h}_b^{\text{opt}})|^2 \right\}. \quad (2.39)$$

Expanding RHS of (2.39), and applying the relation $\mathbf{e}(k) = \mathbf{e}_a(k) + \mathbf{n}(k)$. After simplifying (2.39), the EMSE for ZALMS is given by:

$$J_{zaex}(\infty) = \frac{\kappa}{2 - \kappa} \sigma_n^2 + \frac{\iota_1}{(2 - \kappa)\mu} \rho \left(\rho - \frac{2\iota_2}{\iota_1} \right), \quad (2.40)$$

where $\kappa = \text{tr}(\mathbf{R}(\mathbf{I} - \mu\mathbf{R})^{-1})$, σ_n^2 is variance of observation noise, $\iota_1 = \mathbb{E}\{\text{sgn}(\hat{\mathbf{h}}(\infty))^T (\mathbf{I} - \mu\mathbf{R})^{-1} \text{sgn}(\hat{\mathbf{h}}(\infty))\}$, and $\iota_2 = \mathbb{E}\{\|\hat{\mathbf{h}}(\infty)\|_1\} - \|\mathbf{h}_b^{\text{opt}}\|_1$.

Difference of Excess MSE of ZALMS- ι_1 and standard LMS

As the first term on the RHS of (2.40) is the steady state excess MSE of the standard LMS filter. Therefore, (2.40) is rewritten as:

$$J_{zaex}(\infty) = J_{lmex}(\infty) + \frac{\iota_1}{(2 - \kappa)\mu} \rho \left(\rho - \frac{2\iota_2}{\iota_1} \right). \quad (2.41)$$

Therefore, $J_{zaex}(\infty) - J_{lmex}(\infty)$ can be given by $\frac{\iota_1}{(2 - \kappa)\mu} \rho \left(\rho - \frac{2\iota_2}{\iota_1} \right)$ which under small misadjustment condition $\mu \ll \frac{2}{\text{Tr}(\mathbf{R})}$ can be reduces to $\frac{\rho}{2\mu} (\rho\iota_1 - 2\iota_2)$. Assuming i.i.d input with $\mu \ll 1/\sigma_Q^2$ we have $\mathbf{I} - \mu\mathbf{R} = (1 - \mu\sigma_Q^2)\mathbf{I} \approx \mathbf{I}$, Since, $\text{sgn}(\hat{\mathbf{h}}(\infty))^T \text{sgn}(\hat{\mathbf{h}}(\infty)) = T$, where T is the number of active taps. In such case $\iota_1 = T$, ι_2 can be equivalently expressed as, $\iota_2 = \sum_{i=0}^{T-1} \mathbb{E}\{|\hat{h}_{b,i}(\infty)|\} - |h_{b,i}^{\text{opt}}|$. Now if $\hat{\mathbf{h}}(\infty)$ is Gaussian, then by the definition of folded normal distribution from [103]:

$$\mathbb{E}\{|\hat{h}_{b,i}(\infty)|\} = h_{b,i}^{\text{opt}} \left[1 - 2\text{erf} \left(-\frac{h_{b,i}^{\text{opt}}}{\sigma_{\hat{h}_{b,i}}} \right) \right] + \sqrt{\frac{2}{\pi}} \sigma_{\hat{h}_{b,i}} \exp \left(-\frac{(h_{b,i}^{\text{opt}})^2}{2\sigma_{\hat{h}_{b,i}}^2} \right), \quad (2.42)$$

after simplification of (2.42) we can find the value of ι_2 as $\iota_2 = \sqrt{\frac{2}{\pi}} \sum_{i \in Z} \sigma_{\hat{h}_{b,i}}$. Now putting the value of ι_1 and ι_2 in $\frac{\rho}{2\mu} (\rho\iota_1 - 2\iota_2)$, the difference of excess MSE of

ZALMS- l_1 norm and LMS is given by:

$$J_{zaex}(\infty) - J_{lmax}(\infty) = \frac{\rho}{2\mu} \left(\rho T - 2\sqrt{\frac{2}{\pi}} \sum_{i \in Z} \sigma_{\hat{h}_{b,i}} \right). \quad (2.43)$$

As value of $2\sqrt{\frac{2}{\pi}} \sum_{i \in Z} \sigma_{\hat{h}_{b,i}}$ is larger than the product ρT for sparse channel, so the overall value will be negative, means $J_{zaex}(\infty)$, excess MSE of ZALMS is less than $J_{lmax}(\infty)$, excess MSE of LMS. For a sparse channel, (2.43) guarantees a lower MSE floor of ZALMS compared with LMS.

2.4 Simulation Results

The simulations presented in this work are divided into two sections. In the first section, we illustrate the estimation accuracy of the considered mmWave MIMO system using the MSE as a performance metric. In the second section, we demonstrate the SE for the same system corresponding to the different channel estimators. For these simulations, we considered one BS and one MS i.e., without any interference with the number of transmitting and receiving antenna is 32, the number of RF chain is 8 for both the transmitter and receiver, antenna arrays are uniform linear array (ULA) with antenna spacing is $\lambda/2$ and RF phase shifters are assumed in precoders. The channel considered here is a geometric channel described in (2.1), with the number of paths is 3. The AoDs/AoAs are taken 32 quantized values in the range $[0 \ 2\pi]$, the amplitude of path gain is Rayleigh distributed. For channel estimation, the consider the step size (μ) = .05, regularization parameter (ρ_0) for ZALMS- l_0 is 5×10^{-6} , regularization parameter (ρ_1) for ZALMS- l_1 is 5×10^{-5} , accuracy parameter (ν) for ZALMS- l_0 is 20 [98]. SNR for estimation is fixed 30 dB for all the illustrated cases, and the SNR range for spectral efficiency calculation is from -40dB to 0dB [43]. All the simulations are ensembled by 1000 Monte Carlo simulations.

From Figure 2.2, it is observed that sparse aware channel estimation algorithms, as the ZALMS- l_1 , and ZALMS- l_0 deliver improved performance as compared to the LMS for the mmWave MIMO system. MSE floor of ZALMS- l_0 based estimator is quite close to optimal (Wiener) estimator and that of output error corresponding to

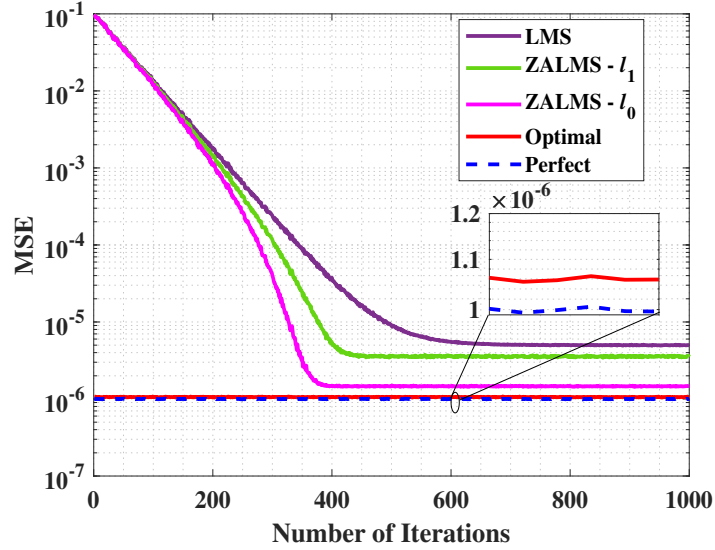


Figure 2.2: MSE performance of LMS, ZALMS- l_1 , and ZALMS- l_0 with optimal and true channel. Simulation parameter are $N_T = 32$, $N_R = 32$, $\mu = .05$, $\rho_1 = 5 \times 10^{-5}$, $\rho_0 = 5 \times 10^{-6}$, $\nu = 20$.

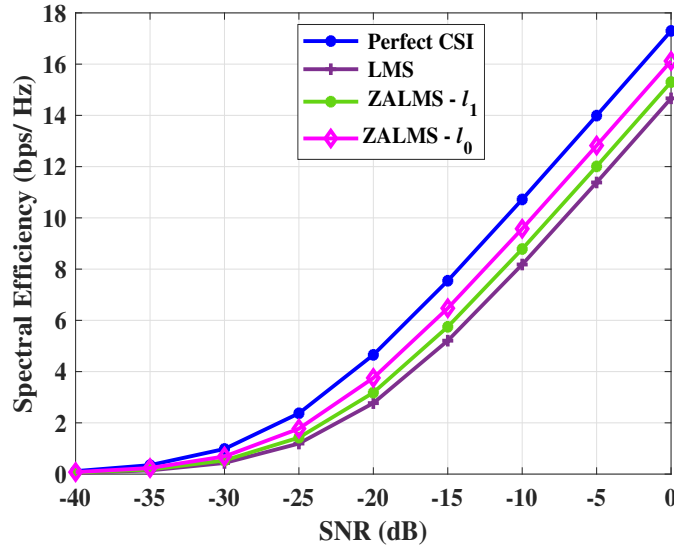


Figure 2.3: Comparison of spectral efficiency with estimated CSI from different estimator to the perfect CSI for the mmWave MIMO system, with $N_T = 32$, $N_R = 32$, $N_{RF} = 8$, $L = 2$, and pathloss component 3.

the true channel, that is drawn for benchmarking purpose. ZALMS- l_0 norm-based estimator has approximately 1 dB lower steady state MSE as compared to classical LMS and 0.52 dB lower steady state MSE as compared to ZALMS- l_1 based estimator and converges approximately 20 iterations before from ZALMS- l_1 and 100 iterations before than classical LMS. Thus ZALMS- l_0 based estimator outperform in terms of both accuracy and convergence rate as compared to ZALMS- l_1 and classical LMS.

The spectral efficiency for different channel estimation approaches are compared in Figure 2.3 for various SNR values. From the figure, a general trend of increase in SE is observed with an increase in estimation accuracy. In particular, it is observed for the ZALMS- l_0 based estimator, the SE is approximately 1.5 bps/Hz more compared to LMS based estimator and 0.8 bps/Hz more than ZALMS- l_1 based estimator. This leads us to conclude that the proposed ZALMS based channel estimator improves the overall system performance.

2.5 Summary

In this chapter, ZALMS based sparse channel estimation is proposed for narrowband mmWave hybrid MIMO system and its MSE is analyzed and validated through simulations over mmWave MIMO systems. The presented simulation results indicate that ZALMS- l_0 outperforms ZALMS- l_1 and classical LMS in terms of accuracy (has lower MSE floor) and convergence (require less number of iterations). Comparisons are presented for the spectral efficiency of different channel estimation methods and the enhanced estimation accuracy of the ZALMS- l_0 is observed from the presented simulations, which motivates the proposed ZALMS as a promising channel estimation method for mmWave MIMO.

Further, in practice, transceivers suffer from HIs that affect their performance and should be considered for a fair analysis. In the next chapter we will consider mmWave hybrid MIMO system with HI.

Chapter 3

SI-ZALMS based Channel Estimator for mmWave Hybrid MIMO System with HI

In the previous chapter, channel estimation of a mmWave hybrid MIMO system was performed for ideal hardware. However, the impact of hardware impairments (HIs) was not considered. In this chapter, we address the impact of HIs, which must be considered in practical system design.

MmWave hybrid MIMO is a pioneering physical layer technique for the fifth generation and beyond fifth-generation (5G/B5G) wireless communication systems, to provide ultra-high data rate, massive connectivity, and ultra-low latency [91]. For such MIMO systems, channel estimation is of fundamental importance for their analysis and design [91, 104, 105]. The mmWave hybrid MIMO systems rely on a wide bandwidth (up to 2 GHz) in the frequency range of 30 GHz to 300 GHz [90]. The mmWave MIMO systems are known to empower advanced applications such as high definition wireless local area networks (WLAN), smart wearables, virtual reality (VR), augmented reality (AR), and most prominently 5G new-radio (5G-NR) [89, 99, 106]. Despite the aforementioned advantages and applications, mmWave offers several technological challenges such as high path loss, severe propagation loss, and high energy consumption in the circuits.

The typically small wavelength of mmWave allows for mounting several antennas per unit area which, in turn allows for the premise of massive MIMO. This

consideration of mmWave with MIMO allows for formation of a high gain beam to mitigate the propagation loss [107, 108]. However, the deployment of several antennas is challenging due to the associated hardware complexity due to the very high sampling rate of DAC/ADC converters which involve high power consumption the RF chains connected to each transmitter and receiver. To overcome this high power consumption a hybrid architecture was proposed in [13, 99], and [43].

Unlike conventional MIMO systems where the majority of signal processing is done in the baseband, hybrid mmWave MIMO architecture divides the overall signal processing in baseband and RF domain. For hybrid mmWave MIMO architectures, the analog beamforming involves a digitally controlled phase shifter network to achieve beamforming gain [19]. For such systems, accurate CSI is necessary for designing of the precoding/combining matrices for mmWave hybrid MIMO system, which is challenging due to large number of antenna elements.

Recent works for channel estimation of mmWave hybrid MIMO system as [43, 92, 93, 96, 99, 109–117], mostly consider ideal hardware and research works like [114] where, a deep learning aided channel estimation algorithm is proposed which is different from most existing works concerning the compressed sensing (CS)-based channel estimation. In [114], off-grid channel estimation problem is solved by using a low computational complexity alternating direction method of multipliers (ADMM)-based algorithm, dubbed ADMM-OG algorithm. In [115], quaternion theory based algorithm named quaternion non-circular MUSIC (QNC-MUSIC) is proposed for parameter estimation of non-circular signals with high estimation accuracy for large-scale/massive MIMO systems. In [115], it is shown that the QNC-MUSIC has much lower computational complexity as compared to the conventional methods. However, both [114] and [115], assume an ideal transceiver hardware. In [118], an efficient channel estimation method for frequency selective channels is proposed which is based on the training channel model for urban traffic scenario. In this work, author has raised issue of noise correlation in practical channel, and proposed noise weighted method to solve the sparse signal recovery problem. However, the impact of transceiver hardware impairments is not considered. To achieve high reliability and spectral efficiency for industrial big data, a multiple-input–multiple-output filter bank multicarrier (MIMO-FBMC) communication system is employed under

offset quadrature amplitude modulation in [119]. In this article, a low-complexity sparse adaptive channel estimation scheme is proposed which is based on a dynamic threshold that reduces the number of inner product calculations.

However, for common cost effective and power efficient mmWave systems, generally inexpensive components are deployed which lead to hardware impairments. These low cost components (not limited to the aforementioned) make the non ideal hardware and introduce hardware impairments such as quantization error, I/Q imbalance, nonlinear power amplifier, and phase noise [85, 86, 120, 121]. To mitigate the effects of hardware impairments different compensation methods are studied [122–125]. Further, these distortions cannot be fully parameterized and estimated due to time varying statistics of the residual transceiver hardware impairments (RTHIs) [85]. Due to RTHIs training pilots and received signals get contaminated and consequently channel estimation performance degrades. In the literature, few studies consider the RTHI for the different systems [126]. As in [85], channel estimation with hardware impairments is considered for massive MIMO system, which is not specific for mmWave MIMO system.

In [126], the authors have considered hardware impairment for mmWave hybrid MIMO system and applied fast sparse Bayesian learning (FSBL) approach for channel estimation, which is more complex due to matrix inversion. Further, due to its offline nature, this method is unable to provide accurate estimate of channel gain due to distortion noise whose power is non-stationary due to its dependence on signal power and current channel gain. A major drawback in the existing methods is high computational complexity due to matrix inversion operations and increased processing delay due to their offline nature.

Against this background, we develop a novel sparse aware adaptive filtering approach for narrowband mmWave hybrid MIMO channel estimation considering residual hardware impairment to overcome the drawbacks of existing techniques. In this context, a zero attracting least mean square (ZALMS) [127] based online channel estimation techniques capable of accurate learning and tracking are inherently suitable for narrowband mmWave hybrid MIMO system. Moreover, these methods do not require apriori knowledge of second order statistics as an auto correlation matrix or cross covariance vectors, however they rely only on the instantaneous es-

timates of second order error statistics. Based on this background and literature survey, contributions of this work are summarized below.

- This work examines the *overall* impact of hardware impairments on mmWave hybrid MIMO systems as compared to the perfect hardware scenario considered in the literature (either in transmitter or receiver).
- The beamspace domain model of the mmWave MIMO channel is used for sparse channel estimation using a sparse dictionary consisting of the quantized receive and transmit array response vectors.
- For adaptive online channel estimation in narrowband mmWave hybrid MIMO systems, a ZALMS-based channel estimator is proposed, which reduces the estimation error variance. Since the proposed ZALMS technique depends on the first and second order statistics of the narrowband mmWave MIMO channel, it is well suited to both stationary and non-stationary channels, emphasizing its practical significance. Furthermore, to enhance the convergence rate of ZALMS, SI-ZALMS is proposed.
- Detailed analysis and expressions for MSE, MSD, range of regularization, and step size parameter are derived and validated via computer simulations.
- The proposed SI-ZALMS and ZALMS-based approaches are compared against existing methods and an analytical bound is derived to quantify its performance.

3.1 System Model

3.1.1 Hardware Impairments

A generalized system model that represents the impact of residual transceiver impairments is given in Figure 3.1, where \mathbf{e}_t and \mathbf{e}_r denote the additive distortion noise due to residual impairments at the transmitter and the receiver. From the existing works [85], it is known that $\mathbf{e}_t \sim \mathcal{CN}(\mathbf{0}_{N_T}, \mathbf{\Upsilon}_t)$ and $\mathbf{e}_r \sim \mathcal{CN}(\mathbf{0}_{N_R}, \mathbf{\Upsilon}_r)$ follows a Gaussian distribution with its average power proportional to the average signal

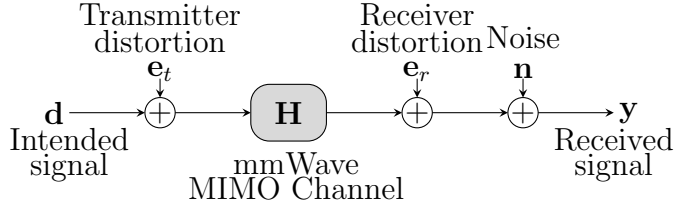


Figure 3.1: Generalized transmission with hardware impairments.

power at each antenna where $\Upsilon_{\mathbf{t}} = \kappa_t \text{diag}(r_{1,1}, r_{2,2}, \dots, r_{N_T, N_T})$, $\Upsilon_{\mathbf{r}} = \kappa_r \mathbf{H}^H \text{tr}\{\mathbf{R}\} \mathbf{H}$, $\kappa_t, \kappa_r \geq 0$ are proportionality coefficients, and $(r_{1,1}, r_{2,2}, \dots, r_{N_T, N_T})$ are the diagonal elements of signal covariance matrix \mathbf{R} . The proportionality coefficient κ_t and κ_r are related to the error vector magnitude (EVM) and characterize the level of hardware impairments. The EVM at transmitter is given by [85]:

$$\text{EVM}_t = \sqrt{\frac{\mathbb{E}\{\|\mathbf{e}_t\|_2^2\}}{\mathbb{E}\{\|\mathbf{x}\|_2^2\}}} = \sqrt{\frac{\kappa_t \text{tr}\{\mathbf{R}\}}{\text{tr}\{\mathbf{R}\}}} = \sqrt{\kappa_t}. \quad (3.1)$$

For practical application such as Long Term Evolution (LTE), the EVM has a range of [0.08, 0.175] [87].

Transceiver signal in practical mmWave hybrid MIMO system is shown in Figure 3.2, which experience distortion due to imperfect behavior of hardware components such as, mixer, oscillator, filter, converter, and amplifier. Many compensation techniques can be applied at the transceiver to mitigate the impairment, even after some residual impairments remain. Total residual impairments at the transceiver are modeled as independent additive distortion noise as done in [85] and [86]. *The distortion noise is well known to be non-stationary because it is proportional to the instantaneous signal power P and the current channel gain $\|\mathbf{H}\|_2^2$. As adaptive method has inherent tracking capability so it is well suited for channel estimation of mmWave hybrid MIMO system with non-ideal hardware.*

The mmWave hybrid MIMO system with considered transceiver hardware impairments can be accurately modeled as,

$$\mathbf{y} = \mathbf{W}^H \mathbf{H}(\mathbf{x} + \mathbf{e}_t) + \mathbf{W}^H \mathbf{e}_r + \mathbf{W}^H \mathbf{n}. \quad (3.2)$$

Since low-cost hardware is used in practical deployed mmWave systems MIMO,

which leads to large EVM, which, in turn limits the system performance [85]. In this work, channel estimation in the downlink problem is considered with single BS and MS, that is equipped with uniform linear array (ULA) of N_T and N_R transmitting and receiving antennas, respectively. N_{RF} is number of RF chains at the transmitting and the receiving side, such that $N_{RF} \ll \min(N_T, N_R)$ [43]. Transmitter first modifies the input data vector $\mathbf{d} \in \mathbb{C}^{N_{RF} \times 1}$ with a baseband precoder $\mathbf{F}_{BB} \in \mathbb{C}^{N_{RF} \times N_{RF}}$, and then the RF precoder $\mathbf{F}_{RF} \in \mathbb{C}^{N_T \times N_{RF}}$ before transmission. The transmitted signal is represented as

$$\mathbf{x} = \mathbf{F}_{RF} \mathbf{F}_{BB} \mathbf{d} = \mathbf{F} \mathbf{d}, \quad (3.3)$$

where $\mathbf{x} \in \mathbb{C}^{N_T \times 1}$ is a pilot signal with covariance matrix $\mathbb{E}\{\mathbf{x}\mathbf{x}^H\} = \mathbf{Q}$ and $\mathbf{F} = \mathbf{F}_{RF} \mathbf{F}_{BB}$ denoting the combined precoding matrix. We consider a quasi-static narrowband channel model, corresponding to the pre-processed received signal \mathbf{r} can be given as,

$$\mathbf{r} = \mathbf{H} \mathbf{x} + \mathbf{n}, \quad (3.4)$$

where \mathbf{n} is the observed additive white Gaussian noise (AWGN) with distribution $\mathcal{CN}(\mathbf{0}, \sigma_n^2 \mathbf{I}_{N_R})$ and $\mathbf{H} \in \mathbb{C}^{N_R \times N_T}$ is MIMO channel matrix.

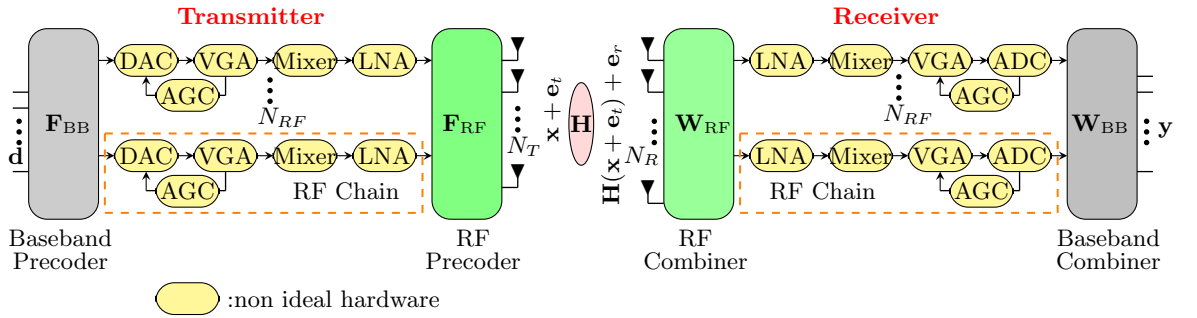


Figure 3.2: Millimeter wave hybrid MIMO transceiver block diagram with non-ideal hardware.

To process the received signal, receiver comprises of a hybrid combiner \mathbf{W} , that is cascaded with RF combiner $\mathbf{W}_{RF} \in \mathbb{C}^{N_R \times N_{RF}}$ and baseband combiner $\mathbf{W}_{BB} \in \mathbb{C}^{N_{RF} \times N_{RF}}$. Finally, the post processed signal is given as,

$$\mathbf{y} = \mathbf{W}^H \mathbf{H} \mathbf{x} + \mathbf{n}. \quad (3.5)$$

3.1.2 MmWave Channel Model

We consider a dense urban non-line-of-sight scenario for which geometric narrow-band channel with L scatterers is taken into consideration, with each scatterer contributing a single propagation path between the BS and the MS. Under this model, the channel \mathbf{H} can be represented as [43],

$$\mathbf{H} = \sqrt{\frac{N_T N_R}{\eta}} \sum_{l=1}^L \alpha_l \mathbf{a}_R(\theta_l) \mathbf{a}_T^H(\phi_l), \quad (3.6)$$

where η denotes the average path loss between BS and MS, α_l is the complex path gain of the l^{th} path and its amplitude is assumed to be Rayleigh distributed. The azimuth AoA and AoD are represented by the variables $\theta_l \in [0, 2\pi]$ and $\phi_l \in [0, 2\pi]$, respectively. $\mathbf{a}_T(\phi_l)$ and $\mathbf{a}_R(\theta_l)$ are the transmitter and receiver antenna array response vector, that can be expressed as,

$$\mathbf{a}_T(\phi_l) = \frac{1}{\sqrt{N_T}} [1, e^{-j2\pi(s/\lambda)\cos(\phi_l)}, \dots, e^{-j(N_T-1)2\pi(s/\lambda)\cos(\phi_l)}], \quad (3.7)$$

and

$$\mathbf{a}_R(\theta_l) = \frac{1}{\sqrt{N_R}} [1, e^{-j2\pi(s/\lambda)\cos(\theta_l)}, \dots, e^{-j(N_R-1)2\pi(s/\lambda)\cos(\theta_l)}], \quad (3.8)$$

respectively, where s is spacing between the neighboring antenna and λ is the signal wavelength.

In beamspace domain the channel (3.6) can be represented as,

$$\mathbf{H} = \mathbf{A}_R \mathbf{H}_a \mathbf{A}_T^H, \quad (3.9)$$

where \mathbf{A}_T and \mathbf{A}_R are the transmit and receive array response dictionary matrices and \mathbf{H}_a is sparse beamspace channel matrix that are given as,

$$\mathbf{H}_a = \text{diag}\left(\sqrt{\frac{N_T N_R}{\eta}} [\alpha_1, \alpha_2, \dots, \alpha_L]^T\right). \quad (3.10)$$

$$\mathbf{A}_T = [\mathbf{a}_T(\phi_1), \mathbf{a}_T(\phi_2), \dots, \mathbf{a}_T(\phi_L)]. \quad (3.11)$$

and

$$\mathbf{A}_R = [\mathbf{a}_R(\theta_1), \mathbf{a}_R(\theta_2), \dots, \mathbf{a}_R(\theta_L)]. \quad (3.12)$$

3.1.3 Sparse Formulation of MmWave Hybrid MIMO Channel

AoA and AoD are partitioned into $G \geq \max\{N_T, N_R\}$ points in the interval $[0, \pi)$ at the transmitter and receiver. Let angle of departure grid Φ_T and angle of arrival grid Θ_R are uniformly spaced and defined as,

$$\Phi_T = \left\{ \phi_g : \phi_g = \frac{\pi(g-1)}{G}, \forall 1 \leq g \leq G \right\}. \quad (3.13)$$

$$\Theta_R = \left\{ \theta_g : \theta_g = \frac{\pi(g-1)}{G}, \forall 1 \leq g \leq G \right\}. \quad (3.14)$$

Assume further $\mathbf{A}_T(\Phi_T) \in \mathbb{C}^{N_T \times G}$ and $\mathbf{A}_R(\Theta_R) \in \mathbb{C}^{N_R \times G}$ represent transmit and receive array response dictionary (ARD) matrices given as

$$\mathbf{A}_R(\Theta_R) = [\mathbf{a}_R(\theta_1), \mathbf{a}_R(\theta_2), \dots, \mathbf{a}_R(\theta_G)], \quad (3.15)$$

and

$$\mathbf{A}_T(\Phi_T) = [\mathbf{a}_T(\phi_1), \mathbf{a}_T(\phi_2), \dots, \mathbf{a}_T(\phi_G)]. \quad (3.16)$$

The transmitter and receiver ARD matrices meet the condition $\mathbf{A}_T(\Phi_T)\mathbf{A}_T^H(\Phi_T) = \frac{G}{N_T}\mathbf{I}_{N_T}$ and $\mathbf{A}_R(\Theta_R)\mathbf{A}_R^H(\Theta_R) = \frac{G}{N_R}\mathbf{I}_{N_R}$ [99].

In the beamspace domain, representation of the channel matrix \mathbf{H}_s can be obtained in terms of ARD matrices as,

$$\mathbf{H}_s = \mathbf{A}_R(\Theta_R)\mathbf{H}_b\mathbf{A}_T^H(\Phi_T), \quad (3.17)$$

where $\mathbf{H}_b \in \mathbb{C}^{G \times G}$ is sparse beamspace channel matrix.

3.1.4 Hybrid Processing Model with Hardware Impairments

In this section, to model mmWave channel estimation with transceiver hardware impairments, the sparse recovery problem with measurement matrix perturbation is used. For a coherent channel block B ($K \ll B$), K symbols are assumed allocated for channel estimation, and $\mathbf{W}^{(k)}$ and $\mathbf{x}^{(k)}$ are the combining matrix and training pilot sequence for the k -th training time instant, where $1 \leq k \leq K$. Exploiting the inherent channel-sparsity, the combined signal is reconstructed as follows at the k -th training time instant:

$$\begin{aligned} \mathbf{y}^{(k)} &= \left((\mathbf{x}^{(k)} + \mathbf{e}_t^{(k)})^T \otimes (\mathbf{W}^{(k)})^H \right) \text{vec}(\mathbf{H}_b) + \tilde{\mathbf{n}}^{(k)}, \\ &= \left((\mathbf{x}^{(k)} + \mathbf{e}_t^{(k)})^T \otimes (\mathbf{W}^{(k)})^H \right) \mathbf{Z} \mathbf{h}_b + \tilde{\mathbf{n}}^{(k)}, \end{aligned} \quad (3.18)$$

where

$$\tilde{\mathbf{n}}^{(k)} = (\mathbf{W}^{(k)})^H \mathbf{e}_r^{(k)} + (\mathbf{W}^{(k)})^H \mathbf{n}^{(k)},$$

$\mathbf{Z} = (\mathbf{A}_T(\Phi_T))^* \otimes \mathbf{A}_R(\Theta_R)$, and $\mathbf{h}_b = \text{vec}(\mathbf{H}_b) \in \mathbb{C}^{G^2 \times 1}$ is an L -sparse vector. For all K - observations by stacking them,

$$\underbrace{\begin{bmatrix} \mathbf{y}^{(1)} \\ \vdots \\ \mathbf{y}^{(K)} \end{bmatrix}}_{\mathbf{y}} = \underbrace{\begin{bmatrix} (\mathbf{x}^{(1)} + \mathbf{e}_t^{(1)})^T \otimes (\mathbf{W}^{(1)})^H \\ \vdots \\ (\mathbf{x}^{(K)} + \mathbf{e}_t^{(K)})^T \otimes (\mathbf{W}^{(K)})^H \end{bmatrix}}_{\mathbf{Q}} \mathbf{Z} \mathbf{h}_b + \underbrace{\begin{bmatrix} \tilde{\mathbf{n}}^{(1)} \\ \vdots \\ \tilde{\mathbf{n}}^{(K)} \end{bmatrix}}_{\tilde{\mathbf{n}}}, \quad (3.19)$$

which can be simplified as:

$$\mathbf{y} = \mathbf{Q} \mathbf{h}_b + \tilde{\mathbf{n}}, \quad (3.20)$$

where \mathbf{y} , \mathbf{Q} , and $\tilde{\mathbf{n}}$ denote combined signal collection, measurement matrix, and equivalent noise collection, respectively. Graphical representation of received signal and unknown variables are given in Figure 3.3, where \mathbf{E} is distortion transmission noise matrix which is given as,

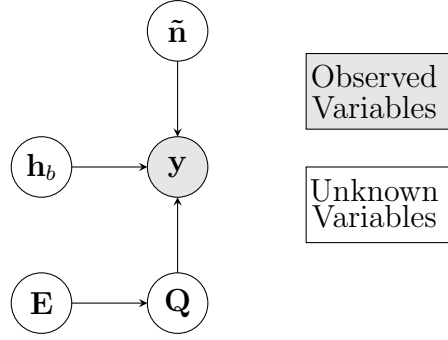


Figure 3.3: Graphical representation of received signal \mathbf{y} .

$$\mathbf{E} = [\mathbf{e}_t^{(1)}, \mathbf{e}_t^{(2)}, \dots, \mathbf{e}_t^{(K)}]. \quad (3.21)$$

An OMP-based approach [93] can be used to estimate the sparse channel vector \mathbf{h}_b . An distortion noise $\mathbf{e}_t^{(k)}$, on the other hand, introduces an unknown perturbation to the measurement matrix, separating the channel estimation problem from the traditional sparse recovery problem. In the next section, online adaptive filtering is proposed for LMS and ZALMS for mmWave MIMO channel estimation.

3.2 Adaptive Filtering Approach

3.2.1 LMS Algorithms for Channel Estimation

Let $\hat{\mathbf{h}}$ be the estimate of channel \mathbf{h}_b , then the mean square error cost function at k^{th} instant is given by,

$$J(k) = \mathbb{E}\{\|\mathbf{y}(k) - \mathbf{Q}^H(k)\hat{\mathbf{h}}(k)\|^2\}. \quad (3.22)$$

Using steepest descent algorithm [100], the estimate $\hat{\mathbf{h}}(k)$ is iteratively updated as:

$$\hat{\mathbf{h}}(k+1) = \hat{\mathbf{h}}(k) - \frac{\mu}{2} \nabla_{\hat{\mathbf{h}}(k)}(J(k)), \quad (3.23)$$

where μ is the step size parameter. By defining cross covariance vector

$$\mathbf{p} = \mathbb{E}\{\mathbf{Q}^H(k)\mathbf{y}(k)\} \in \mathbb{C}^{G^2 \times 1},$$

and auto-covariance matrix $\mathbf{R} = \mathbb{E}\{\mathbf{Q}^H(k)\mathbf{Q}(k)\} \in \mathbb{C}^{G^2 \times G^2}$, the gradient of the cost function $J(k)$ is given by:

$$\nabla_{\hat{\mathbf{h}}(k)}(J(k)) = 2\mathbf{R}\hat{\mathbf{h}}(k) - 2\mathbf{p}. \quad (3.24)$$

The weight update equation can be obtained by putting the value of $\nabla_{\hat{\mathbf{h}}(k)}(J(k))$ from (3.24) to (3.23),

$$\hat{\mathbf{h}}(k+1) = \hat{\mathbf{h}}(k) + \mu(\mathbf{p} - \mathbf{R}\hat{\mathbf{h}}(k)). \quad (3.25)$$

By using stochastic-gradient (SG) method that replaces \mathbf{R} and \mathbf{p} with their instantaneous estimates, $\hat{\mathbf{R}} = \mathbf{Q}^H(k)\mathbf{Q}(k)$ and $\hat{\mathbf{p}} = \mathbf{Q}^H(k)\mathbf{y}(k)$. By putting the values of $\hat{\mathbf{R}}$ and $\hat{\mathbf{p}}$ recursion is given as:

$$\hat{\mathbf{h}}(k+1) = \hat{\mathbf{h}}(k) + \mu\mathbf{Q}(k)\mathbf{e}(k), \quad (3.26)$$

where $\mathbf{e}(k) \in \mathbb{C}^{N_{RF} \times 1}$ is the instantaneous observation error can be expressed as,

$$\mathbf{e}(k) = \mathbf{y}(k) - \mathbf{Q}^H(k)\hat{\mathbf{h}}(k). \quad (3.27)$$

3.2.2 Proposed ZALMS algorithms

Assuming that \mathbf{h}_b is a sparse vector, estimation of the channel is defined as a non-convex combinatorial problem, which is written as follows:

$$\min_{\mathbf{h}_b} \|\mathbf{h}_b\|_0, \quad \text{s.t. } \|\mathbf{y} - \mathbf{Q}\mathbf{h}_b\|_2^2 \leq \varrho, \quad (3.28)$$

where $\varrho > 0$ is error tolerance. Various approaches e.g. OMP [93] and SBL [101], exist to solve the sparse signal recovery problem, but these algorithms offer high propagation delay and large computational complexity due to their offline nature and matrix inversions. The ZALMS algorithms which overcome these problems is developed next. The MSE cost function for ZALMS [102], at ith instant is given as

follows:

$$J_{ZA}(k) = \mathbb{E}\{\|\mathbf{y}(k) - \mathbf{Q}^H(k)\hat{\mathbf{h}}(k)\|^2\} + \gamma f(\hat{\mathbf{h}}(k)), \quad (3.29)$$

where $f(\cdot)$ is sparsity inducing penalty term and γ is regularization parameter. After employing steepest descent algorithm [100], the filter weight update equation can be expressed as follows:

$$\hat{\mathbf{h}}(k+1) = \hat{\mathbf{h}}(k) - \frac{\mu}{2} \nabla_{\hat{\mathbf{h}}(k)}(J_{ZA}(k)), \quad (3.30)$$

where the gradient is given as,

$$\nabla_{\hat{\mathbf{h}}(k)}(J_{ZA}(k)) = 2\mathbf{R}\hat{\mathbf{h}}(k) - 2\mathbf{p} - \rho g(f(\hat{\mathbf{h}}(k))), \quad (3.31)$$

where $g(f(\hat{\mathbf{h}}(k)))$ is the gradient of $f(\hat{\mathbf{h}}(k))$ and $\rho = \frac{\gamma\mu}{2}$ denotes regularization step-size. By putting the value of $\nabla_{\hat{\mathbf{h}}(k)}(J_{ZA}(k))$ from (3.31) to (3.30), simplified weight update is expressed as,

$$\hat{\mathbf{h}}(k+1) = \hat{\mathbf{h}}(k) + \mu(\mathbf{p} - \mathbf{R}\hat{\mathbf{h}}(k)) - \rho g(f(\hat{\mathbf{h}}(k))). \quad (3.32)$$

Applying SG algorithms, final update expression is given as,

$$\hat{\mathbf{h}}(k+1) = \hat{\mathbf{h}}(k) + \mu\mathbf{Q}(k)\mathbf{e}(k) - \rho g(f(\hat{\mathbf{h}}(k))), \quad (3.33)$$

where $\mathbf{e}(k)$ similar to (3.27), represents the instantaneous observation error. In this work, l_0 and l_1 -norm based sparsity inducing penalty functions are considered. We discuss each approach separately in the following subsections.

ZALMS- l_0 algorithms

The l_0 -norm penalty function, denoted by $f_0(\cdot)$, is defined as:

$$f_0(\hat{\mathbf{h}}(k)) = \|\hat{\mathbf{h}}(k)\|_0 = \sum_{k=1}^{G^2} \mathcal{I}(|\hat{\mathbf{h}}(k)| > 0), \quad (3.34)$$

where $\mathcal{I}(\cdot)$ denotes the indicator function. After suitable approximation, as in [102], $\sum_{k=1}^{G^2} \mathcal{I}(|\hat{\mathbf{h}}(k)| > 0) \approx \sum_{k=1}^{G^2} (1 - e^{-\nu(|\hat{\mathbf{h}}(k)|)})$, where ν is the accuracy of the approximation. The gradient term $g(f_0(\hat{\mathbf{h}}(k)))$ is given as:

$$g(f_0(\hat{\mathbf{h}}(k))) = \nu e^{-\nu(|\hat{\mathbf{h}}(k)|)} \times \text{sgn}(\hat{\mathbf{h}}(k)). \quad (3.35)$$

Putting the value of gradient of penalty function $g(f_0(\hat{\mathbf{h}}(k)))$ from (3.35) into (3.33), the update equation for ZALMS- l_0 , is given as:

$$\hat{\mathbf{h}}(k+1) = \hat{\mathbf{h}}(k) + \mu \mathbf{Q}(k) \mathbf{e}(k) - \rho_0 \nu e^{-\nu(|\hat{\mathbf{h}}(k)|)} \times \text{sgn}(\hat{\mathbf{h}}(k)), \quad (3.36)$$

where ρ_0 is regularization parameter ZALMS- l_0 .

ZALMS- l_1 algorithms

The l_1 -norm penalty function $f_1(\cdot)$ [102] can be given as,

$$f_1(\hat{\mathbf{h}}(k)) = \|\hat{\mathbf{h}}(k)\|_1 = \sum_{k=1}^{G^2} |\hat{\mathbf{h}}(k)|. \quad (3.37)$$

The gradient of penalty function is given as,

$$g(f_1(\hat{\mathbf{h}}(k))) = \text{sgn}(\hat{\mathbf{h}}(k)). \quad (3.38)$$

Substituting the value of $g(f_1(\hat{\mathbf{h}}(k)))$ from (3.38) into (3.33) we get,

$$\hat{\mathbf{h}}(k+1) = \hat{\mathbf{h}}(k) + \mu \mathbf{Q}(k) \mathbf{e}(k) - \rho_1 \text{sgn}(\hat{\mathbf{h}}(k)). \quad (3.39)$$

The above equation is weight update recursion of the ZALMS- l_1 norm algorithm. Algorithm-1 provides a step-by-step process as well as the initialization required for the proposed ZALMS technique. Although the beamspace channel's normal initialization $\hat{\mathbf{h}}(0) = \mathbf{0}_{G^2 \times 1}$ yields correct estimates, as shown in simulation results given in Section 3.4. The proposed algorithm typically requires a considerable number of iterations for the MSE to converge. To circumvent this limitation, we can use any of the known sparse signal recovery techniques [93] in the 0^{th} frame to initialize

the proposed ZALMS framework with a suitable sparse estimate. In the sequel, this strategy is referred to as sparse-initialized (SI) ZALMS (SI-ZALMS), and it has been proved to perform better than non-sparse initialization based ZALMS in terms of convergence.

Algorithm 2 Proposed ZALMS Algorithm

Input: Received signal $\mathbf{y} \in \mathbb{C}^{N_T^{Beam} N_R^{Beam} \times 1}$ and sensing matrix $\mathbf{Q} \in \mathbb{C}^{N_T^{Beam} N_R^{Beam} \times N_T N_R}$.

Output: $\hat{\mathbf{H}}$.

- 1: **Initialization:** $\hat{\mathbf{h}}(0) = \mathbf{0}_{G^2 \times 1}$.
 - 2: **for** $n = 1, 2, \dots$ **Do**.
 - 3: $\mathbf{e}(n) = \mathbf{y}(n) - \mathbf{Q}^H(n)\hat{\mathbf{h}}(n)$.
 - 4: Update $\hat{\mathbf{h}}(n+1)$ using (3.30).
 - 5: **End For**
 - 6: $\hat{\mathbf{H}} = \mathbf{A}_R(\Theta_R)\text{vec}^{-1}(\hat{\mathbf{h}})\mathbf{A}_T^H(\Phi_T)$
-

3.3 Parameter Analysis

In this section, range of step size μ that ensures convergence of ZALMS- l_0 , selection of regularization parameter ρ for ZALMS- l_0 , MSD for ZALMS- l_0 , complexity analysis for different estimation algorithms, and impact of RTHIs on the SE are analytically defined.

3.3.1 Bound of Step Size

Proof: Define a weight error vector

$$\tilde{\mathbf{h}}_b(k) \triangleq \hat{\mathbf{h}}(k) - \mathbf{h}_b^{\text{opt}}. \quad (3.40)$$

It measures the difference between the weight estimate at instant n and the optimal weight vector, $\mathbf{h}_b^{\text{opt}}$, that is Wiener solution.

Subtracting $\mathbf{h}_b^{\text{opt}}$ both sides of the recursion (4.31) we obtain

$$\begin{aligned} \tilde{\mathbf{h}}_b(k+1) &= [\mathbf{I} - \mu\mathbf{Q}(k)\mathbf{Q}^H(k)]\tilde{\mathbf{h}}_b(k) + \mu\mathbf{Q}^H(k)\tilde{\mathbf{n}}(k) \\ &\quad - \rho g(f(\hat{\mathbf{h}}(k))). \end{aligned} \quad (3.41)$$

Both sides of (3.41) are postmultiplied with their respective conjugate transposes.

$$\begin{aligned}
 \tilde{\mathbf{h}}_b(k+1)\tilde{\mathbf{h}}_b^H(k+1) &= [\mathbf{I} - \mu\mathbf{Q}(k)\mathbf{Q}^H(k)]\tilde{\mathbf{h}}_b(k)\tilde{\mathbf{h}}_b^H(k)[\mathbf{I} - \mu\mathbf{Q}(k)\mathbf{Q}^H(k)]^H + \\
 &\quad \mu^2\mathbf{Q}^H(k)\tilde{\mathbf{n}}(k)\tilde{\mathbf{n}}^H(k)\mathbf{Q}(k) \\
 &\quad + \rho^2g(f(\hat{\mathbf{h}}(k)))g^T(f(\hat{\mathbf{h}}(k))) + \mu[\mathbf{I} - \mu\mathbf{Q}(k)\mathbf{Q}^H(k)]\tilde{\mathbf{h}}_b(k)\tilde{\mathbf{n}}^H(k)\mathbf{Q}(k) \\
 &\quad + \mu\mathbf{Q}^H(k)\tilde{\mathbf{n}}(k)\tilde{\mathbf{h}}_b^H(k)[\mathbf{I} - \mu\mathbf{Q}(k)\mathbf{Q}^H(k)] \\
 &\quad - \mu\rho[\mathbf{I} - \mu\mathbf{Q}(k)\mathbf{Q}^H(k)]\tilde{\mathbf{h}}_b(k)g^T(f(\hat{\mathbf{h}}(k))) \\
 &\quad - \mu\rho g(f(\hat{\mathbf{h}}(k)))\tilde{\mathbf{h}}_b^H(k)[\mathbf{I} - \mu\mathbf{Q}(k)\mathbf{Q}^H(k)]^H \\
 &\quad - \mu\rho g^H(f(\hat{\mathbf{h}}(k)))\mathbf{Q}^H(k)\tilde{\mathbf{n}}(k) - \mu\rho g(f(\hat{\mathbf{h}}(k)))\tilde{\mathbf{n}}^H(k)\mathbf{Q}(k). \tag{3.42}
 \end{aligned}$$

We assume

$$\mathbf{V}(k) = \mathbb{E}\{\tilde{\mathbf{h}}_b(k)\tilde{\mathbf{h}}_b^H(k)\}, \tag{3.43}$$

represents second moment matrix of weight error vector. Using the independence assumption [128], and taking the expectations on both sides of (3.42), there is

$$\begin{aligned}
 \mathbf{V}(k+1) &= \mathbf{V}(k) - \mu(\mathbf{R}\mathbf{V}(k) + \mathbf{V}(k)\mathbf{R}) + 2\mu^2\mathbf{R}\mathbf{V}(k)\mathbf{R} + \mu^2\mathbf{R}\text{tr}\{\mathbf{R}\mathbf{V}(k)\} \\
 &\quad - 2(\mathbf{I} - \mu\mathbf{R})\rho\mathbb{E}\{\tilde{\mathbf{h}}_b(k)g^H(f(\hat{\mathbf{h}}(k)))\} + \rho^2\mathbb{E}\{g(f(\hat{\mathbf{h}}(k)))g^H(f(\hat{\mathbf{h}}(k)))\} + \\
 &\quad \mu^2\sigma_n^2\mathbf{R}, \tag{3.44}
 \end{aligned}$$

where $\mathbf{R} = \mathbb{E}\{\mathbf{Q}(k)\mathbf{Q}^H(k)\}$. Assume \mathbf{Q} is i.i.d. with mean zero and variance λ , then $\mathbf{R} = \lambda\mathbf{I}$, (3.44) can be simplified as,

$$\begin{aligned}
 \mathbf{V}(k+1) &= (1 - 2\mu\lambda + 2\mu^2\lambda^2)\mathbf{V}(k) + \mu^2\lambda^2\text{tr}\{\mathbf{V}(k)\}\mathbf{I} - \\
 &\quad 2(1 - \mu\lambda)\rho\mathbb{E}\{\tilde{\mathbf{h}}_b(k)g^H(f(\hat{\mathbf{h}}(k)))\} \\
 &\quad + \rho^2\mathbb{E}\{g(f(\hat{\mathbf{h}}(k)))g^H(f(\hat{\mathbf{h}}(k)))\} + \mu^2\sigma_n^2\lambda\mathbf{I}. \tag{3.45}
 \end{aligned}$$

Let

$$U(k) = \text{tr}\{\mathbf{V}(k)\} = \mathbb{E}\{\|\hat{\mathbf{h}}(k) - \mathbf{h}_b^{\text{opt}}\|_2^2\}. \tag{3.46}$$

Taking trace on both sides of (3.45)

$$U(k+1) = \left[1 - 2\mu\lambda + (G+2)\mu^2\lambda^2 \right] U(k) - 2(1-\mu\lambda)\rho\zeta(k) + \rho^2\epsilon(k) + \mu^2\sigma_n^2\lambda G, \quad (3.47)$$

where

$$G = \text{tr}\{\mathbf{I}\}. \quad (3.48)$$

$$\zeta(k) = \mathbb{E}\{\tilde{\mathbf{h}}_b(k)g^H(f(\hat{\mathbf{h}}(k)))\}. \quad (3.49)$$

$$\epsilon(k) = \mathbb{E}\{g(f(\hat{\mathbf{h}}(k)))g^H(f(\hat{\mathbf{h}}(k)))\}. \quad (3.50)$$

To obtain the bound of $\zeta(k)$ and $\epsilon(k)$

$$\begin{aligned} |\zeta(k)| &= |\mathbb{E}\{(\hat{\mathbf{h}}(k) - \mathbf{h}_b^{\text{opt}})g^H(f(\hat{\mathbf{h}}(k)))\}| \\ &\leq \mathbb{E}\{|\hat{\mathbf{h}}(k) - \mathbf{h}_b^{\text{opt}}|g^H(f(\hat{\mathbf{h}}(k)))\}| \\ &\leq \sum_{i=0}^{G-1} \mathbb{E}\{|\hat{h}_{b,i}(k) - h_{b,i}^{\text{opt}}|g^H(f(\hat{h}_{b,i}(k)))\}| \\ &= \sum_{|\hat{h}_{b,i}(k) - h_{b,i}^{\text{opt}}| < \frac{1}{\nu}} \mathbb{E}\{|\hat{h}_{b,i}(k) - h_{b,i}^{\text{opt}}|g^H(f(\hat{h}_{b,i}(k)))\}| \\ &\leq \sum_{|\hat{h}_{b,i}(k) - h_{b,i}^{\text{opt}}| < \frac{1}{\nu}} \mathbb{E}\{|\hat{h}_{b,i}(k) - h_{b,i}^{\text{opt}}|\}|g^H(f(\hat{h}_{b,i}(k)))\}| \\ &\leq \sum_{|\hat{h}_{b,i}(k) - h_{b,i}^{\text{opt}}| < \frac{1}{\nu}} \nu \mathbb{E}\{|\hat{h}_{b,i}(k) - h_{b,i}^{\text{opt}}|\} \\ &(\because |g^H(f(\hat{h}_{b,i}(k)))| < \nu) \\ &\leq \sum_{|\hat{h}_{b,i}(k) - h_{b,i}^{\text{opt}}| < \frac{1}{\nu}} \nu\{\mathbb{E}|\hat{h}_{b,i}(k)| + \|\mathbf{h}_b^{\text{opt}}\|_1\} \\ &\leq G + \nu\|\mathbf{h}_b^{\text{opt}}\|_1. \end{aligned} \quad (3.51)$$

$$\begin{aligned}
 |\epsilon(k)| &= |\mathbb{E}\{g(f(\hat{\mathbf{h}}(k)))g^H(f(\hat{\mathbf{h}}(k)))\}| \\
 &\leq \mathbb{E}\{|g(f(\hat{\mathbf{h}}(k)))g^H(f(\hat{\mathbf{h}}(k)))|\} \\
 &\leq \sum_{i=0}^{G-1} \left\{ |\hat{h}_{b,i}(k)|^2 \right\} \\
 &\leq G\nu^2.
 \end{aligned} \tag{3.52}$$

As a result, to ensure convergence of (3.46), the following equation must be satisfied:

$$|1 - 2\mu\lambda + (G + 2)\mu^2\lambda^2| < 1. \tag{3.53}$$

After simplification (3.53), range of μ can be given as

$$0 < \mu < \frac{2}{\lambda(G + 2)}. \tag{3.54}$$

3.3.2 Selection of Regularization Parameter

Covariance matrix of weight error vector is given from (3.44) as,

$$\begin{aligned}
 \mathbf{V}(k + 1) &= (1 - 2\mu\lambda + 2\mu^2\lambda^2)\mathbf{V}(k) + \mu^2\lambda^2\text{tr}\{\mathbf{V}(k)\}\mathbf{I} \\
 &\quad + \mu^2\sigma_{\tilde{n}}^2\lambda\mathbf{I} + \rho^2\mathbb{E}\{g(f(\hat{\mathbf{h}}(k)))g^H(f(\hat{\mathbf{h}}(k)))\} \\
 &\quad - 2\rho(1 - \mu\lambda)\mathbb{E}\{\tilde{\mathbf{h}}_b(k)g^H(f(\hat{\mathbf{h}}(k)))\}.
 \end{aligned} \tag{3.55}$$

It is noted that the first three terms in the above expression corresponds to the estimation error of LMS i.e. without the regularization term. To ensure the lower estimation error of ZALMS- l_0 than the LMS, 4th and 5th term must be less than zero, i.e.

$$\{\rho^2\mathbb{E}\{g(f(\hat{\mathbf{h}}(k)))g^H(f(\hat{\mathbf{h}}(k)))\} - 2\rho(1 - \mu\lambda)\mathbb{E}\{\tilde{\mathbf{h}}_b(k)g^H(f(\hat{\mathbf{h}}(k)))\}\} < 0. \tag{3.56}$$

By simplifying the above expression the allowable range ρ to ensure convergence is given as follows:

$$0 < \rho < \frac{2(1 - \mu\lambda)\mathbb{E}\{\tilde{\mathbf{h}}_b(k)g^H(f(\hat{\mathbf{h}}(k)))\}}{\mathbb{E}\{g(f(\hat{\mathbf{h}}(k)))g^H(f(\hat{\mathbf{h}}(k)))\}}. \tag{3.57}$$

As $\mathbb{E}\{\tilde{\mathbf{h}}_b(k)g^H(f(\hat{\mathbf{h}}(k)))\} = G + \nu\|\mathbf{h}_b^{\text{opt}}\|_1$ from (3.51) and $\mathbb{E}\{g(f(\hat{\mathbf{h}}(k)))g^H(f(\hat{\mathbf{h}}(k)))\} = G\nu^2$ from (3.52). By putting these values in the expression (3.57) this range is re-expressed as follows:

$$0 < \rho < \frac{2(1 - \mu\lambda)(G + \nu\|\mathbf{h}_b^{\text{opt}}\|_1)}{G\nu^2}. \quad (3.58)$$

3.3.3 MSD Analysis

As from (3.47), MSD is given as

$$U(k+1) = \left[1 - 2\mu\lambda + (G+2)\mu^2\lambda^2\right]U(k) - 2(1 - \mu\lambda)\rho\zeta(k) + \rho^2\epsilon(k) + \mu^2\sigma_n^2\lambda G. \quad (3.59)$$

At steady-state, $n \rightarrow \infty$, $U(k+1) = U(k)$. After simplifying (3.59), at steady-state condition we get

$$U(\infty) = R \left[2\rho(1 - \mu\lambda)\zeta(\infty) + \rho^2\epsilon(\infty) + \mu^2\sigma_n^2\lambda G\right], \quad (3.60)$$

where

$$R = \frac{1}{2\mu\lambda - (G+2)\mu^2\lambda^2}. \quad (3.61)$$

$$\zeta(k) = \mathbb{E}\{\tilde{\mathbf{h}}_b(\infty)g^H(f(\hat{\mathbf{h}}(\infty)))\}. \quad (3.62)$$

$$\epsilon(k) = \mathbb{E}\{g(f(\hat{\mathbf{h}}(\infty)))g^H(f(\hat{\mathbf{h}}(\infty)))\}. \quad (3.63)$$

$$\sigma_n^2 = \mathbb{E}\{\|\tilde{\mathbf{n}}\|^2\}. \quad (3.64)$$

Algorithm	Multiplication	Addition
ZALMS	$2MG_rG_t(N_{RF} + 1)$	$MG_rG_t(2N_{RF} + 1)$
OMP	$\frac{4}{3}(MN_{RF})^3 + \frac{4}{3}(MN_{RF})^2 + MN_{RF}(G_rG_t + 1)$	$\frac{5}{2}(MN_{RF})^3 - (MN_{RF})^2 + MN_{RF}(G_rG_t - 1) - G_rG_t$
R-FSBL	$\mathcal{O}((N_T N_R)(MM_r(MM_r + L) + L^2))$	$\mathcal{O}((N_T N_R)(MM_r(MM_r + L) + L^2))$
BCS-LSE	$\mathcal{O}((N_T N_R)^3)$	$\mathcal{O}((N_T N_R)^3)$

Table 3.1: Complexity comparison of different algorithms

3.3.4 Complexity Analysis

The computational complexities incurred in each frame for the proposed ZALMS algorithms are evaluated in Table-3.1, which compares the number of complex additions and multiplications necessary to estimate the beamspace channel vector \mathbf{h}_b using the proposed ZALMS and existing OMP [93], R-FSBL [126], and BCS-LSE [129] algorithms. The computational complexity of channel estimate in each frame for the ZALMS scheme is in the order of $\mathcal{O}(MN_{RF})$, whereas the same for the OMP is $\mathcal{O}((MN_{RF})^3)$, BCS-LSE is $\mathcal{O}((N_T N_R)^3)$, and R-FSBL is $\mathcal{O}((N_T N_R)(MM_r(MM_r + L) + L^2))$. These complexities are significantly higher than those of the proposed ZALMS-based schemes, thereby making the proposed channel estimator more attractive for deployment in practical mmWave MIMO systems with enhanced performance.

3.3.5 Impact of RTHIs on the SE

As we have considered single user mmWave hybrid MIMO system with N_{RF} number of parallel data stream sent by the transmitter to the receiver. The received signal after processing with considered RTHIs can be given as

$$\begin{aligned}
 \mathbf{y} &= \mathbf{W}^H \mathbf{H}(\mathbf{x} + \mathbf{e}_t) + \mathbf{W}^H \mathbf{e}_r + \mathbf{W}^H \mathbf{n} \\
 &= \mathbf{W}^H \mathbf{H}\mathbf{x} + \mathbf{W}^H \mathbf{H}\mathbf{e}_t + \mathbf{W}^H \mathbf{e}_r + \mathbf{W}^H \mathbf{n} \\
 &= \mathbf{W}^H \mathbf{H}\mathbf{x} + \mathbf{e},
 \end{aligned} \tag{3.65}$$

where $\mathbf{e} = \mathbf{W}^H \mathbf{H}\mathbf{e}_t + \mathbf{W}^H \mathbf{e}_r + \mathbf{W}^H \mathbf{n}$. The SE of the system can be written as,

$$SE = \log_2 \left| \mathbf{I}_{N_{RF}} + \frac{P}{N_{RF}} \tilde{\mathbf{R}}^{-1} \mathbf{W}^H \mathbf{H} \mathbf{F} \mathbf{F}^H \mathbf{H}^H \mathbf{W} \right|, \tag{3.66}$$

where P is the average total transmit power, $\mathbf{I}_{N_{RF}}$ is $N_{RF} \times N_{RF}$ identity matrix, $\tilde{\mathbf{R}} = \mathbf{W}^H \mathbf{R}_e \mathbf{W}$, and $\mathbf{R}_e = \mathbb{E}\{\mathbf{e}\mathbf{e}^H\}$ allows for the following simplification:

$$\mathbf{R}_e = \mathbb{E}\{\mathbf{e}\mathbf{e}^H\} = P \left(\frac{\kappa_t}{N_{RF}} + \kappa_r \right) \mathbf{H}\mathbf{H}^H + \sigma_n^2 \mathbf{I}. \quad (3.67)$$

As the design of precoder and combiner depends on singular value decomposition (SVD) of channel estimated value $\hat{\mathbf{H}}$ [93]. Therefore, the SE is found to depend on the accuracy of channel estimation as observed from (3.66).

3.4 Simulation Results

Simulation and analytical results are presented to validate the performance of the algorithms. NMSE versus iteration and NMSE versus SNR plots are demonstrated to show the estimation accuracy of the proposed algorithms, as well as OMP, SBL, and BCS, at various impairment levels for the considered system. An NMSE versus iteration plot for the proposed SI-ZALMS is also presented. Additionally, MSE versus step size (μ) and MSE versus regularization parameter (ρ) plots are demonstrated to select the appropriate parameters for the algorithms. Furthermore, SE versus SNR plots for various values of κ_t and κ_r are shown to illustrate the performance of the proposed estimator. For the simulation, we considered one BS and MS, each equipped with 32 antennas and 8 RF chains. ULA antenna arrays with antenna spacing of $\lambda/2$ are used, and phase shifters are included in the RF precoders.

The considered channel is assumed as geometric channel as defined in (3.6), with 3 paths. Without loss of generality, α is considered as Rayleigh distributed, angle of arrival and departure are 32 discrete values in the range $[0 \ 2\pi]$. For MSE performance curve considered simulation parameters are as, step size (μ) = 3×10^{-2} , regularization parameter (ρ_0) for ZA-LMS- l_0 is 5×10^{-6} , and (ρ_1) for ZA-LMS- l_1 is 5×10^{-5} , accuracy parameter (ν) for ZA-LMS- l_0 is 20, $\kappa_t = \kappa_r \in \{0.05^2, 0.15^2\}$. The SNR for estimation is fixed 20 dB for all the illustrated cases, and the SNR range for spectral efficiency calculation is from -40dB to 20dB [43]. All the simulations are ensemble averaged over by 500 Monte Carlo runs.

It is observed from Figure 3.4, that the ZALMS based algorithms outperforms other algorithms as MSE floor is lower by 4.84×10^{-3} when impairment level at the

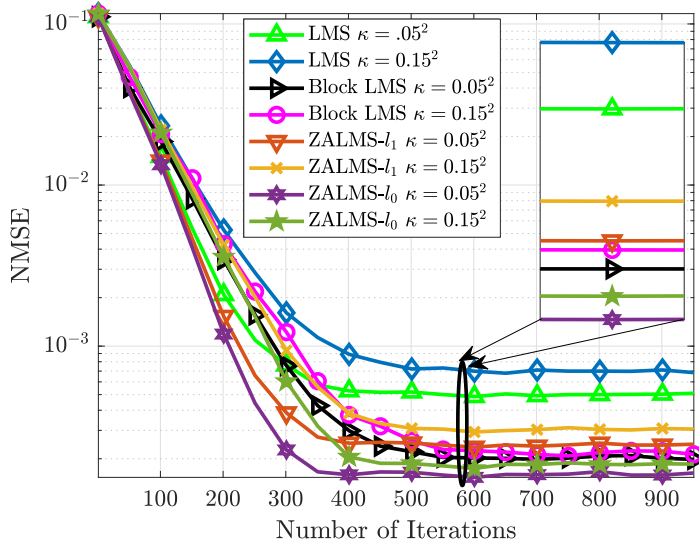


Figure 3.4: NMSE versus number of iterations performance of LMS, block LMS, and ZALMS with two impairment level $\kappa_t = \kappa_r = 0.05^2$ and $\kappa_t = \kappa_r = 0.15^2$ with $N_{RF} = 8$, $N_T = N_R = 32$, $L = 2$, $\rho_0 = 5 \times 10^{-5}$, $\rho_1 = 1 \times 10^{-6}$, $\mu = 0.03$, and SNR = 20 dB.

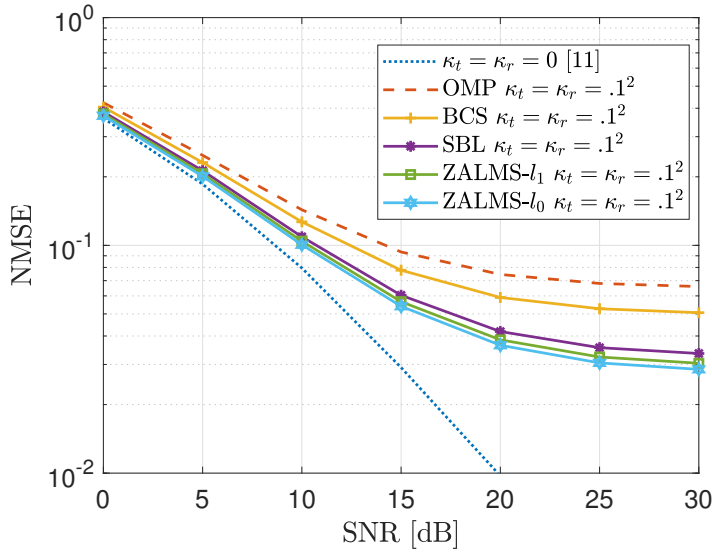


Figure 3.5: NMSE versus SNR performance of OMP, BCS, SBL, ZALMS- l_1 , and ZALMS- l_0 with impairment level $\kappa_t = \kappa_r = 0.1^2$, $N_{RF} = 8$, $N_T = N_R = 32$, $L = 2$, $\rho_0 = 5 \times 10^{-5}$, $\rho_1 = 1 \times 10^{-6}$, $\mu = 0.03$.

transmitter and receiver is 0.05^2 and lower by 4.51×10^{-3} when impairment level is 0.15^2 from LMS, for which ideal hardware i.e. $\kappa_t = \kappa_r = 0$ is considered and in robustness as there is very small variation in MSE floor when impairments level varies from 0.05^2 to 0.15^2 . For a mmWave configuration with simulation parameters set as $N_T = N_R = 32$; $N_{RF} = 8$; $G_T = G_R = 32$; $M = 20$.

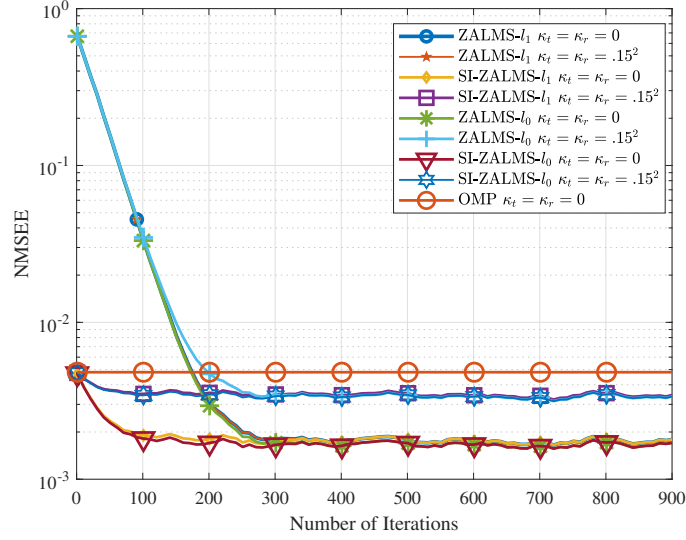


Figure 3.6: NMSE versus number of iterations performance of zero-initiated and sparse-initiated ZALMS- l_0 , ZALMS- l_1 , with $\kappa_t = \kappa_r = 0.05^2$, $N_{RF} = 8$, $N_T = N_R = 32$, $L = 2$, $\rho_0 = 5 \times 10^{-5}$, $\rho_1 = 1 \times 10^{-6}$, $\mu = 0.03$, and SNR = 20 dB.

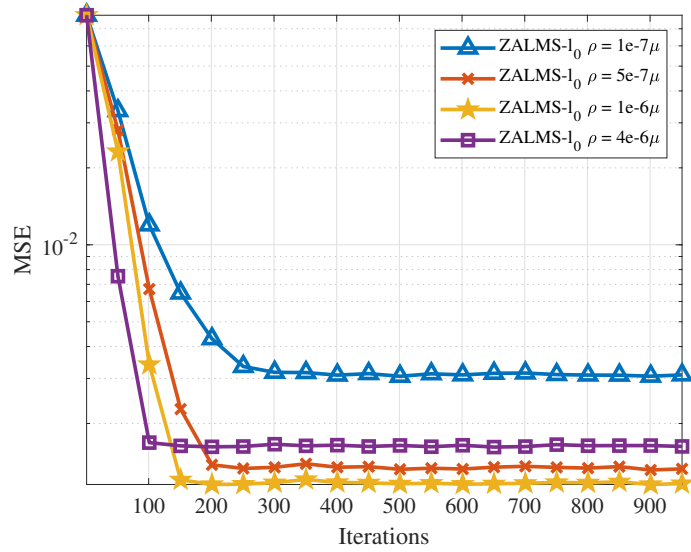


Figure 3.7: MSE versus iterations performance of ZALMS- l_0 for different values of ρ at impairments level $\kappa_t = \kappa_r = 0.05^2$, $L = 2$, $N_T = N_R = 32$, $N_{RF} = 8$, $\mu = .03$, and SNR = 20 dB.

Figure 3.5, compares the NMSE versus SNR performance of the proposed ZALMS-based schemes upon convergence and that of the existing OMP, BCS, and SBL techniques for mmWave hybrid MIMO systems with ideal hardware ($\kappa_t = \kappa_r = 0$) and with impairments level $\kappa_t = \kappa_r = 0.1^2$ and simulation parameters $N_T = N_R = 32$; $N_{RF} = 8$; $G_T = G_R = 32$ and $L = 2$. From the figure, it is obvious that NMSE of all the schemes is seen to improve with SNR. Further, it can be observed that

the NMSE performance of the proposed ZALMS techniques is notably better than the existing algorithms (e.g., OMP, BCS, and SBL) for same level of impairments. Furthermore, it is also clear from the plot that the NMSE decreases monotonically with SNR in case of ideal hardware whereas in case of non-ideal hardware NMSE does not decrease continuously and reduces error floor at fixed SNR ($\approx 25\text{dB}$) due to the effect of hardware impairment.

Figure 3.6, depicts the NMSE performance of SI-ZALMS- l_0 and SI-ZALMS- l_1 techniques. That use the initial estimate obtained from the OMP technique to the 0^{th} frame. It is observed that SI-ZALMS converges approximately 150 iterations before than the zero initialization ZALMS.

Further, Figure 3.7, depicts MSE performance plot of ZALMS- l_0 for different reg-

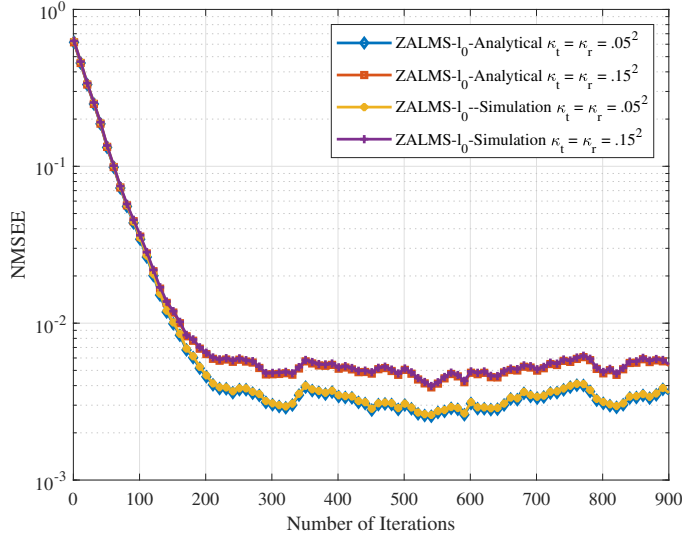


Figure 3.8: Simulation and analytical performance plot of NMSE versus iterations of ZALMS- l_0 , at different impairments level.

ularization parameter ρ with simulation parameters $\kappa_t = \kappa_r = 0.15^2$, $N_T = 32$, $N_R = 32$, $N_{RF} = 8$, $L = 2$, SNR = 35 dB, and $\mu = 0.03$. ZALMS- l_0 has lowest MSE floor and fastest convergence rate at $\rho_0 = 1 \times 10^{-6}$.

Figure 3.8, shows the analytical and simulation plot for NMSE vs number of iterations at two different impairment level $\kappa_t = \kappa_r = 0.05^2$ and $\kappa_t = \kappa_r = 0.15^2$. From this figure it is clear that if impairments level increases, NMSE floor decreases, which is verified by both simulation as well as analytical plots.

Furthermore, it is evident from Figure 3.9, which is MSE performance plot of ZALMS- l_0 for different step size parameter μ with simulation parameters $\kappa_t = \kappa_r =$

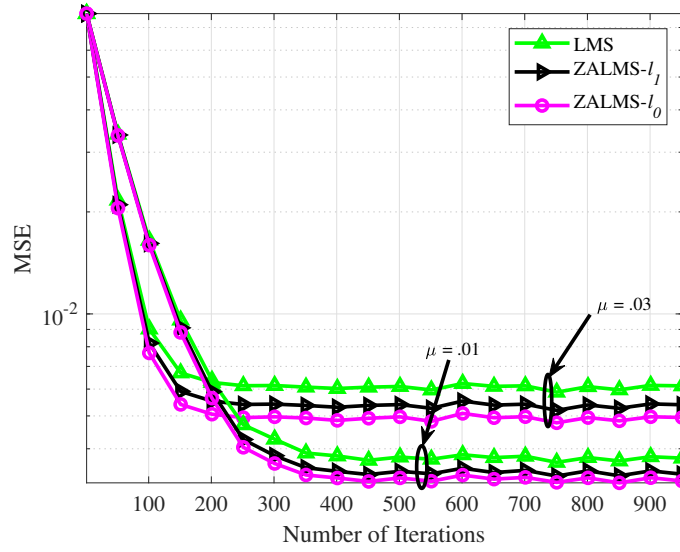


Figure 3.9: MSE versus iterations performance of LMS, ZALMS- l_1 , and ZALMS- l_0 for different μ .

0.15^2 , $N_T = 32$, $N_R = 32$, $N_{RF} = 8$, $L = 2$, SNR = 20 dB, and $\rho = 5 \times 10^{-8}$, as the value of μ increases, MSE floor increases means estimation quality decreases but convergence rate improved, which allows for a trade off between estimation quality and convergence rate in selecting the value of step size parameter.

Figure 3.10, depicts the dependence of MSE floor and convergence rate on the step size, μ , and the regularization parameter, ρ . In this context, simulations are shown for various values of μ and ρ in Figure 3.10. Hence, for better estimation and faster convergence value of μ and ρ are chosen accordingly.

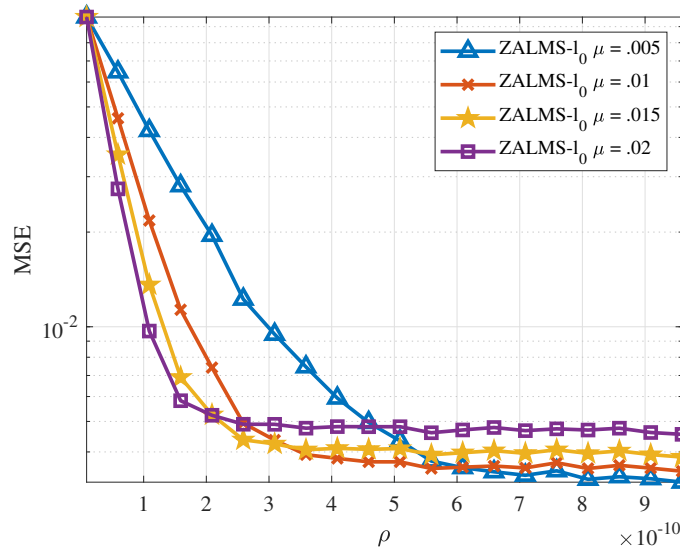


Figure 3.10: MSE versus ρ performance of ZALMS- l_0 for different μ

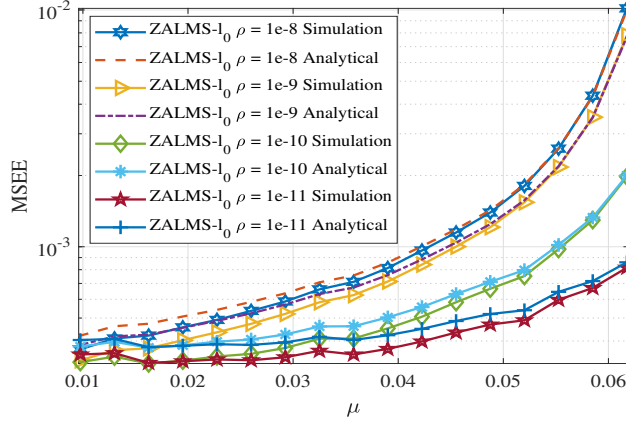


Figure 3.11: MSEE vs μ simulation and analytical plots of ZALMS- l_0 for various ρ . The analytical MSEE for ZALMS- l_0 have been evaluated using (3.60).

Figure 3.11, compares MSEE performance versus step size (μ) of ZALMS- l_0 for various regularization parameter (ρ). It is obvious from the plot that when value of μ increases MSEE also increases and it increases more rapidly when the value of ρ increases, which is further analytically verified using (3.60). To summarize, this allows for parameter selection for accurate estimation.

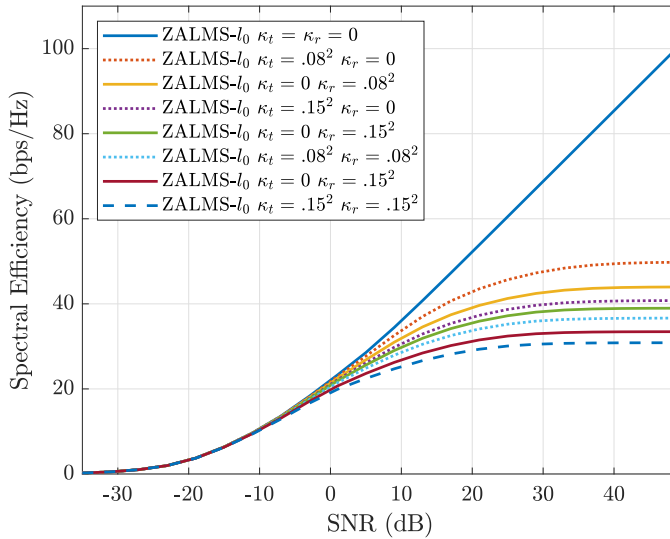


Figure 3.12: SE versus the SNR performance plot of ZALMS- l_0 for different values of κ_t and κ_r with $N_T = 32$, $N_R = 32$ and $N_{RF} = 8$.

Figure 3.12, shows SE versus SNR performance of ZALMS- l_0 for different values of κ_t and κ_r . From the figure, we can observe that the residual transceiver hardware impairments (RATHIs) has negligible effect in the low SNR regime (less than 0 dB) as compared with the ideal transceiver system. Whereas, the impact of HIs can be observed in the high SNR region (greater than 0 dB). Further, we observe that the

SE decreases with the increases in κ_t and κ_r . It is also observed that κ_r has severe impact than compared with κ_t . The ceiling phenomena is observed at high SNR i.e., the SE does not increase with the SNR after 20dB, which can be clearly observed from Figure 3.12.

3.5 Summary

In this work, the impact of various hardware impairments on mmWave hybrid MIMO systems at the transceiver is considered while estimating the narrowband mmWave hybrid MIMO channels. For that low-complexity adaptive online channel estimators based on ZALMS to exploit the sparsity of mmWave hybrid MIMO systems is proposed. Further, to enhance the convergence of the ZALMS, SI-ZALMS has been proposed. The theoretical MSD and MSE, as well as the related equations for their asymptotic values, are determined. Next, the ranges are derived analytically for possible step size and regularization parameter values. From simulations, it is observed that the proposed ZALMS-based channel estimators outperformed the existing OMP-based technique in terms of CSI estimate considering the hardware impairments. Lastly, the impact of RTHI on spectral efficiency is also derived.

Chapter 4

VSS-ZALMS based Channel Estimator for IRS-Aided mmWave Hybrid MIMO System

In the previous chapters, channel estimation for mmWave hybrid MIMO system considering ideal hardware and with HI is performed. However, in this chapter IRS-aided mmWave hybrid MIMO system is considered.

Millimeter-wave (mmWave) systems operating in the 30-300 GHz spectrum are a key technology for future wireless communication, owing to their ability to provide ultra high data rates and overcome spectrum scarcity [43, 130, 131]. In mmWave communications, large antenna arrays are typically used to generate highly directional beams that compensate for substantial path loss compared to the sub-6 GHz band. However, this high directivity makes mmWave communication more susceptible to signal obstruction [116]. IRS is seen as a solution to increase the coverage of mmWave communication systems in blocked and deep fading scenarios [132, 133]. Typically, IRS is an artificial metasurface made up of many low-cost passive reflecting units that are effectively controlled by a smart controller [134]. By altering the amplitude and phase of the incident signals, the IRS intelligently reflects the signals from the base BS to the user equipment (UE). When the direct channel between the BS and the UE is blocked, an IRS can create a concatenated BS-IRS-UE channel, thus enhancing the coverage of mmWave systems. Since expensive RF components are not used in a passive IRS, it is seen as a practical and economical solution.

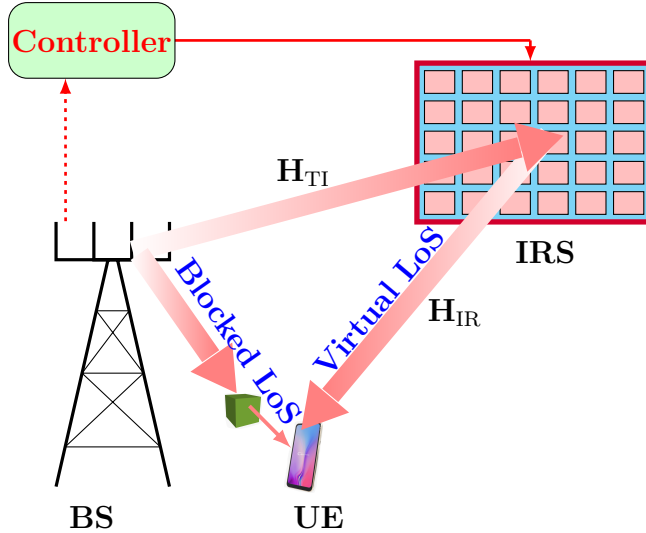


Figure 4.1: Diagram of the IRS-assisted communication system.

However, accurate CSI is necessary for joint active and passive beamforming in order to maximize the IRS and mmWave MIMO benefits. The channel estimation of IRS-aided wireless systems has been studied in the literature [135–139]. In [135], active elements are used in IRS to estimate the channel. These active elements have the ability to function in the receive mode, allowing them to pick up incident signals that can be used to estimate the BS-IRS channel and the IRS-user channel. However, the IRSs that have active components require wire or battery power, which may not be practical for many applications. In [136, 137], a cascade channel estimation technique for passive IRS using the least squares (LS) method is proposed. However, since these techniques do not leverage the sparse structure present in mmWave wireless channels, they necessitate a significant number of pilots. Thus, in this work, we consider channel estimation for IRS-assisted mmWave MIMO systems. We perform sparse representation of the cascaded BS-IRS-UE channel using the Khatri-Rao and Kronecker products, and exploit this sparsity using the zero-attracting principle.

We propose a cascaded sparse online channel estimator (estimator that continually adapts to changes in the input data stream as it is received, rather than processing the entire dataset at once as a block update. This means updates are made to its parameters in real time as new data becomes available) based on a variable step size (VSS) zero-attracting least mean square (ZALMS) algorithm. Since the step size varies in accordance with MSE, the VSS-ZALMS-based estimators offer

better accuracy, tracking, and convergence rate as compared to fixed step size (FSS) adaptive algorithms. Since there is no matrix inversion required for the composite channel, the suggested technique offers lower computation cost and thus reduces estimation delay. From this perspective, the major contributions of this work are:

- VSS-ZALMS-based channel estimator is proposed for the cascaded channel between the BS-IRS-UE in IRS-assisted mmWave hybrid MIMO channels, formulated using Kronecker products.
- For the considered system, a sparse channel estimation model is developed in the beamspace domain. This model includes a sparsifying dictionary composed of quantized receive and transmit array response vectors.
- The proposed method is applicable for both stationary and nonstationary conditions in IRS-aided mmWave hybrid MIMO systems, emphasizing its versatility and practical importance.
- Analytical expressions for the range of regularization parameters and step size parameters are derived for VSS-ZALMS, ensuring lower NMSE compared to classical LMS. Additionally, an analysis is performed on IRS location, SE, pilot overhead requirements, and computational complexity.
- Performance of the proposed channel estimator is compared with the existing methods e.g. OMP and SBL and also for oracle least square (LS) for benchmarking purpose. Simulation results corroborate the superiority of the suggested estimator in terms of accuracy, complexity, and robustness compared to existing estimators.

4.1 System and Channel Model

Figure 4.1 depicts a downlink IRS-assisted communication system, in which an IRS is used to aid signal transmission from the BS to the UE when the direct path is obstructed. The IRS-assisted mmWave hybrid MIMO transceiver is shown in Figure 4.2, in which the BS transmits signals using N_T transmit antennas to the UE, which is equipped with N_R receive antennas through an IRS. The IRS under consideration

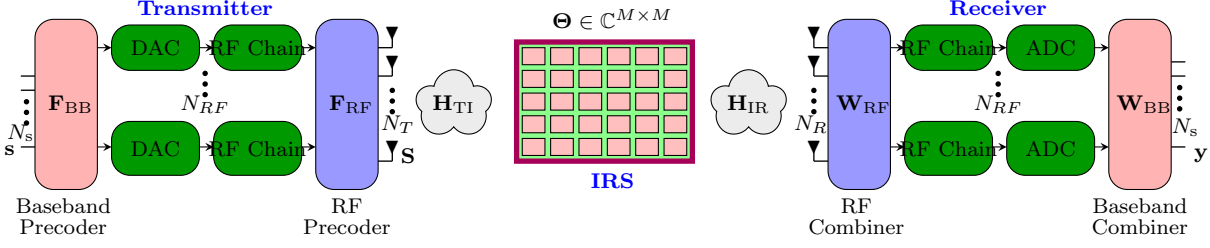


Figure 4.2: Diagram illustrating the channel estimation for an IRS-assisted mmWave hybrid MIMO transceiver.

is a uniform planar array (UPA) consisting of M low-cost passive reflecting elements. Let, $\mathbf{H}_{\text{TI}} \in \mathbb{C}^{M \times N_T}$ and $\mathbf{H}_{\text{IR}} \in \mathbb{C}^{N_R \times M}$ denote the channel from the BS to the IRS, and from the IRS to the UE, respectively. Because of blockage, the LoS path between the BS and the UE is not considered. The IRS reflection matrix Θ is used to model the IRS and is given by $\Theta = \text{diag}([\kappa_1 e^{j\theta_1}, \dots, \kappa_M e^{j\theta_M}]) \in \mathbb{C}^{M \times M}$, where $\kappa_m \in [0, 1]$ and $\theta_m \in [0, 2\pi)$ denote the amplitude reflection and phase change of the m -th IRS element. Each element of the IRS reflects the received signal in a controllable manner, with control provided by the BS. The total cascaded channel matrix $\mathbf{H} \in \mathbb{C}^{N_R \times N_T}$ from the BS to the UE can be expressed as

$$\mathbf{H} = \mathbf{H}_{\text{IR}} \Theta \mathbf{H}_{\text{TI}}. \quad (4.1)$$

Suppose the BS transmits N_s data streams to the UE using the digital baseband precoder $\mathbf{F}_{\text{BB}} \in \mathbb{C}^{N_{\text{RF}}^T \times N_s}$ and the analog RF precoder $\mathbf{F}_{\text{RF}} \in \mathbb{C}^{N_T \times N_{\text{RF}}^T}$. The UE utilizes the analog RF combiner $\mathbf{W}_{\text{RF}} \in \mathbb{C}^{N_R \times N_{\text{RF}}^R}$ and the baseband combiner $\mathbf{W}_{\text{BB}} \in \mathbb{C}^{N_{\text{RF}}^R \times N_s}$ to process the received signal. Here, N_{RF}^T and N_{RF}^R refers to the quantities of RF chains at the BS and the UE, respectively with the constraint $N_s \leq \min(N_{\text{RF}}^T, N_{\text{RF}}^R) \ll \min(N_T, N_R)$. Each element of the RF precoder \mathbf{F}_{RF} and combiner \mathbf{W}_{RF} follows the constraint $|[\mathbf{W}_{\text{RF}}]_{m,n}| = 1/\sqrt{N_R}$, $|[\mathbf{F}_{\text{RF}}]_{m,n}| = 1/\sqrt{N_T}$, $\forall m, n$, as these are designed with phase shifters. The processed received signal is given as [13]

$$\mathbf{y} = \mathbf{W}_{\text{BB}}^H \mathbf{W}_{\text{RF}}^H \mathbf{H} \mathbf{F}_{\text{RF}} \mathbf{F}_{\text{BB}} \mathbf{s} + \mathbf{W}_{\text{BB}}^H \mathbf{W}_{\text{RF}}^H \mathbf{n}, \quad (4.2)$$

where $\mathbf{s} \in \mathbb{C}^{N_s \times 1}$ is signal vector sent in the t^{th} time frame with a covariance matrix $\mathbb{E}\{\mathbf{s}\mathbf{s}^H\} = (P_s/N_s)\mathbf{I}_{N_s}$, and $\mathbf{n} \in \mathbb{C}^{N_R \times 1}$ is the noise vector with $\mathcal{CN}(\mathbf{0}, \sigma_n^2 \mathbf{I}_{N_R})$. In

this work, we examine a quasi-static channel characterized by a coherence time T , implying that the channel remains constant within each transmitted block of duration T . Let $\mathbf{x} \in \mathbb{C}^{N_T \times 1}$ in the t^{th} time frame, given as $\mathbf{x} = \mathbf{F}_{RF}\mathbf{F}_{BB}\mathbf{s} = \mathbf{F}\mathbf{s}$. Then, the observed signal $\mathbf{y} \in \mathbb{C}^{N_s \times 1}$ at the UE can be expressed as $\mathbf{y} = \mathbf{W}^H\mathbf{H}\mathbf{x} + \tilde{\mathbf{n}}$, where $\tilde{\mathbf{n}} = \mathbf{W}^H\mathbf{n}$, and $\mathbf{W} = \mathbf{W}_{RF}\mathbf{W}_{BB} \in \mathbb{C}^{N_R \times N_s}$ is the hybrid combiner. For the total T time frames, the received signal matrix at the UE can be given as

$$\mathbf{Y} = \mathbf{W}^H\mathbf{H}\mathbf{X} + \tilde{\mathbf{N}}, \quad (4.3)$$

Here, \mathbf{X} represents an $N_T \times T$ pilot matrix, \mathbf{Y} is an $N_s \times T$ matrix of received signals, and $\tilde{\mathbf{N}}$ is an $N_s \times T$ matrix representing noise. Due to IRS the number of path between IRS and UE increases, hence, sparsity level of channel matrix decreases. This may cause sparse estimator gives slightly poor response. However, for single IRS effect will be negligible.

4.1.1 Channel Model for IRS aided mmWave System

We have examined a downlink propagation scenario, employing a geometric channel model to characterize the propagation environment. In this model, the mmWave channel is represented as follows [140],

$$\mathbf{H}_{\text{TI}} = \sqrt{\frac{N_{\text{T}}M}{\eta}} \sum_{l=1}^L \alpha_l \mathbf{a}_{\text{IRS}}(\psi_l, \gamma_l) \mathbf{a}_{\text{BS}}^H(\phi_l), \quad (4.4)$$

$$\mathbf{H}_{\text{IR}} = \sqrt{\frac{N_{\text{R}}M}{\mu}} \sum_{l'=1}^{L'} \beta_{l'} \mathbf{a}_{\text{UE}}(\phi_{l'}) \mathbf{a}_{\text{IRS}}^H(\psi_{l'}, \gamma_{l'}), \quad (4.5)$$

where η is the path loss, α_l is the complex path gain of the l^{th} path, and L denotes the number of paths of the BS-IRS link. $\psi_l(\gamma_l)$ denotes the azimuth (elevation) AoA of the l^{th} path, and ϕ_l is the AoD of the l^{th} path between the BS-IRS link. Similarly, μ , $\beta_{l'}$, $\psi_{l'}(\gamma_{l'})$, $\phi_{l'}$, and L' denote path loss, the complex path gain, azimuth (elevation) AoD, AoA of the l'^{th} path, and the number of paths between the IRS-UE link, respectively. Besides, \mathbf{a}_{BS} , \mathbf{a}_{IRS} , and \mathbf{a}_{UE} are the transmit and the receive array response vectors (ARVs) at the BS, the IRS, and the UE, respectively, that are defined as

$$\mathbf{a}_{\text{BS}}(\phi_l) = \frac{1}{\sqrt{N_T}} \left[1, e^{\frac{j2\pi d \cos(\phi_l)}{\lambda}}, \dots, e^{\frac{j2\pi d(N_T-1) \cos(\phi_l)}{\lambda}} \right]^T, \quad (4.6)$$

$$\mathbf{a}_{\text{UE}}(\phi_l) = \frac{1}{\sqrt{N_R}} \left[1, e^{\frac{j2\pi d \cos(\phi_l)}{\lambda}}, \dots, e^{\frac{j2\pi d(N_R-1) \cos(\phi_l)}{\lambda}} \right]^T, \quad (4.7)$$

where d is a consecutive antenna spacing and λ is the carrier signal's wavelength. In this work, IRS is assumed to be a $M_x \times M_y$ URA with $M \triangleq M_x M_y$ reflecting units. The ARV of the IRS is expressed as [138]

$$\mathbf{a}_{\text{IRS}}(\psi_l, \gamma_l) = \mathbf{a}_x(\psi_l, \gamma_l) \otimes \mathbf{a}_y(\gamma_l), \quad (4.8)$$

where \otimes stands for Kronecker product. The term $\mathbf{a}_x(\psi_l, \gamma_l)$ and $\mathbf{a}_y(\gamma_l)$ can be expressed as

$$\mathbf{a}_x(\psi_l, \gamma_l) = \frac{1}{\sqrt{M_x}} \left[1, e^{\frac{j2\pi \hat{d} \sin(\gamma_l) \cos(\psi_l)}{\lambda}}, \dots, e^{\frac{j2\pi \hat{d}(M_x-1) \sin(\gamma_l) \cos(\psi_l)}{\lambda}} \right]^T, \quad (4.9)$$

$$\mathbf{a}_y(\gamma_l) = \frac{1}{\sqrt{M_y}} \left[1, e^{\frac{j2\pi \hat{d} \cos(\gamma_l)}{\lambda}}, \dots, e^{\frac{j2\pi \hat{d}(M_y-1) \cos(\gamma_l)}{\lambda}} \right]^T. \quad (4.10)$$

We have assumed that \hat{d} represents the spacing between consecutive reflecting elements, and that the paths L and L' are known at the BS.

4.1.2 Beamspace Representation of Channel

Channel in (4.4) and (4.5) can be represented in compact form [138] as

$$\mathbf{H}_{\text{TI}} = \mathbf{A}_{\text{IRS}} \mathbf{\Lambda}_\alpha \mathbf{A}_{\text{BS}}^H, \quad \mathbf{H}_{\text{IR}} = \mathbf{A}_{\text{UE}} \mathbf{\Lambda}_\beta \mathbf{A}_{\text{IRS}}^H, \quad (4.11)$$

where $\mathbf{A}_{\text{BS}} \in \mathbb{C}^{N_T \times G_{\text{BS}}}$, $\mathbf{A}_{\text{IRS}} \in \mathbb{C}^{M \times G_{\text{I}}}$, and $\mathbf{A}_{\text{UE}} \in \mathbb{C}^{N_R \times G_{\text{UE}}}$ are overcomplete array response dictionary matrices (ARDM) at the base station, IRS, and at the user, respectively. G_{BS} , G_{I} , and G_{UE} denote their respective angular resolutions. $\mathbf{\Lambda}_\alpha \in$

$\mathbb{C}^{G_I \times G_{BS}}$ and $\mathbf{\Lambda}_\beta \in \mathbb{C}^{G_{UE} \times G_I}$ are two sparse matrices with L and L' non-zero elements corresponding to channel path gain α_l and $\beta_{l'}$, respectively. According to (4.6) and (4.7), the ARDM \mathbf{A}_{BS} and \mathbf{A}_{UE} can be given as $\mathbf{A}_{BS} = [\mathbf{a}_{BS}(\phi_1), \dots, \mathbf{a}_{BS}(\phi_{G_{BS}})]$ and $\mathbf{A}_{UE} = [\mathbf{a}_{UE}(\phi_1), \dots, \mathbf{a}_{UE}(\phi_{G_{UE}})]$, respectively. Similarly, according to (4.8), the ARDM \mathbf{A}_{IRS} is given as

$$\mathbf{A}_{IRS} = \mathbf{A}_x \otimes \mathbf{A}_y, \quad (4.12)$$

where $\mathbf{A}_x = [\mathbf{a}_x(\psi_1, \gamma_1), \dots, \mathbf{a}_x(\psi_{G_x}, \gamma_{G_x})]$ and $\mathbf{A}_y = [\mathbf{a}_y(\gamma_1), \dots, \mathbf{a}_y(\gamma_{G_y})]$, where $G_I = G_x G_y$ and G_x, G_y denote the angular resolutions along the x and y -axis, respectively.

4.1.3 Problem Formulation

Vectorizing the cascaded channel \mathbf{H} in (4.1) after substituting \mathbf{H}_{TI} and \mathbf{H}_{IR} from (4.11)

$$\begin{aligned} \text{vec}(\mathbf{H}) &= \text{vec}(\mathbf{A}_{UE} \mathbf{\Lambda}_\beta \mathbf{A}_{IRS}^H \mathbf{\Theta} \mathbf{A}_{IRS} \mathbf{\Lambda}_\alpha \mathbf{A}_{BS}^H) \\ &\stackrel{(a)}{=} (\mathbf{A}_{BS}^* \otimes \mathbf{A}_{UE}) \text{vec}(\mathbf{\Lambda}_\beta \mathbf{A}_{IRS}^H \mathbf{\Theta} \mathbf{A}_{IRS} \mathbf{\Lambda}_\alpha) \\ &\stackrel{(b)}{=} (\mathbf{A}_{BS}^* \otimes \mathbf{A}_{UE}) (\mathbf{\Lambda}_\alpha^T \otimes \mathbf{\Lambda}_\beta) (\mathbf{A}_{IRS}^T \odot \mathbf{A}_{IRS}^H) \text{vecd}(\mathbf{\Theta}) \\ &\stackrel{(c)}{=} (\mathbf{A}_{BS}^* \otimes \mathbf{A}_{UE}) (\mathbf{\Lambda}_\alpha^T \otimes \mathbf{\Lambda}_\beta) \mathbf{A}_D \mathbf{z}, \end{aligned} \quad (4.13)$$

where (a) and (b) is from vectorization of triple matrix product and (c) is by replacing $\text{vecd}(\mathbf{\Theta}) \in \mathbb{C}^{M \times 1}$ to \mathbf{z} and $\mathbf{A}_D = (\mathbf{A}_{IRS}^T \odot \mathbf{A}_{IRS}^H) \in \mathbb{C}^{G_I^2 \times M}$. With the channel model as in (4.13), the received signal \mathbf{Y} in (4.3) can be vectorized $\mathbf{y} = \text{vec}(\mathbf{Y})$ as

$$\begin{aligned} \mathbf{y} &= (\mathbf{S}^T \otimes \mathbf{W}^H) \text{vec}(\mathbf{H}) + \text{vec}(\tilde{\mathbf{N}}) \\ &\stackrel{(a)}{=} (\mathbf{S}^T \otimes \mathbf{W}^H) (\mathbf{A}_{BS}^* \otimes \mathbf{A}_{UE}) (\mathbf{\Lambda}_\alpha^T \otimes \mathbf{\Lambda}_\beta) (\mathbf{A}_{IRS}^T \odot \mathbf{A}_{IRS}^H) \mathbf{z} + \text{vec}(\tilde{\mathbf{N}}). \end{aligned} \quad (4.14)$$

The term $(\mathbf{\Lambda}_\alpha^T \otimes \mathbf{\Lambda}_\beta) (\mathbf{A}_{IRS}^T \odot \mathbf{A}_{IRS}^H)$ in (4.14) can be simplified as (from [141])

$$(\mathbf{\Lambda}_\alpha^T \otimes \mathbf{\Lambda}_\beta) (\mathbf{A}_{IRS}^T \odot \mathbf{A}_{IRS}^H) = \underbrace{\left(\sum_{k=1}^{G_I} (\lambda_k \otimes \Lambda_\beta) \mathbf{P}_k \right)}_{\hat{\mathbf{A}}} \mathbf{A}_{IRS}^T, \quad (4.15)$$

where \mathbf{P}_k is a permutation matrix that changes position of the rows of \mathbf{A}_{IRS} , $\boldsymbol{\lambda}_k \in \mathbb{C}^{G_{\text{BS}} \times 1}$ is k^{th} column of $\boldsymbol{\Lambda}_\alpha^T$ and $\hat{\boldsymbol{\Lambda}} \in \mathbb{C}^{G_{\text{BS}} G_{\text{UE}} \times G_{\text{I}}}$ is sparse matrix with LL' non-zero elements. Lastly, substituting the value of $(\boldsymbol{\Lambda}_\alpha^T \otimes \boldsymbol{\Lambda}_\beta) (\mathbf{A}_{\text{IRS}}^T \odot \mathbf{A}_{\text{IRS}}^H)$ from (4.15) into (4.14), we get where $\boldsymbol{\Lambda}_k \in \mathbb{C}^{G_{\text{BS}} \times 1}$ denotes the k^{th} column of $\boldsymbol{\Lambda}_\alpha^T$ and $\hat{\boldsymbol{\Lambda}} \in \mathbb{C}^{G_{\text{BS}} G_{\text{UE}} \times G_{\text{I}}}$ is sparse matrix with LL' non-zero elements. Finally, substituting the results of (4.15) into (4.14), we have

$$\begin{aligned} \mathbf{y} &= \left(\mathbf{S}^T \otimes \mathbf{W}^H \right) \left(\mathbf{A}_{\text{BS}}^* \otimes \mathbf{A}_{\text{UE}} \right) \hat{\boldsymbol{\Lambda}} \mathbf{A}_{\text{IRS}}^T \mathbf{z} + \tilde{\mathbf{n}} \\ &\stackrel{\text{(a)}}{=} \left((\mathbf{z}^T \mathbf{A}_{\text{IRS}}) \otimes \left((\mathbf{S}^T \otimes \mathbf{W}^H) \left(\mathbf{A}_{\text{BS}}^* \otimes \mathbf{A}_{\text{UE}} \right) \right) \right) \mathbf{h}_b + \tilde{\mathbf{n}} \\ &\stackrel{\text{(b)}}{=} \mathbf{Q} \mathbf{h}_b + \tilde{\mathbf{n}}, \end{aligned} \quad (4.16)$$

where $\mathbf{h}_b = \text{vec}(\hat{\boldsymbol{\Lambda}}) \in \mathbb{C}^{G_{\text{BS}} G_{\text{UE}} G_{\text{I}} \times 1}$ is a sparse channel vector to be estimated and $\tilde{\mathbf{n}} = \text{vec}(\tilde{\mathbf{N}})$. Equation (b) is obtained by substituting $\mathbf{Q} \triangleq \left((\mathbf{z}^T \mathbf{A}_{\text{IRS}}) \otimes (\mathbf{S}^T \otimes \mathbf{W}^H) \left(\mathbf{A}_{\text{BS}}^* \otimes \mathbf{A}_{\text{UE}} \right) \right) \in \mathbb{C}^{N_s T \times G_{\text{BS}} G_{\text{UE}} G_{\text{I}}}$. The system model in (4.16) is a sparse signal recovery problem [142]. Because of the complexity reduction, we adopt a VSS-ZALMS based approach to estimate the channel \mathbf{h}_b . Ultimately, with the obtained \mathbf{h}_b , the estimated channel $\hat{\mathbf{H}}$ can be found as

$$\hat{\mathbf{H}} = \left(\mathbf{A}_{\text{BS}}^* \otimes \mathbf{A}_{\text{UE}} \right) \mathbf{H}_b \mathbf{A}_{\text{IRS}}^T, \quad (4.17)$$

here the \mathbf{H}_b is obtained by matricization of \mathbf{h}_b .

4.2 Adaptive Filtering Framework

In this section, we discuss the proposed VSS-ZALMS framework for channel estimation. The energy of the observation error is utilized to adjust the step size in the VSS-based algorithms. Initially, a higher prediction error results in a larger step size, leading to a faster convergence rate. As the prediction error decreases in the (near) converged state, a smaller step size is employed, yielding lower MSE floors. Consequently, VSS-based algorithms can achieve both a higher convergence rate and lower MSE floors.

4.2.1 VSS-LMS Framework

We have taken MSE as the cost function because it is a hyperparaboloid (bowl-shaped) with a single, easily computed minimum point, as represented in [128]

$$J(k) = \mathbb{E}\{\|\mathbf{y}(k) - \mathbf{Q}^H(k)\hat{\mathbf{h}}(k)\|^2\}, \quad (4.18)$$

where $\hat{\mathbf{h}}$ is the estimate of \mathbf{h}_b . After applying the steepest-descent (SD) algorithm [100], the estimate $\hat{\mathbf{h}}(k)$ is updated as

$$\hat{\mathbf{h}}(k+1) = \hat{\mathbf{h}}(k) - \frac{\mu(k)}{2} \nabla_{\hat{\mathbf{h}}(k)}(J(k)), \quad (4.19)$$

where $\mu(k)$ is a VSS parameter. By defining covariance matrix $\mathbf{R} = \mathbb{E}\{\mathbf{Q}^H(k)\mathbf{Q}(k)\} \in \mathbb{C}^{G_{BS}G_{UE}G_I \times G_{BS}G_{UE}G_I}$ and cross covariance vector $\mathbf{p} = \mathbb{E}\{\mathbf{Q}^H(k)\mathbf{y}(k)\} \in \mathbb{C}^{G_{BS}G_{UE}G_I \times 1}$, the gradient of the MSE $J(k)$ can be represented as

$$\nabla_{\hat{\mathbf{h}}(k)}(J(k)) = 2\mathbf{R}\hat{\mathbf{h}}(k) - 2\mathbf{p}. \quad (4.20)$$

Substituting the value of $\nabla_{\hat{\mathbf{h}}(k)}(J(k))$ from (4.20) to (4.19) the recursion is given as

$$\hat{\mathbf{h}}(k+1) = \hat{\mathbf{h}}(k) + \mu(k)(\mathbf{p} - \mathbf{R}\hat{\mathbf{h}}(k)). \quad (4.21)$$

Replacing \mathbf{R} and \mathbf{p} with their instantaneous estimates, $\hat{\mathbf{R}} = \mathbf{Q}^H(k)\mathbf{Q}(k)$ and $\hat{\mathbf{p}} = \mathbf{Q}^H(k)\mathbf{y}(k)$, using the stochastic-gradient (SG) approach, the weight update recursion is given as

$$\hat{\mathbf{h}}(k+1) = \hat{\mathbf{h}}(k) + \mu(k)\mathbf{Q}^H(k)\mathbf{e}(k), \quad (4.22)$$

where $\mathbf{e}(k) \in \mathbb{C}^{N_s T \times 1}$ is the output error vector given as

$$\mathbf{e}(k) = \mathbf{y}(k) - \mathbf{Q}^H(k)\hat{\mathbf{h}}(k). \quad (4.23)$$

The step size $\mu(k)$ update equation for VSS algorithm is represented as [143],

$$\mu'(k+1) = \varphi\mu'(k) + \varrho\|\mathbf{e}(k)\|^2, \quad (4.24)$$

with $0 < \varphi < 1$, and $\varrho > 0$. Then,

$$\mu(k) = \begin{cases} \mu_{\max} & \text{if } \mu'(k+1) > \mu_{\max} \\ \mu_{\min} & \text{if } \mu'(k+1) < \mu_{\min} \\ \mu'(k+1) & \text{elseways ,} \end{cases} \quad (4.25)$$

where $0 < \mu_{\min} < \mu_{\max}$. The step size is controlled by the variables φ , ϱ , and $\mathbf{e}(k)$, as shown in (4.24). It makes intuitive sense that a larger step size in the beginning would result in faster convergence. As the estimation error decreases, the step size is reduced, leading to lower MSE and misadjustment. Bounded MSE is ensured by setting the value of μ_{\max} , and μ_{\min} is chosen to minimize misadjustments.

4.2.2 Proposed VSS-ZALMS Framework

The channel estimation problem for sparse channel vector \mathbf{h}_b is formulated as

$$\min_{\mathbf{h}_b} \|\mathbf{h}_b\|_0, \text{ subject to } \|\mathbf{y} - \mathbf{Q}\mathbf{h}_b\|_2^2 \leq \epsilon, \quad (4.26)$$

where ϵ is the error tolerance value, and $\epsilon > 0$. This is compressive sensing [138], where the task is to estimate a high-order sparse vector \mathbf{h}_b from a low-order received signal vector \mathbf{y} in a noiseless scenario. Since equation (4.26) represents a non-convex optimization problem due to the minimization of the l_0 -norm, various offline methods based on compressive sensing are available in the literature to solve it, including OMP [93] and SBL [101]. However, these approaches exhibit large computational complexity due to the involvement of multiple matrix inversions in each iteration. Consequently, existing methods require a significant amount of time for estimation, making them unsuitable for real time scenarios. This limitation is addressed in the suggested VSS-ZALMS framework, where an l_0 -norm penalty is added to the cost function of LMS approach. To handle the non-convex nature of the l_0 -norm, an appropriate approximation and l_1 -norm regularization strategy can be employed [144]. We have taken MSE as the cost function for ZALMS [102], which is given as

$$Z_L(k) = \mathbb{E} \left\{ \left\| \mathbf{y}(k) - \mathbf{Q}^H(k)\hat{\mathbf{h}}(k) \right\|^2 \right\} + \iota f(\hat{\mathbf{h}}(k)), \quad (4.27)$$

where $f(\cdot)$ is the penalty function and ι is the regularization parameter (RP). After employing the SD and VSS algorithm [100], the recursion is updated as

$$\hat{\mathbf{h}}(k+1) = \hat{\mathbf{h}}(k) - \frac{\mu(k)}{2} \nabla_{\hat{\mathbf{h}}(k)} (Z_L(k)). \quad (4.28)$$

Gradient of the MSE can be given as

$$\nabla_{\hat{\mathbf{h}}(k)} (Z_L(k)) = 2\mathbf{R}\hat{\mathbf{h}}(k) - 2\mathbf{p} - \rho(k)g\left(f\left(\hat{\mathbf{h}}(k)\right)\right), \quad (4.29)$$

where $g\left(f\left(\hat{\mathbf{h}}(k)\right)\right)$ is the gradient of the penalty term $f(\cdot)$ and $\rho(k) = \frac{\mu(k)}{2}$ denotes variable regularization step size (that controls the estimation error and degree of sparsity) and $\mu(k)$ is obtained from (4.25). Substituting the value of $\nabla_{\hat{\mathbf{h}}(k)} (Z_L(k))$ from (4.29) into (4.28), recursion for VSS-ZALMS is given as

$$\hat{\mathbf{h}}(k+1) = \hat{\mathbf{h}}(k) + \mu(k) \left(\mathbf{p} - \mathbf{R}\hat{\mathbf{h}}(k) \right) - \rho(k)g\left(f\left(\hat{\mathbf{h}}(k)\right)\right). \quad (4.30)$$

Applying SG approach, the recursion for VSS-ZALMS can be expressed as

$$\hat{\mathbf{h}}(k+1) = \hat{\mathbf{h}}(k) + \mu(k)\mathbf{Q}^H(k)\mathbf{e}(k) - \rho(k)g\left(f\left(\hat{\mathbf{h}}(k)\right)\right), \quad (4.31)$$

where $\mathbf{e}(k)$, similar to (4.23), represents the output error vector. The penalty term

Algorithm 3 Proposed VSS-ZALMS Algorithm

Input: Sensing matrix $\mathbf{Q} \in \mathbb{C}^{N_s T \times G_{BS} G_{UE} G_I}$ and received signal $\mathbf{y} \in \mathbb{C}^{N_s T \times 1}$.

Output: $\hat{\mathbf{H}}$.

- 1: **for** $m = 1, 2, \dots$, until convergence.
 - 2: $\mathbf{e}(k) = \mathbf{y}(k) - \mathbf{Q}^H(k)\hat{\mathbf{h}}(k)$.
 - 3: Recursion of channel weights is updated by (4.31).
 - 4: Update step size from (4.24).
 - 5: Find next step size from (4.25).
 - 6: Update the weight using (4.31).
 - 7: Repeat until convergence.
 - 8: **end for**
 - 9: $\hat{\mathbf{H}} = \left(\mathbf{A}_{BS}^* \otimes \mathbf{A}_{UE} \right) \text{vec}^{-1} \left(\hat{\mathbf{h}}(n) \right) \mathbf{A}_{IRS}^T$
-

$f(\cdot)$ can be l_0 and l_1 norm-based, which are explained in the next subsections.

VSS-ZALMS using l_0 -norm

The l_0 -norm penalty term, denoted as $f_0(\cdot)$, is given by

$$f_0(\hat{\mathbf{h}}(k)) = \left\| \hat{\mathbf{h}}(k) \right\|_0 = \sum_{n=1}^{G_{\text{BS}}G_{\text{UE}}G_{\text{I}}} \mathcal{I}(|\hat{\mathbf{h}}(k)| > 0), \quad (4.32)$$

where $\mathcal{I}(\cdot)$ denotes the indicator function. Since the l_0 -norm defined above is non-convex, we employ an appropriate approximation, as in [102],

$$\sum_{k=1}^{G_{\text{BS}}G_{\text{UE}}G_{\text{I}}} \mathcal{I}(|\hat{\mathbf{h}}(k)| > 0) \approx \sum_{k=1}^{G_{\text{BS}}G_{\text{UE}}G_{\text{I}}} \left(1 - e^{-\nu(|\hat{\mathbf{h}}(k)|)}\right), \quad (4.33)$$

where ν is the accuracy parameter of the approximation. Thus, the gradient term $g(f_0(\hat{\mathbf{h}}(k)))$ is given as

$$g(f_0(\hat{\mathbf{h}}(k))) = \nu e^{-\nu(|\hat{\mathbf{h}}(k)|)} \text{sgn}(\hat{\mathbf{h}}(k)). \quad (4.34)$$

Substituting the value of $g(f_0(\hat{\mathbf{h}}(k)))$ from (4.34) into (4.31), the update equation for ZA-LMS- l_0 , is obtained as

$$\hat{\mathbf{h}}(k+1) = \hat{\mathbf{h}}(k) + \mu(k)\mathbf{Q}^H(k)\mathbf{e}(k) - \rho_0(k)\nu e^{-\nu(|\hat{\mathbf{h}}(k)|)} \text{sgn}(\hat{\mathbf{h}}(k)), \quad (4.35)$$

where $\rho_0(k)$ is variable RP for ZA-LMS- l_0 .

VSS-ZALMS using l_1 -norm

The l_1 -norm penalty term is represented as $f_1(\cdot)$, is given by [102]

$$f_1(\hat{\mathbf{h}}(k)) = \left\| \hat{\mathbf{h}}(k) \right\|_1 = \sum_{n=1}^{G_{\text{BS}}G_{\text{UE}}G_{\text{I}}} |\hat{\mathbf{h}}(k)|. \quad (4.36)$$

The gradient term $g(f_1(\hat{\mathbf{h}}(k)))$ is determined by

$$g(f_1(\hat{\mathbf{h}}(k))) = \text{sgn}(\hat{\mathbf{h}}(k)). \quad (4.37)$$

The recursion for ZA-LMS- l_1 -norm is expressed as

$$\hat{\mathbf{h}}_b(k+1) = \hat{\mathbf{h}}(k) + \mu(k)\mathbf{Q}^H(k)\mathbf{e}(k) - \rho_1(k)\text{sgn}\left(\hat{\mathbf{h}}(k)\right). \quad (4.38)$$

The third term present in (4.35) and (4.38) is known as zero-attractor and its strength depends on RP.

4.3 Parameter Analysis For Performance Improvements

4.3.1 Convergence Analysis of VSS-ZALMS

Convergence analysis of VSS-ZALMS algorithms is difficult, hence the following assumptions are taken into account for tractable analysis:

Assumption 1: For the algorithms (4.31)

$$\mathbb{E}\{\mu(k)\mathbf{Q}^H(k)\mathbf{e}(k)\} = \mathbb{E}\{\mu(k)\}\mathbb{E}\{\mathbf{Q}^H(k)\mathbf{e}(k)\} \quad (4.39)$$

and

$$\mathbb{E}\left\{\rho(k)g\left(f\left(\hat{\mathbf{h}}(k)\right)\right)\right\} = \mathbb{E}\{\rho(k)\}\mathbb{E}\left\{g\left(f\left(\hat{\mathbf{h}}(k)\right)\right)\right\}. \quad (4.40)$$

By defining the weight error vector $\tilde{\mathbf{h}}(k)$ as

$$\tilde{\mathbf{h}}(k) = \mathbf{w}_b^o - \hat{\mathbf{h}}(k), \quad (4.41)$$

where \mathbf{w}_b^o is weight of optimum Wiener filter. Subtracting \mathbf{w}_b^o from both sides in equation (4.31) and then taking the expectation the recursion for VSS-ZALMS is given by

$$\begin{aligned} \mathbb{E}\{\tilde{\mathbf{h}}_b(k+1)\} &= \mathbb{E}\{\tilde{\mathbf{h}}(k)\} - \mathbb{E}\{\mu(k)\mathbf{Q}^H(k)\mathbf{Q}(k)\tilde{\mathbf{h}}(k)\} \\ &\quad + \mathbb{E}\{\mu(k)\mathbf{Q}^H(k)\mathbf{n}(k)\} - \mathbb{E}\{\rho(k)g(f(\hat{\mathbf{h}}(k)))\}. \end{aligned} \quad (4.42)$$

Employing *Assumption 1* and independent assumption of sensing matrix, noise, and weight error vector $\mathbb{E}\{\mathbf{Q}^H(k)\mathbf{n}(k)\}$ will be zero, and $\mathbb{E}\{\mathbf{Q}^H(k)\mathbf{Q}(k)\tilde{\mathbf{h}}(k)\} =$

$\mathbf{R}\mathbb{E}\{\tilde{\mathbf{h}}(k)\}$. Combining these, (4.42) can be expressed as

$$\begin{aligned}\mathbb{E}\{\tilde{\mathbf{h}}_b(k+1)\} &= (\mathbf{I} - \mathbb{E}\{\mu(k)\}\mathbf{R})\mathbb{E}\{\tilde{\mathbf{h}}(k)\} \\ &\quad - \mathbb{E}\{\rho(k)\}\mathbb{E}\{g(f(\hat{\mathbf{h}}(k)))\}.\end{aligned}\quad (4.43)$$

For l_1 -norm the gradient term $g(f(\hat{\mathbf{h}}(k))) = \rho(k)\mathbb{E}\{\text{sgn}(\hat{\mathbf{h}}(k))\}$ that is bounded between $-\rho(k)\mathbf{1}$ and $\rho(k)\mathbf{1}$. Thus, (4.43) converges if

$$\prod_{n=1}^{G_{\text{BS}}G_{\text{UE}}G_{\text{I}}} [\mathbf{I} - \mathbb{E}\{\mu(k)\}\mathbf{R}] \rightarrow \mathbf{0}_{G_{\text{BS}}G_{\text{UE}}G_{\text{I}} \times 1}, \quad \text{as } n \rightarrow \infty. \quad (4.44)$$

A sufficient condition for (4.44) to hold

$$0 < \mathbb{E}\{\mu(k)\} < \frac{2}{\text{tr}(\mathbf{R})}, \quad (4.45)$$

where $\text{tr}(\mathbf{R})$ is trace of covariance matrix \mathbf{R} .

4.3.2 Range of Regulariation Parameter ρ

Assume $\mathbf{V}(k)$ is second moment matrix of weight error vector defined as

$$\mathbf{V}(k) = \mathbb{E}\{\tilde{\mathbf{h}}(k)\tilde{\mathbf{h}}_b^H(k)\}. \quad (4.46)$$

The update equation of $\mathbf{V}(k)$ is given as

$$\begin{aligned}\mathbf{V}(k+1) &= \mathbf{V}(k) - \mathbb{E}\{\mu(k)\}(\mathbf{R}\mathbf{V}(k) + \mathbf{V}(k)\mathbf{R}) \\ &\quad + 2\mathbb{E}\{\mu^2(k)\}\mathbf{R}\mathbf{V}(k)\mathbf{R} \\ &\quad + \mathbb{E}\{\mu^2(k)\}\mathbf{R}\text{tr}\{\mathbf{R}\mathbf{V}(k)\} \\ &\quad - 2(\mathbf{I} - \mathbb{E}\{\mu(k)\}\mathbf{R})\mathbb{E}\{\rho(k)\}\mathbb{E}\{\tilde{\mathbf{h}}(k)g^H(f(\hat{\mathbf{h}}(k)))\} \\ &\quad + \mathbb{E}\{\rho^2(k)\}\mathbb{E}\{g(f(\hat{\mathbf{h}}(k)))g^H(f(\hat{\mathbf{h}}(k)))\} \\ &\quad + \mathbb{E}\{\mu^2(k)\}\sigma_n^2\mathbf{R},\end{aligned}\quad (4.47)$$

We have considered \mathbf{Q} is Gaussian with mean zero and $\mathbf{\Lambda}$ variance, then $\mathbf{R} = \mathbf{\Lambda}\mathbf{I}$, (4.47) can be simplified as

$$\begin{aligned}
\mathbf{V}(k+1) &= (1 - 2\mathbb{E}\{\mu(k)\}\mathbf{\Lambda} + 2\mathbb{E}\{\mu^2(k)\}\mathbf{\Lambda}^2)\mathbf{V}(k) + \mathbb{E}\{\mu^2(k)\}\mathbf{\Lambda}^2\text{tr}\{\mathbf{V}(k)\}\mathbf{I} \\
&\quad - 2(1 - \mathbb{E}\{\mu(k)\}\mathbf{\Lambda})\mathbb{E}\{\rho(k)\}\mathbb{E}\{\tilde{\mathbf{h}}(k)g^H(f(\hat{\mathbf{h}}(k)))\} \\
&\quad + \mathbb{E}\{\rho^2(k)\}\mathbb{E}\{g(f(\hat{\mathbf{h}}(k)))g^H(f(\hat{\mathbf{h}}(k)))\} + \mathbb{E}\{\mu^2(k)\}\sigma_n^2\mathbf{\Lambda}\mathbf{I}.
\end{aligned} \tag{4.48}$$

Let

$$U(k) = \text{tr}\{\mathbf{V}(k)\} = \mathbb{E}\{\|\hat{\mathbf{h}}(k) - \mathbf{w}_b^o\|_2^2\}. \tag{4.49}$$

Take the trace on both side of (4.49) and assume $G_{\text{BS}}G_{\text{UE}}G_{\text{I}} = G$

$$\begin{aligned}
U(k+1) &= \left[1 - 2\mathbb{E}\{\mu(k)\}\mathbf{\Lambda} + (G+2)\mathbb{E}\{\mu^2(k)\}\mathbf{\Lambda}^2\right]U(k) \\
&\quad - 2(1 - \mathbb{E}\{\mu(k)\}\mathbf{\Lambda})\mathbb{E}\{\rho(k)\}\zeta(k) + \mathbb{E}\{\rho^2(k)\}\epsilon(k) + \mathbb{E}\{\mu^2(k)\}\sigma_n^2\mathbf{\Lambda}G,
\end{aligned} \tag{4.50}$$

where

$$G = \text{tr}\{\mathbf{I}\}. \tag{4.51}$$

$$\zeta(k) = \mathbb{E}\{\tilde{\mathbf{h}}(k)g^H(f(\hat{\mathbf{h}}(k)))\}. \tag{4.52}$$

$$\epsilon(k) = \mathbb{E}\{g(f(\hat{\mathbf{h}}(k)))g^H(f(\hat{\mathbf{h}}(k)))\}. \tag{4.53}$$

Now find the bound of $\zeta(k)$ and $\epsilon(k)$

$$\begin{aligned}
|\zeta(k)| &= |\mathbb{E}\{(\hat{\mathbf{h}}(k) - \mathbf{w}_b^o)g^H(f(\hat{\mathbf{h}}(k)))\}| \\
&\leq \mathbb{E}\{|\hat{\mathbf{h}}(k) - \mathbf{w}_b^o|g^H(f(\hat{\mathbf{h}}(k)))\}| \\
&\leq \sum_{k=0}^{G-1} \mathbb{E}\{|\hat{\zeta}_{b,k}(k) - w_{b,k}^o|g^H(f(\hat{\zeta}_{b,k}(k)))\}| \\
&= \sum_{|\hat{\zeta}_{b,k}| < \frac{1}{\nu}} \mathbb{E}\{|\hat{\zeta}_{b,k}(k) - w_{b,k}^o|g^H(f(\hat{\zeta}_{b,k}(k)))\}| \\
&\leq \sum_{|\hat{\zeta}_{b,k}| < \frac{1}{\nu}} \mathbb{E}\{|\hat{\zeta}_{b,k}(k) - w_{b,k}^o|\}|g^H(f(\hat{\zeta}_{b,k}(k)))| \\
&\leq \sum_{|\hat{\zeta}_{b,k}| < \frac{1}{\nu}} \nu \mathbb{E}\{|\hat{\zeta}_{b,k}(k) - w_{b,k}^o|\} \\
&\quad (\because |g^H(f(\hat{\zeta}_{b,k}(k)))| < \nu) \\
&\leq \sum_{|\hat{\zeta}_{b,k}| < \frac{1}{\nu}} \nu \{\mathbb{E}|\hat{\zeta}_{b,k}(k)| + \|\mathbf{w}_b^o\|_1\} \\
&\leq G + \nu \|\mathbf{w}_b^o\|_1. \tag{4.54}
\end{aligned}$$

$$\begin{aligned}
|\epsilon(k)| &= |\mathbb{E}\{g(f(\hat{\mathbf{h}}(k)))g^H(f(\hat{\mathbf{h}}(k)))\}| \\
&\leq \mathbb{E}\{|g(f(\hat{\mathbf{h}}(k)))g^H(f(\hat{\mathbf{h}}(k)))|\} \\
&\leq \sum_{k=0}^{G-1} \left\{ |\hat{\zeta}_{b,k}(k)|^2 \right\} \\
&\leq G\nu^2. \tag{4.55}
\end{aligned}$$

Covariance matrix of weight-error vector can be evaluated by using (4.47) as

$$\begin{aligned}
\mathbf{V}(k+1) &= (1 - 2\mathbb{E}\{\mu(k)\}\mathbf{\Lambda} + 2\mathbb{E}\{\mu^2(k)\}\mathbf{\Lambda}^2)\mathbf{V}(k) \\
&\quad + \mathbb{E}\{\mu^2(k)\}\mathbf{\Lambda}^2 \text{tr}\{\mathbf{V}(k)\}\mathbf{I} + \mathbb{E}\{\mu^2(k)\}\sigma_n^2\mathbf{\Lambda}\mathbf{I} \\
&\quad + \mathbb{E}\{\rho^2(k)\}\mathbb{E}\{g(f(\hat{\mathbf{h}}(k)))g^H(f(\hat{\mathbf{h}}(k)))\} \\
&\quad - 2\mathbb{E}\{\rho(k)\}(1 - \mathbb{E}\{\mu(k)\}\mathbf{\Lambda})\mathbb{E}\{\tilde{\mathbf{h}}(k)g^H(f(\hat{\mathbf{h}}(k)))\}. \tag{4.56}
\end{aligned}$$

To get lower error for VSS-ZALMS- l_0 than the VSS-LMS, the fourth and the fifth term in (4.56) must be less than zero, i.e.,

$$\begin{aligned} & \{\mathbb{E}\{\rho^2(k)\}\mathbb{E}\{g(f(\hat{\mathbf{h}}(k)))g^H(f(\hat{\mathbf{h}}(k)))\} \\ & - 2\mathbb{E}\{\rho(k)\}(1 - \mathbb{E}\{\mu(k)\}\mathbf{\Lambda})\mathbb{E}\{\tilde{\mathbf{h}}(k)g^H(f(\hat{\mathbf{h}}(k)))\}\} < 0. \end{aligned} \quad (4.57)$$

By simplifying the above expression range of RP $\mathbb{E}\{\rho(k)\}$ can be given as,

$$0 < \mathbb{E}\{\rho(k)\} < \frac{2(1 - \mathbb{E}\{\mu(k)\}\mathbf{\Lambda})\mathbb{E}\{\tilde{\mathbf{h}}(k)g^H(f(\hat{\mathbf{h}}(k)))\}}{\mathbb{E}\{g(f(\hat{\mathbf{h}}(k)))g^H(f(\hat{\mathbf{h}}(k)))\}} \quad (4.58)$$

From (4.54) and (4.55), the lower and the upper bound for the RP can be given as

$$0 < \mathbb{E}\{\rho(k)\} < \frac{2(1 - \mathbb{E}\{\mu(k)\}\mathbf{\Lambda})(G + \nu\|\mathbf{h}_b^o\|_1)}{G\nu^2} \quad (4.59)$$

4.3.3 SE Analysis

SE for the system under consideration is given as

$$\text{SE} = \log_2 \left| \mathbf{I}_{N_s} + \frac{P}{N_s} \mathbf{R}_n^{-1} \mathbf{H}_{\text{eff}} \mathbf{H}_{\text{eff}}^H \right|, \quad (4.60)$$

where $\mathbf{R}_n = \sigma_n^2 \mathbf{W}_{BB}^H \mathbf{W}_{RF}^H \mathbf{W}_{RF} \mathbf{W}_{BB}$ is noise covariance matrix and

$$\mathbf{H}_{\text{eff}} = \mathbf{W}_{BB}^H \mathbf{W}_{RF}^H \mathbf{H}_{\text{IR}} \mathbf{\Theta} \mathbf{H}_{\text{TI}} \mathbf{F}_{RF} \mathbf{F}_{BB}. \quad (4.61)$$

Here \mathbf{F}_{RF} and \mathbf{F}_{BB} are RF and baseband precoders, and \mathbf{W}_{RF} and \mathbf{W}_{BB} are RF and baseband combiner, that are constructed using the singular value decomposition (SVD) of the $\hat{\mathbf{H}}$. Therefore, a more precise algorithms will result in higher SE. Asymptotic SE can be found by putting $\|\mathbf{H}_{\text{IR}}\|_F^2 = N_R M$, $\|\mathbf{H}_{\text{TI}}\|_F^2 = M N_T$, and $\|\mathbf{\Theta}\|_F^2 = M$. That can be represented as

$$\text{SE} = \log_2 \left(1 + \frac{P}{\sigma^2 N_s} N_T N_R M^2 L^2(d) \right). \quad (4.62)$$

The expression above clarifies that the SE depends on the square of the number of reflecting elements, represented as M^2 , and it encounters the challenge of dual path loss across the reflecting link. This issue of dual path loss can be overcome by deploying an active IRS.

4.3.4 Computational Complexity

Predicting the cascaded channel \mathbf{H} incurs excessively high computational complexity for OMP, SBL, and oracle LS reaching the order of $\mathcal{O}\left[(TG_1^2G_{\text{UE}}G_{\text{BS}}N_{\text{BS}})^3\right]$ due to the requirement for matrix inversion. The computational complexity of the proposed scheme can be computed as follows. Each iteration in algorithm (4.31) requires evaluation of the inner product of $\mathbf{Q}(k)\hat{\mathbf{h}}_b(k)$, where $\mathbf{Q}(k) \in \mathbb{C}^{N_s T \times G_{\text{BS}}G_{\text{UE}}G_{\text{I}}}$ and $\hat{\mathbf{h}}_b \in \mathbb{C}^{G_{\text{BS}}G_{\text{UE}}G_{\text{I}} \times 1}$, necessitating $N_s T G_{\text{BS}}G_{\text{UE}}G_{\text{I}}$ complex multiplications and $N_s T (G_{\text{BS}}G_{\text{UE}}G_{\text{I}} - 1)$ complex additions. The proposed algorithm requires evaluation of the vector $\mathbf{y}(k) - \mathbf{Q}(k)\hat{\mathbf{h}}_b(k)$, which demands $N_s T$ additions. The product $\mu(k) \left(\mathbf{y}(k) - \mathbf{Q}(k)\hat{\mathbf{h}}_b(k)\right)$ requires $N_s T$ multiplications, given that $\mu(k)$ is a real scalar. Finally, the addition of three vectors $\hat{\mathbf{h}}_b(k)$, $\mu(k) \left(\mathbf{y}(k) - \mathbf{Q}(k)\hat{\mathbf{h}}_b(k)\right)$, and $g \left(f \left(\hat{\mathbf{h}}_b(k)\right)\right)$ requires $2G_{\text{BS}}G_{\text{UE}}G_{\text{I}}$ additions. Therefore, algorithm (4.31) requires a total of $N_s T G_{\text{BS}}G_{\text{UE}}G_{\text{I}} + N_s T G_{\text{BS}}G_{\text{UE}}G_{\text{I}} + N_s T + G_{\text{BS}}G_{\text{UE}}G_{\text{I}}$ multiplications and $N_s T (G_{\text{BS}}G_{\text{UE}}G_{\text{I}} - 1) + N_s T + G_{\text{BS}}G_{\text{UE}}G_{\text{I}} (N_s T - 1) + 2G_{\text{BS}}G_{\text{UE}}G_{\text{I}}$ additions. This is considerably less as compared to the prevailing methods such as OMP, SBL, and oracle LS.

4.3.5 Training Overhead

The required training overheads for the existing methods like classical LS are $T \geq MG_{\text{UE}}$ [145], and for OMP and SBL, it is $\mathcal{O}(LL' \log(G_1^2 G_{\text{UE}} G_{\text{BS}}))$ [138]. As the recovery of a $q \times 1$ vector with p non-zero elements necessitates the dimension of the observation to be approximately $\mathcal{O}(p \log(pq))$ [138], [145], the required number of pilots for the proposed VSS-ZALMS- l_0 and VSS-ZALMS- l_1 algorithms are given by $T \geq \mathcal{O}(L' \log(L' G_{\text{UE}}) + LL' \log(LL' G_{\text{I}}))$, which is typically much smaller than the existing methods.

Table 4.1: Parameters for Simulation

Parameters	Parameters
$N_T = N_R = 32$	RF Chains: $N_{RF}^T = N_{RF}^R = 6$
Regularization Parameters: $\rho_0 = 2 \times 10^{-4}$	Regularization Parameters: $\rho_1 = 4 \times 10^{-4}$
Carrier frequency: $f_c = 28$ GHz and $T = 16$	Reference path-loss: $\beta_0 = -30$ dB
Passive reflecting elements: $M = 16 \times 8$	Multipath : $L = L' = 4$
Maximum value of step size: $\varrho_{\max} = 0.007$	Minimum value of step size: $\varrho_{\min} = 0.1^* \varrho_{\max}$
$B = 100$ MHz	$\eta = 2$, for both TI and IR link
$\nu = 15$	$G_{BS} = G_{UE} = 32$ and $G_I = 256$
G_x and $G_y = 16$	step size control parameters: $\alpha = 0.02$ and $\theta = 11$

4.3.6 IRS Deployment

The effectiveness of IRS in terms of received power at the user depends on the deployment strategy, as shown in Figure 4.3. Unlike active communication nodes, such as relays, in cooperative BS-IRS and IRS-UE channels, there is a double path-loss. Thus, the received SNR from IRS is given as [2]

$$\rho_r = \frac{P_s \beta_0^2 M^2}{(d_h^2 + H^2)((D - d_h)^2 + H^2) \sigma_n^2}, \quad (4.63)$$

where P_s denotes the power transmitted from the BS, M denotes the total reflecting units, d_h is the horizontal distance between the IRS and the user, β_0 denotes the path loss at a distance of 1 m, and σ_n^2 denotes the average received noise power. From Figure 4.3, it is evident that as d_h increases from 0 to D , the IRS-UE distance increases while the BS-IRS distance decreases. For the maximum received SNR, the denominator should be minimum, which means either $d_h = 0$ or $d_h = D$. Hence, it can be concluded that if $H \ll D$, the IRS should be placed either near the BS or the UE, and the maximum received SNR will be achieved as $\rho_r \approx \frac{P_s \beta_0^2 M^2}{(D^2 + H^2) H^2 \sigma^2}$.

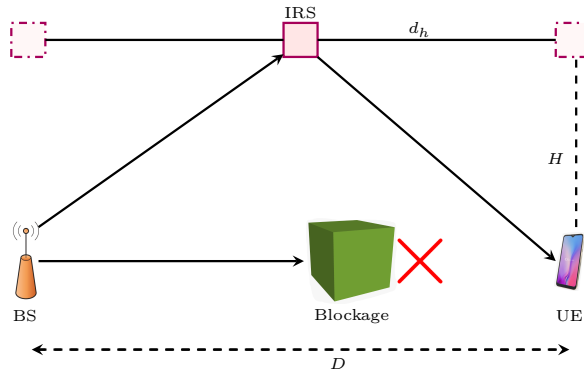


Figure 4.3: IRS installation in point-to-point communication system.

4.4 Simulation and Analytical Results

Effectiveness of the proposed approach is confirmed by the results provided in this section, and the parameters for simulation are detailed in Table 4.1. The performance metrics considered to showcase effectiveness of the overall system and the various estimator accuracy are SE and NMSE, respectively. NMSE is defined as $\mathbb{E} \left\{ \frac{\|\mathbf{H} - \hat{\mathbf{H}}\|_F^2}{\|\mathbf{H}\|_F^2} \right\}$ [138]. The NMSE and SE performance of the proposed algorithms VSS-ZALMS- l_1 and VSS-ZALMS- l_0 are compared with the existing techniques, including SBL, OMP, and the oracle LS as a benchmark estimators where it is assumed that the support of the IRS-assisted mmWave channel is completely known, although it is unknown in practice. We have considered a passive IRS-assisted mmWave hybrid MIMO system with one BS and one UE. As IRS is URA, we have fixed $M_y = 4$ and M_x increases linearly with M . For the presented scenario, the SNR for the NMSE versus iteration plot is set to 12 dB. The NMSE versus SNR plot is set in the range of 0 dB to 15 dB, while the SNR range for spectral efficiency computation is set between -60 dB to 40 dB [43]. All the presented simulation results are averaged over 300 Monte Carlo runs.

NMSE versus number of iterations

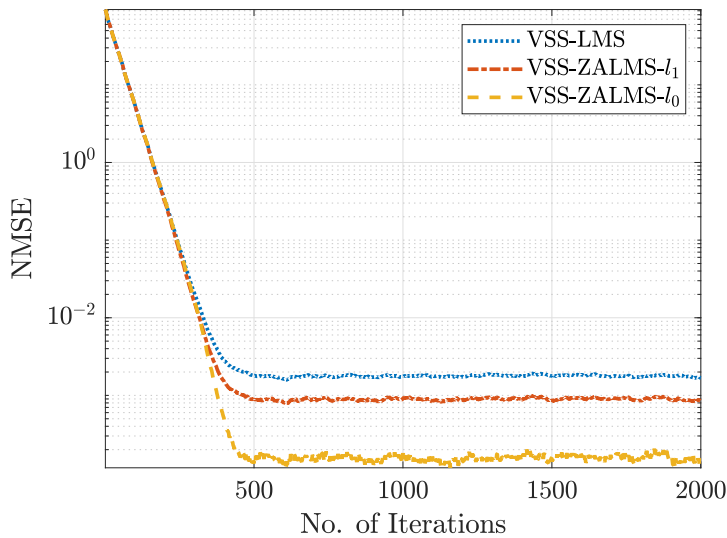


Figure 4.4: NMSE versus number of iterations performance for VSS-LMS, VSS-ZALMS- l_1 , and VSS-ZALMS- l_0 , estimators for the considered system.

It can be observed from Figure 4.4 that the proposed VSS-ZALMS-based estimator outperforms the VSS-LMS-based estimator because VSS-ZALMS methods capitalize on the inherent spatial sparsity found in the beamspace representation of the IRS-assisted mmWave hybrid MIMO channel, a feature that conventional VSS-LMS can not leverage. Further, the VSS-ZALMS- l_0 variants of VSS-ZALMS gives better NMSE performance than VSS-ZALMS- l_1 because the former is based on l_0 -norm approximation given in (4.32), which provides a better fit for the optimization objective in (4.26) than the latter.

NMSE versus SNR

Figure 4.5 illustrates the curves of NMSE versus SNR for the proposed VSS-ZALMS-based techniques after convergence, as well as for the prevailing SBL, OMP, and the benchmark oracle LS methods. From the figure, it is evident that NMSE of all approaches improves as SNR increases. Notably, the NMSE performance of the

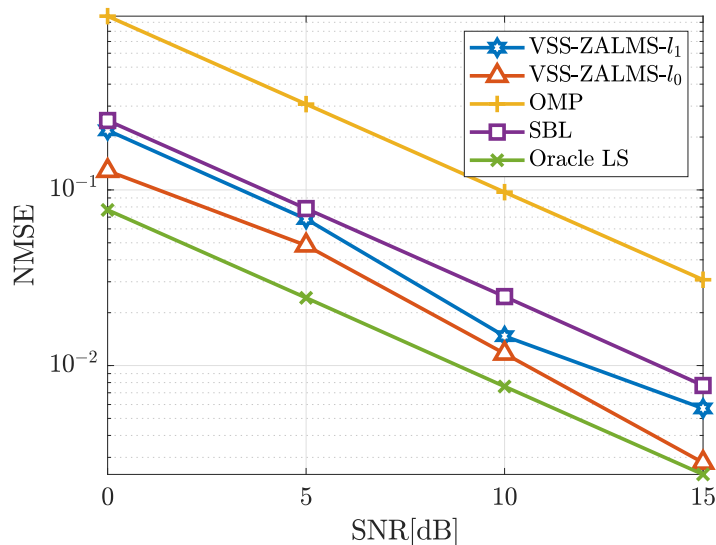


Figure 4.5: NMSE versus SNR performance of the proposed and existing estimators.

VSS-ZALMS-based techniques is approximately 7 dB better than OMP and 3 dB better than SBL, while close to performance of benchmark oracle LS scheme. Additionally, the VSS-ZALMS based scheme exhibits significantly lower complexity compared to existing methods as discussed in Section-IV-B. The Proposed method performs better than OMP because the estimation accuracy of the existing OMP scheme exhibits sensitivity to the choice of the stopping threshold. Slight deviations

in the stopping criteria contribute to the subpar performance of the OMP technique [93]. In mmWave communication, where channels can undergo rapid changes, the offline nature of the SBL leads to ineffective capturing of the sparsity pattern, ultimately resulting in poor overall performance. Conversely, the proposed VSS-ZALMS method is inherently online, meticulously assessing and adapting to variations in the mmWave channel, thereby achieving superior performance compared to SBL and OMP.

SE versus SNR

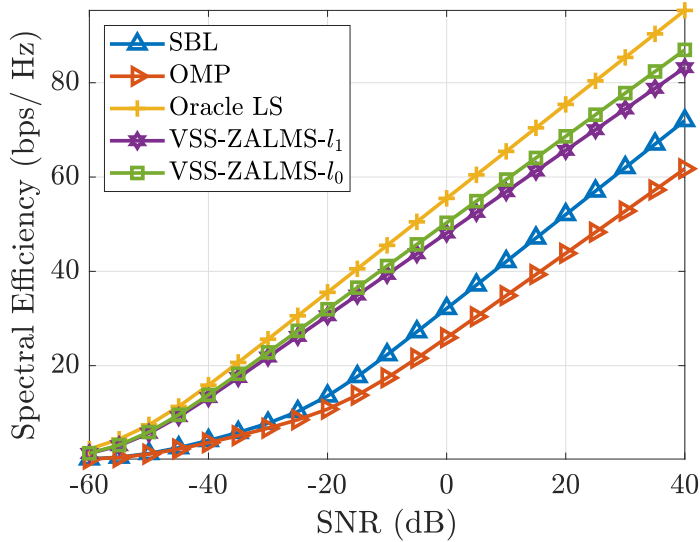


Figure 4.6: SE versus SNR performance of SBL, OMP, VSS-ZALMS, and oracle LS.

SE performance plot for various approaches are shown in Figure 4.6. The graph illustrates a noticeable pattern of improving SE with estimation accuracy. The estimator based on VSS-ZALMS demonstrates an increase of approximately 17 bits/s/Hz in SE to OMP and about 9 bits/s/Hz to the SBL estimator, especially at SNR > 0 dB, and closing to the oracle LS method. This finding affirms that VSS-ZALMS-based approach improves the net SE of the system.

SE versus reflecting elements

Figure 4.7 illustrates that the channel capacity increases with the number of reflecting elements M in the IRS. As the number of reflecting elements increases, additional strong signals are reflected by the IRS, which are used by the UE. From the plot, it

is also evident that the VSS-ZALMS-based estimator gives higher channel capacity compared to OMP and SBL for the same number of reflecting elements M due to better estimation accuracy. Hence, better channel capacity is observed compared to OMP and SBL. Additionally, these results depicts that the VSS-ZALMS-based channel estimator is more efficient in extending the communication range compared to the existing OMP and SBL estimators.

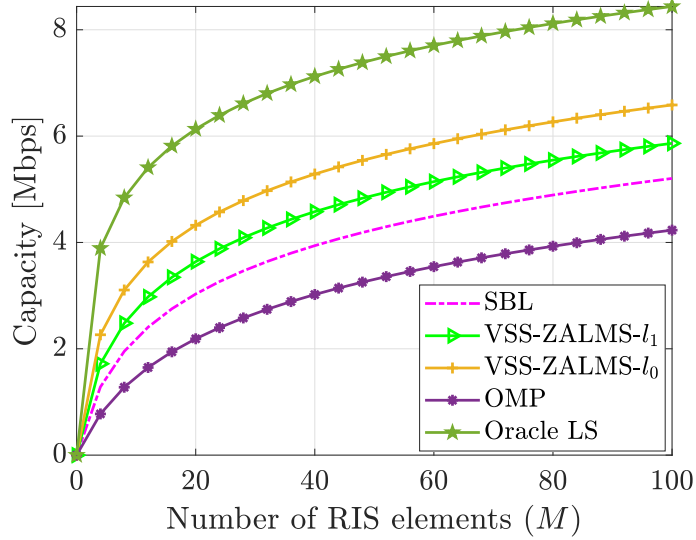


Figure 4.7: Capacity versus number of reflecting elements M performance of SBL, VSS-ZALMS- l_1 , and VSS-ZALMS- l_0 , OMP, and oracle LS estimators.

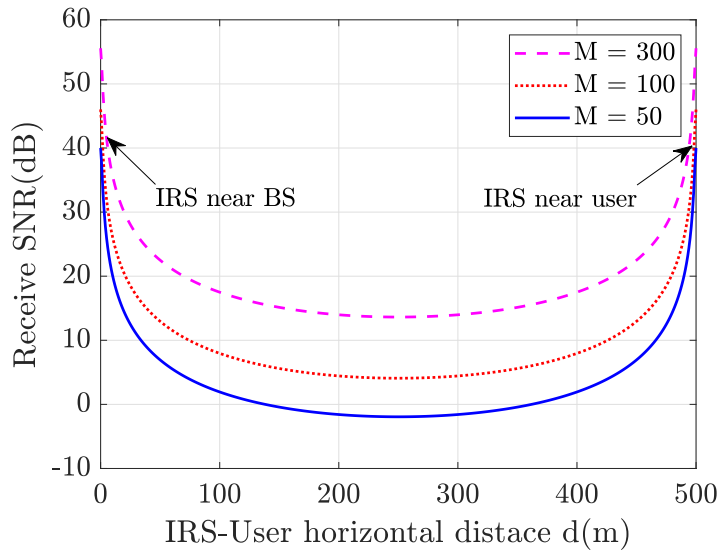


Figure 4.8: Receive SNR versus IRS-User (UE) horizontal distance d for different reflecting elements M .

Received power versus IRS-user horizontal distance

Figure 4.8 illustrates the received SNR versus IRS-UE horizontal distance plot. From the plot, the received SNR is maximum when the IRS is placed either near the BS or UE, while the SNR is minimum when the IRS is placed in the middle of the BS and UE. Thus, for maximum SNR, the IRS must be placed either close to the BS or UE terminal.

4.5 Summary

In this work, we explored the challenges of channel estimation in a mmWave hybrid MIMO system aided by IRS. A sparse recovery problem is formulated from the cascaded channel estimation problem, and VSS-ZALMS algorithm is proposed. To achieve lower NMSE and a faster convergence rate, we derive the range of regularization and step size parameters for the VSS-ZALMS-based estimator. We also analyze the computational complexity, IRS location, and SE for the considered system. Furthermore, the SE versus SNR and SE versus the number of reflecting elements' performance for several estimators are presented. Simulation results show that the proposed VSS-ZALMS-based estimator yields better estimation accuracy and higher SE performance in comparison to established approaches like OMP, SBL, and achieves performance close to the benchmark oracle LS estimator. Hence, a VSS-ZALMS-based estimator could be a potential solution for an IRS-aided mmWave hybrid MIMO system. Furthermore, to enhance the convergence rate and estimation accuracy of the proposed VSS-ZALMS-based estimator, the SEFWLMS-based estimator is proposed in the next chapter.

Chapter 5

SEFWLMS based Channel

Estimator for IRS-Aided mmWave Hybrid MIMO System

MmWave hybrid multiple-input multiple-output (MIMO) system has emerged as a potential candidate to meet the data rate demands of next-generation wireless cellular networks [91]. However, due to the limited scattering effects of mmWave signals, mmWave communication faces significant challenges. Furthermore, in typical mmWave communication systems, the quality of service (QoS) degrades dramatically when line-of-sight (LoS) links are obstructed, and the propagation environment is unknown [91].

The use of IRS in wireless communication systems is a recent breakthrough, owing to their ability to create a favorable wireless propagation environment [146]. IRSs are passive metasurfaces that can be digitally controlled to adjust the phase shifts and/or amplitudes of incident signals, allowing for energy focusing and nulling at desired locations through beamforming while consuming very little power. As a result, for mmWave communications, IRSs can reflect incident signals to establish an efficient virtual LoS link when direct LoS links between transceivers are obstructed. Furthermore, mmWave MIMO and IRS offer a wide range of practical applications, including improving cell edge coverage against blockages and enabling energy and cost efficient communication [132]. The aforementioned advantages of the IRS-aided mmWave MIMO system are possible only when accurate channel estimates

are available, which is challenging due to the limited signal processing capability in passive reflecting elements and the large number of reflecting elements causes high channel estimation overhead [147, 148].

Several studies have recently investigated channel prediction in IRS-assisted wireless communication system. In [149], a low-complexity two-time-scale method for pilot overhead reduction based techniques is proposed. In [150], a MMSE based method is proposed to estimate the aggregated channel in IRS-assisted massive MIMO systems. However, in both works, the mmWave system is not considered. Since the mmWave channel is sparse, popular CS techniques, such as the generalized approximation message passing (GAMP) and OMP algorithms, can be readily applied to IRS-assisted mmWave MIMO systems for channel estimation [138]. However, the computational complexity of these techniques increases cubically with the number of antennas and reflecting elements [138].

Hence, in this chapter, an adaptive filtering framework to solve the CS reconstruction problem is proposed, which can be viewed as a sparse channel estimation problem. At lower complexity, we introduce the l_0 -variant of the exponential forgetting window least mean square (EFWLMS) algorithm for sparse channel identification, termed as the sparse EFWLMS (SEFWLMS) adaptive algorithm. The proposed technique offers lower computational complexity and storage, resulting in higher estimation speed (i.e., lower latency) since no matrix inversion is involved in the composite channel estimation. SEFWLMS-based estimators provide improved accuracy, lower computational complexity, and storage compared to existing methods, such as SBL and OMP.

From this perspective, the major contributions of this work are:

- SEFWLMS-based channel estimator is proposed for the cascaded channel between the BS-IRS-UE in IRS-assisted mmWave hybrid MIMO channels, formulated using Kronecker products.
- For the considered system, a sparse channel estimation model is developed in the beamspace domain. This model includes a sparsifying dictionary composed of quantized receive and transmit array response vectors.
- The proposed method is applicable for both stationary and nonstationary con-

ditions in IRS-aided mmWave hybrid MIMO systems, emphasizing its versatility and practical importance.

- Performance of the proposed channel estimator is compared with the existing methods e.g. OMP and SBL and also for oracle LS for benchmarking purpose. Simulation results corroborate the superiority of the suggested estimator in terms of accuracy, complexity, and robustness compared to existing estimators.

5.1 System and Channel Model

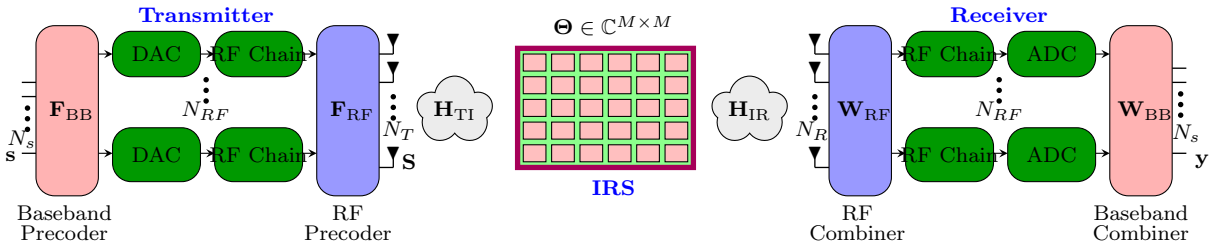


Figure 5.1: Diagram illustrating the channel estimation for an IRS-assisted mmWave hybrid MIMO transceiver.

In this work, a downlink system is considered, in which a signal is transmitted from the base station (BS) with N_T transmit antennas (TAs) to the user equipment (UE) with N_R receive antennas (RAs) via an IRS. Suppose N_{RF}^T and N_{RF}^R are the numbers of RF chains at the BS and the UE, respectively, to transmit N_s data streams, where $N_s \leq \min(N_{RF}^T, N_{RF}^R) \ll \min(N_T, N_R)$. The considered IRS is a URA with M low-cost passive reflecting elements that only reflect the signals once. The IRS provides a virtual LoS link for the UE, which is unable to communicate directly through LoS with the BS due to deep path loss or obstructions. A smart controller that receives input from the BS over a backhaul link [151] can alter IRS reflecting components' phase shifts.

Let $\mathbf{H}_{TI} \in \mathbb{C}^{M \times N_T}$ represent the channel between the BS and the IRS, and $\mathbf{H}_{IR} \in \mathbb{C}^{N_R \times M}$ represent the channel between the IRS and the UE. Due to adverse propagation conditions, the LoS path between the BS and the UE is neglected. Using mmWave channel reciprocity [141], time-division duplexing (TDD) is suggested for acquiring channel state information (CSI). In this work, we consider a block-faded

quasi-static channel with a coherence time of T , i.e., the channel does not change within each transmission block of length T .

The transmitted signal from the BS, \mathbf{x} in the t^{th} time frame, can be given as $\mathbf{x} = \mathbf{F}_{RF}\mathbf{F}_{BB}\mathbf{s} = \mathbf{F}\mathbf{s}$ where $\mathbf{s} \in \mathbb{C}^{N_s \times 1}$ is the transmitted signal vector with a covariance matrix $\mathbb{E}\{\mathbf{s}\mathbf{s}^H\} = \frac{P_s}{N_s}\mathbf{I}_{N_s}$, $\mathbf{F} = \mathbf{F}_{RF}\mathbf{F}_{BB} \in \mathbb{C}^{N_T \times N_s}$ is the hybrid precoding matrix at the BS cascaded with the RF precoder $\mathbf{F}_{RF} \in \mathbb{C}^{N_{RF}^T \times N_T}$ and the baseband precoder $\mathbf{F}_{BB} \in \mathbb{C}^{N_s \times N_{RF}^T}$. The post-processed received signal $\mathbf{y} \in \mathbb{C}^{N_s \times 1}$ at the UE side can be given as $\mathbf{y} = \mathbf{W}^H\mathbf{H}\mathbf{x} + \tilde{\mathbf{n}}$, where $\tilde{\mathbf{n}} = \mathbf{W}^H\mathbf{n}$, \mathbf{n} represents AWGN noise with distribution $\mathcal{CN}(\mathbf{0}, \sigma_n^2\mathbf{I}_{N_R})$, and $\mathbf{W} \in \mathbb{C}^{N_R \times N_s}$ is the hybrid combiner, which is cascaded with the RF combiner $\mathbf{W}_{RF} \in \mathbb{C}^{N_R \times N_{RF}^R}$ and baseband combiner $\mathbf{W}_{BB} \in \mathbb{C}^{N_{RF}^R \times N_s}$. The combined channel matrix $\mathbf{H} \in \mathbb{C}^{N_R \times N_T}$ between the BS-IRS-UE is presented as

$$\mathbf{H} = \mathbf{H}_{IR}\mathbf{\Theta}\mathbf{H}_{TI} \quad (5.1)$$

where $\mathbf{\Theta} \in \mathbb{C}^{M \times M}$ is a diagonal matrix that generates the phase shifts induced by the reflecting components of the IRS, given by $\mathbf{\Theta} = \text{diag}\{\kappa_1 e^{j\theta_1}, \dots, \kappa_M e^{j\theta_M}\}$, with $\kappa_m \in [0, 1]$, $\theta_m \in [0, 2\pi)$, for $m = 1, \dots, M$ is the m^{th} amplitude reflection and phase shift of reflecting element, respectively. Without loss of generality, we consider the same κ_m for all of the IRS's reflecting parts. For the T time frames, the observed signal matrix at the UE can be stated as follows

$$\mathbf{Y} = \mathbf{W}^H\mathbf{H}\mathbf{X} + \tilde{\mathbf{N}}, \quad (5.2)$$

where \mathbf{X} is $N_T \times T$ beamforming matrix, \mathbf{Y} is $N_s \times T$ matrix of observed signal, and $\tilde{\mathbf{N}}$ is $N_s \times T$ noise matrix.

5.1.1 IRS-Aided mmWave MIMO Channel Model

We consider a downlink propagation scenario and geometric channel model for propagation environment. In this model channel matrices between the BS-IRS and the IRS-UE are characterized [138] as,

$$\mathbf{H}_{TI} = \sqrt{\frac{N_T M}{\eta_T}} \sum_{l=1}^L \alpha_l \mathbf{a}_{IRS}(\psi_l, \gamma_l) \mathbf{a}_{BS}^H(\phi_l), \quad (5.3)$$

$$\mathbf{H}_{\text{IR}} = \sqrt{\frac{N_R M}{\eta_R}} \sum_{l'=1}^{L'} \beta_{l'} \mathbf{a}_{\text{UE}}(\phi_{l'}) \mathbf{a}_{\text{IRS}}^H(\psi_{l'}, \gamma_{l'}), \quad (5.4)$$

η_T represents the path loss between the BS-IRS, while α_l stands for the complex path gain of the l^{th} path. The variable L refers to the scattering path of the BS-IRS link. $\psi_l(\gamma_l)$ denotes the azimuth (elevation) AoA for the l^{th} path, and ϕ_l signifies the AoD of the l^{th} path in the BS-IRS link. Similarly, in the context of the IRS-UE channel, η_R pertains to path loss, $\beta_{l'}$ represents the complex path gain, $\psi_{l'}(\gamma_{l'})$ is associated with azimuth (elevation) AoD, and $\phi_{l'}$ corresponds to AoA for the l^{th} path. Furthermore, \mathbf{a}_{BS} , \mathbf{a}_{IRS} , and \mathbf{a}_{UE} are the array response vectors (ARV) for the BS, IRS, and UE, respectively, and can be defined as follows

$$\mathbf{a}_{\text{BS}}(\phi_l) = \frac{1}{\sqrt{N_T}} \left[1, e^{\frac{j2\pi d \cos(\phi_l)}{\lambda}}, \dots, e^{\frac{j2\pi d(N_T-1) \cos(\phi_l)}{\lambda}} \right]^T, \quad (5.5)$$

$$\mathbf{a}_{\text{UE}}(\phi_{l'}) = \frac{1}{\sqrt{N_R}} \left[1, e^{\frac{j2\pi d \cos(\phi_{l'})}{\lambda}}, \dots, e^{\frac{j2\pi d(N_R-1) \cos(\phi_{l'})}{\lambda}} \right]^T, \quad (5.6)$$

where $d = \lambda/2$, is consecutive antenna spacing and λ is the wavelength of the carrier signal. In this work, the IRS is taken as $M_x \times M_y$ URA of $M \triangleq M_x M_y$ elements [138]. The ARV of IRS is given as $\mathbf{a}_{\text{IRS}}(\psi_l, \gamma_l) = \mathbf{a}_x(\psi_l, \gamma_l) \otimes \mathbf{a}_y(\gamma_l)$. The term $\mathbf{a}_x(\psi_l, \gamma_l)$ and $\mathbf{a}_y(\gamma_l)$ can be expressed as

$$\mathbf{a}_x(\psi_l, \gamma_l) = \frac{1}{\sqrt{M_x}} \left[1, e^{\frac{j2\pi d_r \sin(\gamma_l) \cos(\psi_l)}{\lambda}}, \dots, e^{\frac{j2\pi d_r(M_x-1) \sin(\gamma_l) \cos(\psi_l)}{\lambda}} \right]^T, \quad (5.7)$$

$$\mathbf{a}_y(\gamma_l) = \frac{1}{\sqrt{M_y}} \left[1, e^{\frac{j2\pi d_r \cos(\gamma_l)}{\lambda}}, \dots, e^{\frac{j2\pi d_r(M_y-1) \cos(\gamma_l)}{\lambda}} \right]^T, \quad (5.8)$$

where d_r is the consecutive reflecting elements spacing.

5.1.2 Sparse Representation of IRS-Aided mmWave Channel

The BS-IRS and IRS-UE channel matrices can be rewritten in beamspace domain as follows

$$\mathbf{H}_{\text{TI}} = \mathbf{A}_{\text{IRS}} \mathbf{\Lambda}_\alpha \mathbf{A}_{\text{BS}}^H, \quad \mathbf{H}_{\text{IR}} = \mathbf{A}_{\text{UE}} \mathbf{\Lambda}_\beta \mathbf{A}_{\text{IRS}}^H, \quad (5.9)$$

where $\mathbf{A}_{\text{BS}} \in \mathbb{C}^{N_T \times G_{\text{BS}}}$, $\mathbf{A}_{\text{IRS}} \in \mathbb{C}^{M \times G_I}$, and $\mathbf{A}_{\text{UE}} \in \mathbb{C}^{N_R \times G_{\text{UE}}}$ are three angular domain overcomplete dictionary matrices made up of ARVs, each of which relates to a particular AoA/AoD at the BS, IRS, and UE, respectively. G_{BS} , G_I , and G_{UE} represent the corresponding angular resolutions. $\mathbf{\Lambda}_\alpha \in \mathbb{C}^{G_I \times G_{\text{BS}}}$ and $\mathbf{\Lambda}_\beta \in \mathbb{C}^{G_{\text{UE}} \times G_I}$ are two sparse matrices with L and L' number of path and their gain elements that are non-zero α_l and $\beta_{l'}$, respectively. The dictionary matrices \mathbf{A}_{BS} and \mathbf{A}_{UE} can be given as $\mathbf{A}_{\text{BS}} = [\mathbf{a}_{\text{BS}}(\phi_1), \dots, \mathbf{a}_{\text{BS}}(\phi_{G_{\text{BS}}})]$ and $\mathbf{A}_{\text{UE}} = [\mathbf{a}_{\text{UE}}(\phi_1), \dots, \mathbf{a}_{\text{UE}}(\phi_{G_{\text{UE}}})]$, respectively. Similarly, the dictionary matrix \mathbf{A}_{IRS} is defined as $\mathbf{A}_{\text{IRS}} = \mathbf{A}_x \otimes \mathbf{A}_y$, where $\mathbf{A}_x = [\mathbf{a}_x(\psi_1, \gamma_1), \dots, \mathbf{a}_x(\psi_{G_x}, \gamma_{G_x})]$ and $\mathbf{A}_y = [\mathbf{a}_y(\gamma_1), \dots, \mathbf{a}_y(\gamma_{G_y})]$. Here, G_x and G_y denote the angular resolutions along the x -axis and y -axis, respectively, such that $G_I = G_x G_y$.

5.2 Problem Formulation

Substituting the value of \mathbf{H}_{TI} and \mathbf{H}_{IR} from (5.9) into (5.1), and vectorizing the cascade channel as

$$\begin{aligned}
 \text{vec}(\mathbf{H}) &= \text{vec}(\mathbf{A}_{\text{UE}} \mathbf{\Lambda}_\beta \mathbf{A}_{\text{IRS}}^H \mathbf{\Theta} \mathbf{A}_{\text{IRS}} \mathbf{\Lambda}_\alpha \mathbf{A}_{\text{BS}}^H) \\
 &\stackrel{\text{(a)}}{=} (\mathbf{A}_{\text{BS}}^* \otimes \mathbf{A}_{\text{UE}}) \text{vec}(\mathbf{\Lambda}_\beta \mathbf{A}_{\text{IRS}}^H \mathbf{\Theta} \mathbf{A}_{\text{IRS}} \mathbf{\Lambda}_\alpha) \\
 &\stackrel{\text{(b)}}{=} (\mathbf{A}_{\text{BS}}^* \otimes \mathbf{A}_{\text{UE}}) (\mathbf{\Lambda}_\alpha^T \otimes \mathbf{\Lambda}_\beta) (\mathbf{A}_{\text{IRS}}^T \odot \mathbf{A}_{\text{IRS}}^H) \text{vecd}(\mathbf{\Theta}) \\
 &\stackrel{\text{(c)}}{=} (\mathbf{A}_{\text{BS}}^* \otimes \mathbf{A}_{\text{UE}}) (\mathbf{\Lambda}_\alpha^T \otimes \mathbf{\Lambda}_\beta) \mathbf{A}_{\text{D}} \mathbf{z}, \tag{5.10}
 \end{aligned}$$

where (a) and (b) is from vectorization of the matrix product, and (c) is obtained by substituting $\mathbf{A}_{\text{D}} = (\mathbf{A}_{\text{IRS}}^T \odot \mathbf{A}_{\text{IRS}}^H) \in \mathbb{C}^{G_I^2 \times M}$ and $\mathbf{z} = \text{vecd}(\mathbf{\Theta}) \in \mathbb{C}^{M \times 1}$, where $\text{vecd}(\mathbf{\Theta})$ is M -dimensional vector consisting of diagonal entries of $\mathbf{\Theta}$. With the channel model as in (5.10), the received signal vector can be given as,

$$\begin{aligned}
 \mathbf{y} &= (\mathbf{X}^T \otimes \mathbf{W}^H) \text{vec}(\mathbf{H}) + \text{vec}(\tilde{\mathbf{N}}) \\
 &\stackrel{\text{(a)}}{=} (\mathbf{X}^T \otimes \mathbf{W}^H) (\mathbf{A}_{\text{BS}}^* \otimes \mathbf{A}_{\text{UE}}) (\mathbf{\Lambda}_\alpha^T \otimes \mathbf{\Lambda}_\beta) \mathbf{A}_{\text{D}} \mathbf{z} + \tilde{\mathbf{n}}. \tag{5.11}
 \end{aligned}$$

Based on formulation of the overcomplete matrix \mathbf{A}_{IRS} , we have the $\mathbf{A}_{\text{IRS}}^T \circ (\mathbf{a}_k^H \otimes \mathbf{1}_{G_I}) = \mathbf{P}_k \mathbf{A}_{\text{IRS}}^T$, where $\mathbf{a}_k \in \mathbb{C}^{M \times 1}$ denotes the k^{th} column of \mathbf{A}_{IRS} and $\mathbf{P}_k \in \mathbb{C}^{G_I \times G_I}$

is a permutation matrix that changes the order of the rows of \mathbf{A}_{IRS} . Hence, the term $(\mathbf{\Lambda}_\alpha^T \otimes \mathbf{\Lambda}_\beta) (\mathbf{A}_{\text{IRS}}^T \odot \mathbf{A}_{\text{IRS}}^H)$ in (5.11) can be simplified as follows

$$(\mathbf{\Lambda}_\alpha^T \otimes \mathbf{\Lambda}_\beta) (\mathbf{A}_{\text{IRS}}^T \odot \mathbf{A}_{\text{IRS}}^H) = \underbrace{\left(\sum_{k=1}^{G_I} (\mathbf{\Lambda}_k \otimes \mathbf{\Lambda}_\beta) \mathbf{P}_k \right)}_{\hat{\mathbf{\Lambda}}} \mathbf{A}_{\text{IRS}}^T, \quad (5.12)$$

where $\mathbf{\Lambda}_k \in \mathbb{C}^{G_{\text{BS}} \times 1}$ denotes the k^{th} column of $\mathbf{\Lambda}_\alpha^T$ and $\hat{\mathbf{\Lambda}} \in \mathbb{C}^{G_{\text{BS}} G_{\text{UE}} \times G_I}$ is sparse matrix with LL' non-zero elements. Finally, putting the results of (5.12) into (5.11), we have

$$\begin{aligned} \mathbf{y} &= (\mathbf{X}^T \otimes \mathbf{W}^H) (\mathbf{A}_{\text{BS}}^* \otimes \mathbf{A}_{\text{UE}}) \hat{\mathbf{\Lambda}} \mathbf{A}_{\text{IRS}}^T \mathbf{z} + \tilde{\mathbf{n}} \\ &\stackrel{(a)}{=} ((\mathbf{z}^T \mathbf{A}_{\text{IRS}}) \otimes ((\mathbf{X}^T \otimes \mathbf{W}^H) (\mathbf{A}_{\text{BS}}^* \otimes \mathbf{A}_{\text{UE}}))) \mathbf{h}_b + \tilde{\mathbf{n}} \\ &\stackrel{(b)}{=} \mathbf{Q} \mathbf{h}_b + \tilde{\mathbf{n}}, \end{aligned} \quad (5.13)$$

where $\mathbf{h}_b = \text{vec}(\hat{\mathbf{\Lambda}}) \in \mathbb{C}^{G_{\text{BS}} G_{\text{UE}} G_I \times 1}$ is sparse vector with LL' non-zero elements and $\tilde{\mathbf{n}} = \text{vec}(\tilde{\mathbf{N}})$. Equation (b) is obtained by substituting

$$\mathbf{Q} \triangleq ((\mathbf{z}^T \mathbf{A}_{\text{IRS}}) \otimes ((\mathbf{X}^T \otimes \mathbf{W}^H) (\mathbf{A}_{\text{BS}}^* \otimes \mathbf{A}_{\text{UE}}))) \in \mathbb{C}^{N_s T \times G_{\text{BS}} G_{\text{UE}} G_I}$$

that is sensing matrix. To reduce the computational complexity and improve performance, we propose SEFWLMS based adaptive filtering approach to estimate the combined sparse vector \mathbf{h}_b . Finally, the estimated cascaded channel $\hat{\mathbf{H}}$ is given as $\hat{\mathbf{H}} = (\mathbf{A}_{\text{BS}}^* \otimes \mathbf{A}_{\text{UE}}) \mathbf{H}_b \mathbf{A}_{\text{IRS}}^T$, where \mathbf{H}_b is formed by reshaping \mathbf{h}_b to a $LL' \times G_I$ matrix using $\text{vec}^{-1}(\mathbf{h}_b)$.

5.3 SEFWLMS Framework

The considered channel estimation problem for sparse vector \mathbf{h}_b can be formulated as

$$\min_{\mathbf{h}_b} \|\mathbf{h}_b\|_0, \quad \text{subject to } \|\mathbf{y} - \mathbf{Q} \mathbf{h}_b\|_2^2 \leq \epsilon, \quad (5.14)$$

where the error tolerance value $\epsilon > 0$. The above optimization problem is non-convex due to the minimization of l_0 -norm. According to the CS theory, we can correctly recover a large-dimensional sparse vector \mathbf{h}_b from a considerably smaller dimensional linear measurement vector \mathbf{y} in the noiseless scenario. The literature contains a variety of offline techniques for recovering sparse signals, including OMP [93] and SBL [101]. However, these algorithms have a substantial high computation and storage cost due to multiple matrix inversion in each iterations. Moreover, *offline* processing, also leads to lower estimation speed (i.e. higher latency) and high algorithmic delay, which is not suitable for real time applications. These problems are addressed in the proposed SEFWLMS framework. Recent research [152] on CS demonstrates that sparsity is best represented by the l_0 -norm in which the sparsest solution is acquired. This implies that when the unknown parameters are sparse, a l_0 -norm penalty on the adaptive filter coefficients can be integrated into the cost function which ensure sparsity of the solution.

5.3.1 SEFWLMS Framework

Recursive least square (RLS) algorithm [153] is a classical adaptive algorithm where the cost function is defined as

$$\xi_{\text{RLS}}(k) = \sum_{l=1}^k \Lambda^{k-l} |e(l)|^2, \quad (5.15)$$

where $0 \ll \Lambda < 1$ is the forgetting factor, and $e(l) = d(l) - \mathbf{r}(l)\hat{\mathbf{h}}(k)$ is the observation error, $\hat{\mathbf{h}}(k)$ is the estimated value of \mathbf{h}_b at instant n , and $\mathbf{r}(l)$ is row vector found from the sensing matrix $\mathbf{Q}(l, :)$. Above algorithm is difficult to implement due to high computation resources requirements of RLS. However, RLS motivates the consideration of approximating its cost function with a shorter sliding window, meaning a new penalty, which is stated as

$$\xi_{\text{EFWLMS}}(k) = \sum_{l=k-\hat{W}+1}^k \Lambda^{k-l} |e(l)|^2, \quad (5.16)$$

where \hat{W} is the sliding window length. The algorithm, which minimizes (5.16), is known as EFWLMS. The gradient descent weight update equation of filter coefficient

vector is given as

$$\hat{\mathbf{h}}(k+1) = \hat{\mathbf{h}}(k) + \mu \mathbf{R}(k) \mathbf{A} \mathbf{e}'(k), \quad (5.17)$$

where μ is step size parameter,

$$\mathbf{A} = \begin{bmatrix} \Lambda^{\hat{W}-1} & 0 & \cdots & 0 \\ 0 & \Lambda^{\hat{W}-2} & \cdots & 0 \\ \vdots & \vdots & \ddots & \vdots \\ 0 & 0 & \cdots & 1 \end{bmatrix} \quad (5.18)$$

$$\mathbf{R}(k) = \left[\mathbf{r}(k - \hat{W} + 1), \mathbf{r}(k - \hat{W} + 2), \dots, \mathbf{r}(k) \right],$$

$$\begin{aligned} \mathbf{e}'(k) &= \left[e(k - \hat{W} + 1), e(k - \hat{W} + 2), \dots, e(k) \right]^T, \\ &= \mathbf{d}'(k) - \mathbf{R}(k) \hat{\mathbf{h}}(k), \end{aligned} \quad (5.19)$$

and $\mathbf{d}'(k) = \left[d(k - \hat{W} + 1), d(k - \hat{W} + 2), \dots, d(k) \right]$. Employing zero attraction for sparse solutions the final gradient descent weight-update expression of the filter coefficient vector is given as

$$\hat{\mathbf{h}}(k+1) = \hat{\mathbf{h}}(k) + \mu \mathbf{R}(k) \mathbf{A} \mathbf{e}'(k) + \kappa g \left(f \left(\hat{\mathbf{h}}(k) \right) \right), \quad (5.20)$$

where $g \left(f \left(\hat{\mathbf{h}}(k) \right) \right) = \nabla_{\hat{\mathbf{h}}(k)} g \left(f \left(\hat{\mathbf{h}}(k) \right) \right)$ is the gradient of sparsity inducing penalty function $f(\cdot)$ and κ is regularization parameter that balance the degree of sparsity and the estimation error. We have considered the l_0 -norm penalty function that is represented by $f_0(\cdot)$ and given as

$$f_0 \left(\hat{\mathbf{h}}(k) \right) = \left\| \hat{\mathbf{h}}(k) \right\|_0 = \sum_{n=1}^{G_{\text{BS}} G_{\text{UE}} G_{\text{I}}} \mathcal{I} \left(\left| \hat{\mathbf{h}}(k) \right| > 0 \right), \quad (5.21)$$

where $\mathcal{I}(\cdot)$ represents the indicator function. Since, the l_0 -norm mentioned above is non-convex, hence, an appropriate approximation is used as in [154],

$$\sum_{k=1}^{G_{\text{BS}} G_{\text{UE}} G_{\text{I}}} \mathcal{I} \left(\left| \hat{\mathbf{h}}(k) \right| > 0 \right) \approx \sum_{k=1}^{G_{\text{BS}} G_{\text{UE}} G_{\text{I}}} \left(1 - e^{-\nu \left(\left| \hat{\mathbf{h}}(k) \right| \right)} \right) \quad (5.22)$$

where ν is the accuracy term. Thus, the gradient term $g\left(f_0\left(\hat{\mathbf{h}}(k)\right)\right)$ is given as

$$g\left(f_0\left(\hat{\mathbf{h}}(k)\right)\right) = \nu e^{-\nu(|\hat{\mathbf{h}}(k)|)} \text{sgn}\left(\hat{\mathbf{h}}(k)\right). \quad (5.23)$$

Substituting the value of $g\left(f_0\left(\hat{\mathbf{h}}(k)\right)\right)$ into (5.20), the final recursion of the filter coefficient is

$$\hat{\mathbf{h}}(k+1) = \hat{\mathbf{h}}(k) + \mu \mathbf{R}(k) \mathbf{A} \mathbf{e}'(k) - \rho_0 \nu e^{-\nu(|\hat{\mathbf{h}}(k)|)} \text{sgn}\left(\hat{\mathbf{h}}(k)\right), \quad (5.24)$$

where $\rho_0 = \mu\kappa$ is regularization step size and $\text{sgn}(\cdot)$ is sign function. Above algorithm is l_0 -variants of EFWLMS known as SEFWLMS algorithm. The third term, $-\rho_0 \nu e^{-\nu(|\hat{\mathbf{h}}(k)|)} \text{sgn}\left(\hat{\mathbf{h}}(k)\right)$, of SEFWLMS algorithm is known as *zero attraction* term, which forces the small coefficient attracted to zero, that causes SEFWLMS to achieve faster convergence.

Algorithm 4 Proposed SEFWLMS Algorithm

Initialize: $\hat{\mathbf{h}}(0) = \mathbf{0}_{G_{\text{R}}G_{\text{T}} \times 1}$, **Choose:** $\hat{W}, \mu, \alpha, \rho_0, \Lambda$.

Output: $\hat{\mathbf{H}}$.

- 1: **while** $\|\hat{\mathbf{h}}(k) - \hat{\mathbf{h}}(k-1)\|_2 < \zeta$ or $n > \text{Max-iteration}$.
 - 2: Find \hat{W} input vector and \hat{W} desired vector.
 - 3: **For** $l = k - \hat{W} + 1, \dots, k$.
 - 4: $i = \text{mod}(l, N_s T) + 1$, mod : modulo operation.
 - 5: $\mathbf{r}(l) = \mathbf{Q}(i, :)$
 - 6: $d(l) = y_i$, where y_i is the i^{th} element of \mathbf{y}
 - 7: **End For**
 - 8: Find $\mathbf{e}'(k)$ using (5.19)
 - 9: Update $\hat{\mathbf{h}}(k)$ using (5.24).
 - 10: Increase iteration number by one i.e., $k = k + 1$.
 - 11: **End while**
 - 12: $\hat{\mathbf{H}} = \left(\mathbf{A}_{\text{BS}}^* \otimes \mathbf{A}_{\text{UE}}\right) \text{vec}^{-1}\left(\hat{\mathbf{h}}(k)\right) \mathbf{A}_{\text{IRS}}^T$
-

5.3.2 Complexity Analysis

To estimate the cascaded channel \mathbf{H} , the complexity order for OMP, SBL, and oracle LS are prohibitively high that is in the order of $\mathcal{O}[(TG_{\text{I}}^2 G_{\text{UE}} G_{\text{BS}} N_{\text{BS}})^3]$ due to the need for matrix inversion. For the proposed SEFWLMS scheme, the complexity order is $\mathcal{O}[(2\hat{W} + 1)TG_{\text{I}}^2 G_{\text{UE}} G_{\text{BS}} N_{\text{BS}}]$, which is significantly lower than the existing methods OMP, SBL, and oracle LS.

5.3.3 Spectral Efficiency

The SE for the IRS-aided mmWave MIMO is defined as

$$\text{SE} = \log_2 \left| \mathbf{I}_{N_s} + \frac{P_s}{N_s} \mathbf{R}_n^{-1} \mathbf{H}_{\text{eff}} \mathbf{H}_{\text{eff}}^H \right|, \quad (5.25)$$

where $\mathbf{R}_n = \sigma_n^2 \mathbf{W}_{BB}^H \mathbf{W}_{RF}^H \mathbf{W}_{RF} \mathbf{W}_{BB}$ is noise covariance matrix and

$$\mathbf{H}_{\text{eff}} = \mathbf{W}_{BB}^H \mathbf{W}_{RF}^H \mathbf{H}_{\text{IR}} \mathbf{\Theta} \mathbf{H}_{\text{TI}} \mathbf{F}_{RF} \mathbf{F}_{BB}.$$

Here \mathbf{F}_{RF} and \mathbf{F}_{BB} are optimal precoders, and \mathbf{W}_{RF} and \mathbf{W}_{BB} are the optimal combiners, that are designed via the SVD of the estimated channel $\hat{\mathbf{H}}$. Hence, accurate estimator will give higher spectral efficiency. By substituting $\|\mathbf{H}_{\text{IR}}\|_F^2 = N_R M$, $\|\mathbf{H}_{\text{TI}}\|_F^2 = M N_T$, and $\|\mathbf{\Theta}\|_F^2 = 1$ we can find asymptotic SE as

$$\text{SE} = \log_2 \left(1 + \frac{P_s}{\sigma^2 N_s} N_T N_R M^2 L^2(d) \right). \quad (5.26)$$

From the above expression, it is clear that the SNR gain in an IRS-aided system increases with the square of M and also suffers from double path loss over the reflecting link. Due to this double path loss, the received signal at the downlink is very weak, on the order of -140 dB [155]. To improve the received signal strength, an active IRS with a moderate number of reflecting elements would be a better choice. An active IRS can use a small amount of power to amplify the signal that was attenuated during the first hop after transmission, thus enhancing the signal strength at the user [155].

5.4 Simulation Results

The efficacy of the suggested algorithms is validated by the simulation results presented in this section. The simulation parameters for these results are listed in Table 5.1. Performance metrics, namely SE and NMSE as defined by $\mathbb{E} \left\{ \frac{\|\mathbf{H} - \hat{\mathbf{H}}\|_F^2}{\|\mathbf{H}\|_F^2} \right\}$ [138], are considered to assess the performance of the entire system and the estimation accuracy of various estimators, respectively.

The NMSE and SE performance of the proposed SEFWLMS algorithm is com-

Table 5.1: Simulation parameters

Parameters	Parameters
BS and UE antennas: $N_T = N_R = 16$	RF Chains: $N_{RF}^T = N_{RF}^R = 6$
Step-size: $\mu = 0.003$, error tolerance $\zeta = 10^{-3}$	Regularization step-size: $\rho_0 = 2 \times 10^{-4}$
Carrier frequency: $f_c = 28$ GHz	Reference path-loss: $\beta_0 = -30$ dB
Passive reflecting elements: $M = 4 \times 4$	Number of multi path: $L = 4$
Forgetting factor: $\lambda = 0.88$, Max-iteration = 1000	Length of sliding-window: $W = 6$
Bandwidth: $B = 100$ MHz	Path loss component: $\eta_T = \eta_R = 2$
Accuracy parameter: $\nu = 18$	Angular resolutions: $G_{BS} = G_{UE} = 16$ and $G_I = 64$
Angular resolution along x-axis: $G_x = 8$	Angular resolution along y-axis: $G_y = 8$

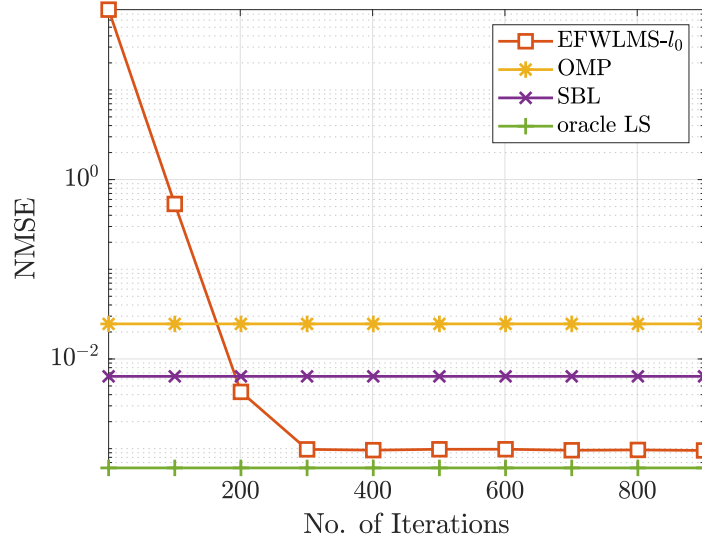


Figure 5.2: NMSE versus number of iterations performance the SEFWLMS, OMP, SBL, and oracle LS estimators.

pared with existing techniques such as OMP and SBL, as well as with oracle LS techniques for benchmarking purposes

NMSE versus Iterations

It is evident from Figure 5.2 that the proposed SEFWLMS-based estimator outperforms existing estimators in terms of accuracy. The plot shows that the NMSE floor of SEFWLMS at the converged state is lower than that of OMP and SBL and is close to the benchmark oracle LS. Therefore, it is clear that the accuracy of the SEFWLMS-based estimator is superior to that of OMP and SBL.

NMSE versus SNR

Figure 5.3 depicts NMSE versus SNR curves for the proposed SEFWLMS-based technique and the existing OMP, SBL, and benchmark oracle LS. It is evident from the plot that the NMSE for all schemes improves with increasing SNR. Furthermore,

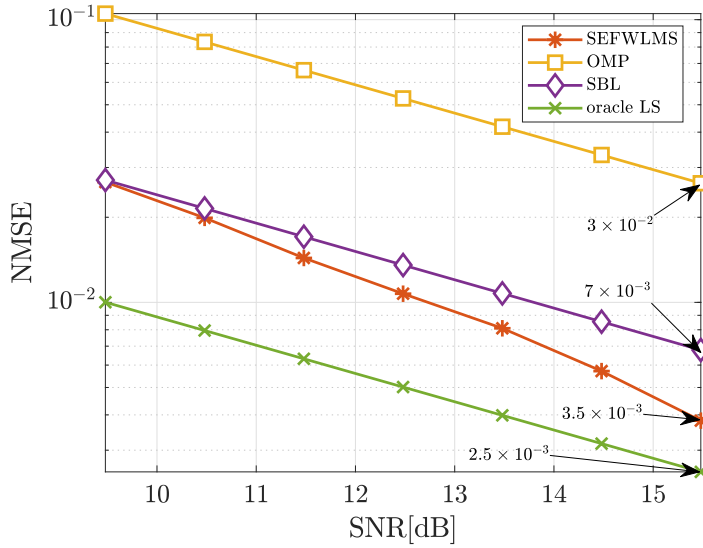


Figure 5.3: NMSE versus SNR performance the SEFWLMS, OMP, SBL, and oracle LS estimators.

it is observed that at a fixed SNR of 15.5 dB, OMP, SBL, SEFWLMS, and oracle LS achieve NMSE values of approximately 3×10^{-2} , 7×10^{-3} , 3.5×10^{-3} , and 2.5×10^{-3} , respectively. Therefore, SEFWLMS exhibits approximately nine-fold lower NMSE compared to OMP, two-fold improvement over SBL, and is close to oracle LS at the considered SNR. Moreover, the proposed scheme has a significantly lower computational complexity as compared to the OMP, SBL, and oracle LS as derived in Subsection 5.3.2. The poor performance of OMP technique is due to its lower estimation accuracy which depends on the stopping criteria and the equivalent sensing matrix.

SE versus SNR

Figure 5.4 illustrates the SE versus SNR curves for various estimators. A general trend of increasing SE is observed with improved estimating accuracy. The plot clearly shows that the SEFWLMS-based estimator provides approximately 18 bps/Hz higher SE compared to OMP and approximately 10 bps/Hz higher SE compared to the SBL estimator at higher SNR levels ($\text{SNR} > 0$ dB), approaching the performance of the oracle LS estimator. This leads us to the conclusion that the proposed SEFWLMS-based estimator enhances the overall system SE.

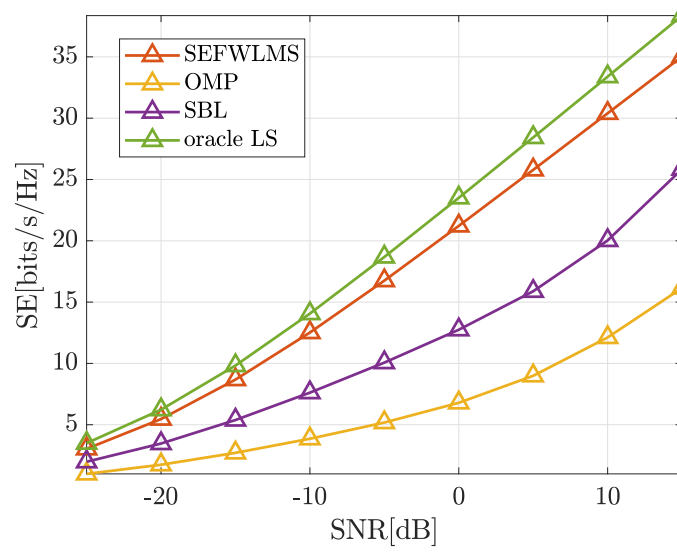


Figure 5.4: SE versus SNR performance the SEFWLMS, OMP, SBL, and oracle LS estimators.

5.5 Summary

In this work, channel estimation problem of the IRS-aided mmWave hybrid MIMO system is investigated. For the system under consideration, characteristics of Kronecker products to develop a cascaded channel estimation approach is utilized. A novel online adaptive filtering-based SEFWLMS algorithm is proposed. Simulation results demonstrate that the SEFWLMS based estimator outperforms existing approaches like OMP and SBL in terms of estimation accuracy and SE performance, closely approaching the benchmark oracle LS estimator. Consequently, choosing an SEFWLMS-based estimator is the preferred option for the system under consideration.

Chapter 6

Conclusion and Future Work

6.1 Conclusion

This thesis presents channel estimation for mmWave hybrid MIMO systems and IRS-assisted mmWave hybrid MIMO systems using an adaptive online sparsity-based channel estimator.

Initially, a ZALMS-based low-complexity, adaptive online channel estimation procedure for narrowband mmWave hybrid MIMO systems is proposed. Simulations demonstrate the superior performance of the proposed algorithm in terms of MSE and SE. Furthermore, theoretical MSE, excess MSE, and corresponding expressions for their asymptotic values are derived for the scheme.

Next, a ZALMS-based low-complexity, adaptive online channel estimation procedure for narrowband mmWave hybrid MIMO systems with HI is introduced. Subsequently, the SI-ZALMS technique is presented, which exploits the sparsity inherent in the beamspace domain model of the narrowband mmWave hybrid MIMO channel, in addition to LMS, through a regularized cost function and initialization with the result of the OMP algorithm. Further, the theoretical MSD and MSE, as well as the related equations for their asymptotic values, are determined. Next, the ranges are derived analytically for possible step size and regularization parameter values to find better convergence rate and NMSE floor. Simulations show that the proposed ZALMS and SI-ZALMS-based channel estimators outperform the existing OMP-based technique in terms of CSI estimate considering the HI. Lastly, the impact of HI on SE is derived and validated analytically.

Furthermore, the challenge of channel estimation in an IRS-assisted mmWave hybrid MIMO system is explored. The characteristics of Kronecker products are utilized to develop the cascade channel estimation approach, and a novel online adaptive VSS-ZALMS-based algorithm is proposed. A range of regularization and step size parameters for the VSS-ZALMS-based estimator is derived to achieve lower NMSE and faster convergence rates. Additionally, computational complexity, IRS location, and SE for the considered system are analyzed. Furthermore, the SE versus SNR and channel capacity versus number of reflecting elements performance for several estimators are presented. Simulation results demonstrate that the proposed VSS-ZALMS based estimator yields better estimation accuracy and higher SE performance compared to existing methods like OMP, SBL, and approaches performance close to the benchmark oracle LS estimator.

Finally, a novel online adaptive SEFWLMS-based algorithm is proposed for IRS-aided mmWave hybrid MIMO systems to achieve better MSE and convergence performance. Simulation results demonstrate that the SEFWLMS-based estimator outperforms existing approaches like OMP and SBL in terms of estimation accuracy and SE performance and closely approaches the benchmark oracle LS estimator.

These contributions pave the way for advancements in wireless communication systems, enabling higher data rates, improved reliability, and enhanced spectral efficiency in future mmWave and IRS-enabled networks.

6.2 Future Work

Sparsity-based signal processing is an emerging research area in the wireless communications. In line with this, all the algorithms developed in this thesis work are novel approaches to improve the SE of mmWave link. The work of this thesis can also be extended for THz communication, since channel of THz system is also sparse.

- In our work we have considered narrowband mmWave channel. Future research may consider for estimating the wideband mmWave MIMO channel by considering beam squint and synchronization errors.
- In our work, we have considered a passive IRS, which cannot effectively manage the double path loss due to that significant reduction in the received signal

power at the receiver. To address this issue, active IRS can be used in the future work. Furthermore, the consideration of multiple IRS units, instead of a single IRS, can also be explored.

- The IRS reflection coefficient comprises of amplitude and phase of the reflecting elements. The IRS comprises of large number of reflecting elements, and it is difficult to achieve an optimal phase shift for all the reflecting elements in practice. The impact of phase shift error can deteriorate or limit the performance of the system. The impact of phase shift error on the performance of IRS-aided systems should be investigated.

References

- [1] T. Ismail, E. Leitgeb, and T. Plank, “Free space optic and mmwave communications: technologies, challenges and applications,” *IEICE Tran. Commun.*, vol. 99, no. 6, pp. 1243–1254, 2016.
- [2] Q. Wu, S. Zhang, B. Zheng, C. You, and R. Zhang, “Intelligent reflecting surface-aided wireless communications: A tutorial,” *IEEE Tran. Commun.*, vol. 69, no. 5, pp. 3313–3351, May 2021.
- [3] B. Zheng, C. You, W. Mei, and R. Zhang, “A survey on channel estimation and practical passive beamforming design for intelligent reflecting surface aided wireless communications,” *IEEE Commun. Surv. Tutor.*, vol. 24, no. 2, pp. 1035–1071, 2nd Quart. 2022.
- [4] D. Raychaudhuri and N. B. Mandayam, “Frontiers of wireless and mobile communications,” *IEEE Proceed.*, vol. 100, no. 4, pp. 824–840, Feb. 2012.
- [5] D. Feng, C. Jiang, G. Lim, L. J. Cimini, G. Feng, and G. Y. Li, “A survey of energy-efficient wireless communications,” *IEEE Commun. Surveys Tut.*, vol. 15, no. 1, pp. 167–178, 2012.
- [6] L. Wei, R. Q. Hu, Y. Qian, and G. Wu, “Key elements to enable millimeter wave communications for 5G wireless systems,” *IEEE Wireless Commun.*, vol. 21, no. 6, pp. 136–143, 2014.
- [7] T. L. Marzetta, “Noncooperative cellular wireless with unlimited numbers of base station antennas,” *IEEE Tran. Wireless Commun.*, vol. 9, no. 11, pp. 3590–3600, 2010.

- [8] T. Nitsche, C. Cordeiro, A. B. Flores, E. W. Knightly, E. Perahia, and J. C. Widmer, "Ieee 802.11 ad: directional 60 GHz communication for multi-Gigabit-per-second Wi-Fi," *IEEE Commun. Mag.*, vol. 52, no. 12, pp. 132–141, 2014.
- [9] P. Wang, Y. Li, L. Song, and B. Vucetic, "Multi-gigabit millimeter wave wireless communications for 5G: from fixed access to cellular networks," *IEEE Commun. Mag.*, vol. 53, no. 1, pp. 168–178, 2015.
- [10] N. Guo, R. C. Qiu, S. S. Mo, and K. Takahashi, "60-GHz millimeter-wave radio: Principle, technology, and new results," *EURASIP J. Wireless Commun. Net.*, vol. 2007, pp. 1–8, 2006.
- [11] S. Geng and X. Zhao, "Feasibility study of E-band mm-Wave for Gigabit point-to-point wireless communications," *Microwave Opt. Technol. Lett.*, vol. 55, no. 8, pp. 1969–1972, 2013.
- [12] T. S. Rappaport, "Wireless communications—principles and practice, (the book end)." *Microwave Journal*, vol. 45, no. 12, pp. 128–129, 2002.
- [13] R. W. Heath, N. Gonzalez-Prelcic, S. Rangan, W. Roh, and A. M. Sayeed, "An overview of signal processing techniques for millimeter wave MIMO systems," *IEEE J. Sel. Top. Signal Process.*, vol. 10, no. 3, pp. 436–453, Apr. 2016.
- [14] T. S. Rappaport, R. W. Heath Jr, R. C. Daniels, and J. N. Murdock, *Millimeter wave wireless communications*. Pearson Education, 2015.
- [15] J. Singh and S. Ramakrishna, "On the feasibility of beamforming in millimeter wave communication systems with multiple antenna arrays," in *2014 IEEE Global Commun. Conf.* IEEE, 2014, pp. 3802–3808.
- [16] T. Bai, A. Alkhateeb, and R. W. Heath, "Coverage and capacity of millimeter-wave cellular networks," *IEEE Commun. Mag.*, vol. 52, no. 9, pp. 70–77, 2014.
- [17] M. R. Akdeniz, Y. Liu, M. K. Samimi, S. Sun, S. Rangan, T. S. Rappaport, and E. Erkip, "Millimeter wave channel modeling and cellular capacity evaluation," *IEEE J. Sel. Areas Commun.*, vol. 32, no. 6, pp. 1164–1179, 2014.

- [18] T. S. Rappaport, S. Sun, R. Mayzus, H. Zhao, Y. Azar, K. Wang, G. N. Wong, J. K. Schulz, M. Samimi, and F. Gutierrez, “Millimeter wave mobile communications for 5G cellular: It will work!” *IEEE Access*, vol. 1, pp. 335–349, May 2013.
- [19] O. El Ayach, S. Rajagopal, S. Abu-Surra, Z. Pi, and R. W. Heath, “Spatially sparse precoding in millimeter wave MIMO systems,” *IEEE Tran. Wireless Commun.*, vol. 13, no. 3, pp. 1499–1513, Mar. 2014.
- [20] H. Xu, V. Kukshya, and T. S. Rappaport, “Spatial and temporal characteristics of 60-GHz indoor channels,” *IEEE J. Sel. Areas Commun.*, vol. 20, no. 3, pp. 620–630, 2002.
- [21] O. El Ayach, R. W. Heath, S. Abu-Surra, S. Rajagopal, and Z. Pi, “Low complexity precoding for large millimeter wave MIMO systems,” in *2012 IEEE int. conf. commun. (ICC)*. IEEE, 2012, pp. 3724–3729.
- [22] A. Sayeed and J. Brady, “Beamspace MIMO for high-dimensional multiuser communication at millimeter-wave frequencies,” in *2013 IEEE Global commun. conf. (GLOBECOM)*. IEEE, 2013, pp. 3679–3684.
- [23] J. Mo, P. Schniter, N. G. Prelcic, and R. W. Heath, “Channel estimation in millimeter wave MIMO systems with one-bit quantization,” in *2014 48th Asilomar Conf. Signals, Systems and Computers*. IEEE, 2014, pp. 957–961.
- [24] T. S. Rappaport, G. R. MacCartney, M. K. Samimi, and S. Sun, “Wideband millimeter-wave propagation measurements and channel models for future wireless communication system design,” *IEEE Tran. Commun.*, vol. 63, no. 9, pp. 3029–3056, 2015.
- [25] P. Schniter and A. Sayeed, “Channel estimation and precoder design for millimeter-wave communications: The sparse way,” in *2014 48th Asilomar conf. signals, systems and computers*. IEEE, 2014, pp. 273–277.
- [26] G. M. Rebeiz, S.-Y. Kim, O. Inac, W. Shin, O. Gurbuz, Y.-C. Ou, F. Golcuk, T. Kanar, and B.-H. Ku, “Millimeter-wave large-scale phased-arrays for 5g

- systems,” in *2015 IEEE MTT-S Int. Microwave Symposium*. IEEE, 2015, pp. 1–3.
- [27] E. Access, “Further advancements for E-UTRA physical layer aspects,” *3GPP Technical Specification TR*, vol. 36, p. V2, 2010.
- [28] M. B. Zid, K. Raouf, and A. Bouallègue, “Mimo spectral efficiency over energy consumption requirements: Application to wsns,” *Int. J. Commun. Net. System Sciences*, vol. 5, no. 2, pp. 121–129, 2012.
- [29] Y. Li, B. Bakkaloglu, and C. Chakrabarti, “A comprehensive energy model and energy-quality evaluation of wireless transceiver front-ends,” in *IEEE Workshop Signal Process. Systems Design and Implementation, 2005*. IEEE, 2005, pp. 262–267.
- [30] D. C. Daly, P. P. Mercier, M. Bhardwaj, A. L. Stone, Z. N. Aldworth, T. L. Daniel, J. Voldman, J. G. Hildebrand, and A. P. Chandrakasan, “A pulsed uwb receiver SoC for insect motion control,” *IEEE J. Solid-state Circuits*, vol. 45, no. 1, pp. 153–166, 2009.
- [31] M. N. Kulkarni, A. Ghosh, and J. G. Andrews, “A comparison of MIMO techniques in downlink millimeter wave cellular networks with hybrid beamforming,” *IEEE Tran. Commun.*, vol. 64, no. 5, pp. 1952–1967, 2016.
- [32] S. Han, I. Chih-Lin, Z. Xu, and C. Rowell, “Large-scale antenna systems with hybrid analog and digital beamforming for millimeter wave 5g,” *IEEE Commun. Mag.*, vol. 53, no. 1, pp. 186–194, 2015.
- [33] X. Gao, O. Edfors, F. Tufvesson, and E. G. Larsson, “Multi-switch for antenna selection in massive MIMO,” in *2015 IEEE Global Commun. Conf. (GLOBECOM)*. IEEE, 2015, pp. 1–6.
- [34] W. Hong, Z. H. Jiang, C. Yu, J. Zhou, P. Chen, Z. Yu, H. Zhang, B. Yang, X. Pang, M. Jiang *et al.*, “Multibeam antenna technologies for 5G wireless communications,” *IEEE Tran. Antennas Prop.*, vol. 65, no. 12, pp. 6231–6249, 2017.

- [35] M. A. B. Abbasi, V. F. Fusco, H. Tataria, and M. Matthaiou, “Constant lens beamformer for low-complexity millimeter-wave hybrid MIMO,” *IEEE Tran. Microwave Theo. Techn.*, vol. 67, no. 7, pp. 2894–2903, 2019.
- [36] J. Mo and R. W. Heath, “Capacity analysis of one-bit quantized mimo systems with transmitter channel state information,” *IEEE Tran. Signal Process.*, vol. 63, no. 20, pp. 5498–5512, 2015.
- [37] J. Singh, O. Dabeer, and U. Madhow, “On the limits of communication with low-precision analog-to-digital conversion at the receiver,” *IEEE Tran. Commun.*, vol. 57, no. 12, pp. 3629–3639, 2009.
- [38] A. Alkhateeb, J. Mo, N. Gonzalez-Prelcic, and R. W. Heath, “MIMO precoding and combining solutions for millimeter-wave systems,” *IEEE Commun. Maga.*, vol. 52, no. 12, pp. 122–131, 2014.
- [39] A. Mezghani, F. Antreich, and J. A. Nossek, “Multiple parameter estimation with quantized channel output,” in *2010 Int. ITG Workshop Smart Antennas (WSA)*. IEEE, 2010, pp. 143–150.
- [40] S. Hur, T. Kim, D. J. Love, J. V. Krogmeier, T. A. Thomas, and A. Ghosh, “Millimeter wave beamforming for wireless backhaul and access in small cell networks,” *IEEE Tran. Commun.*, vol. 61, no. 10, pp. 4391–4403, 2013.
- [41] J. Wang, Z. Lan, C.-W. Pyo, T. Baykas, C.-S. Sum, M. A. Rahman, J. Gao, R. Funada, F. Kojima, H. Harada *et al.*, “Beam codebook based beamforming protocol for multi-gbps millimeter-wave wpan systems,” *IEEE J. Sel. Areas Commun.*, vol. 27, no. 8, pp. 1390–1399, Oct. 2009.
- [42] Y. M. Tsang, A. S. Poon, and S. Addepalli, “Coding the beams: Improving beamforming training in mmwave communication system,” in *2011 IEEE Global Telecommun. Conf. GLOBECOM 2011*. IEEE, Jan. 2011, pp. 1–6.
- [43] A. Alkhateeb, O. El Ayach, G. Leus, and R. W. Heath, “Channel estimation and hybrid precoding for millimeter wave cellular systems,” *IEEE J. Sel. Top. Signal Process.*, vol. 8, no. 5, pp. 831–846, Oct. 2014.

- [44] D. Tse and P. Viswanath, *Fundamentals of wireless communication*. Cambridge university press, 2005.
- [45] R. Méndez-Rial, C. Rusu, A. Alkhateeb, N. González-Prelcic, and R. W. Heath, “Channel estimation and hybrid combining for mmwave: Phase shifters or switches?” in *2015 Inf. Theory Applications Workshop (ITA)*. IEEE, 2015, pp. 90–97.
- [46] D. L. Donoho, “Compressed sensing,” *IEEE Tran. Inf. Theory*, vol. 52, no. 4, pp. 1289–1306, 2006.
- [47] Y. Nesterov and A. Nemirovskii, *Interior-point polynomial algorithms in convex programming*. SIAM, 1994.
- [48] D. G. Luenberger, Y. Ye *et al.*, *Linear and nonlinear programming*. Springer, 1984, vol. 2.
- [49] S. S. Chen, D. L. Donoho, and M. A. Saunders, “Atomic decomposition by basis pursuit,” *SIAM review*, vol. 43, no. 1, pp. 129–159, 2001.
- [50] C. A. Johnson, J. Seidel, and A. Sofer, “Interior-point methodology for 3-d pet reconstruction,” *IEEE Tran. Medical Imaging*, vol. 19, no. 4, pp. 271–285, 2000.
- [51] E. Candes and J. Romberg, “l1-magic: A collection of matlab routines for solving the convex optimization programs central to compressive sampling,” *Available: www.acm.caltech.edu/l1magic*, 2006.
- [52] M. Saunders, “Pdco: Primal-dual interior method for convex objectives 2002,” 2002.
- [53] C. C. Paige and M. A. Saunders, “LSQR: an algorithm for sparse linear equations and sparse least squares,” *ACM Tran. Mathematical Software (TOMS)*, vol. 8, no. 1, pp. 43–71, 1982.
- [54] M. R. Osborne, B. Presnell, and B. A. Turlach, “A new approach to variable selection in least squares problems,” *IMA journal of numerical analysis*, vol. 20, no. 3, pp. 389–403, 2000.

- [55] B. A. Turlach, “On algorithms for solving least squares problems under an l1 penalty or an l1 constraint,” in *2004 Proceedings of the American Statistical Association, Statistical Computing Section [CD-ROM]*, 2005, pp. 2572–2577.
- [56] B. Efron, T. Hastie, I. Johnstone, and R. Tibshirani, “Least angle regression,” 2004.
- [57] D. Donoho and Y. Tsaig, “Fast solution of l1-norm minimization problems when the solution may be sparse, 2006,” *Preprint*, vol. 1, no. 2.
- [58] J. Friedman, T. Hastie, H. Höfling, and R. Tibshirani, “Pathwise coordinate optimization,” 2007.
- [59] E. T. Hale, W. Yin, and Y. Zhang, “A fixed-point continuation method for l1-regularized minimization with applications to compressed sensing,” *CAAM TR07-07, Rice University*, vol. 43, p. 44, 2007.
- [60] G. Narkiss and M. Zibulevsky, *Sequential subspace optimization method for large-scale unconstrained problems*. Technion-IIT, Department of Electrical Engineering, 2005.
- [61] M. A. Figueiredo and R. D. Nowak, “A bound optimization approach to wavelet-based image deconvolution,” in *IEEE International Conference on Image Processing 2005*, vol. 2. IEEE, 2005, pp. II–782.
- [62] I. Daubechies, M. Defrise, and C. De Mol, “An iterative thresholding algorithm for linear inverse problems with a sparsity constraint,” *Communications on Pure and Applied Mathematics: A Journal Issued by the Courant Institute of Mathematical Sciences*, vol. 57, no. 11, pp. 1413–1457, 2004.
- [63] Y. Nesterov, “Gradient methods for minimizing composite functions,” *Mathematical programming*, vol. 140, no. 1, pp. 125–161, 2013.
- [64] M. A. Figueiredo, R. D. Nowak, and S. J. Wright, “Gradient projection for sparse reconstruction: Application to compressed sensing and other inverse problems,” *IEEE J. Sel. Top. signal process.*, vol. 1, no. 4, pp. 586–597, 2007.

- [65] S. J. Wright, R. D. Nowak, and M. A. Figueiredo, “Sparse reconstruction by separable approximation,” *IEEE Tran. Signal Process.*, vol. 57, no. 7, pp. 2479–2493, 2009.
- [66] J. Cai, S. Osher, and Z. Shen, “Linearized bregman iterations for compressive sensing,” *UCLA CAM TR08-06*.
- [67] W. Yin, S. Osher, D. Goldfarb, and J. Darbon, “Bregman iterative algorithms for ℓ_1 -minimization with applications to compressed sensing,” *SIAM J. Imag. Sciences*, vol. 1, no. 1, pp. 143–168, 2008.
- [68] I. F. Gorodnitsky and B. D. Rao, “Sparse signal reconstruction from limited data using FOCUSS: A re-weighted minimum norm algorithm,” *IEEE Tran. Signal Process.*, vol. 45, no. 3, pp. 600–616, 1997.
- [69] R. Chartrand and W. Yin, “Iteratively reweighted algorithms for compressive sensing,” in *2008 IEEE Int. Conf. Acoustics, Speech and Signal Process.* IEEE, 2008, pp. 3869–3872.
- [70] I. Daubechies, R. DeVore, M. Fornasier, and C. S. Güntürk, “Iteratively reweighted least squares minimization for sparse recovery,” *Communications on Pure and Applied Mathematics: J. Issued by the Courant Institute of Mathematical Sciences*, vol. 63, no. 1, pp. 1–38, 2010.
- [71] Y. C. Pati, R. Rezaifar, and P. S. Krishnaprasad, “Orthogonal matching pursuit: Recursive function approximation with applications to wavelet decomposition,” in *Proceedings of 27th Asilomar Conf. Signals, Systems and Comp.* IEEE, 1993, pp. 40–44.
- [72] J. A. Tropp and A. C. Gilbert, “Signal recovery from random measurements via orthogonal matching pursuit,” *IEEE Tran. Inf. Theory*, vol. 53, no. 12, pp. 4655–4666, 2007.
- [73] D. L. Donoho, Y. Tsaig, I. Drori, and J.-L. Starck, “Sparse solution of underdetermined systems of linear equations by stagewise orthogonal matching pursuit,” *IEEE Tran. Inf. Theory*, vol. 58, no. 2, pp. 1094–1121, 2012.

- [74] D. Needell and R. Vershynin, “Signal recovery from incomplete and inaccurate measurements via regularized orthogonal matching pursuit,” *IEEE J. Sel. Top. Signal Process.*, vol. 4, no. 2, pp. 310–316, 2010.
- [75] W. Dai and O. Milenkovic, “Subspace pursuit for compressive sensing: Closing the gap between performance and complexity,” *arXiv preprint arXiv:0803.0811*, vol. 803, 2008.
- [76] D. Needell and J. A. Tropp, “Cosamp: Iterative signal recovery from incomplete and inaccurate samples,” *Applied Comput. Harmonic Analysis*, vol. 26, no. 3, pp. 301–321, 2009.
- [77] T. Blumensath and M. E. Davies, “Iterative hard thresholding for compressed sensing,” *Applied Comput. Harmonic Analysis*, vol. 27, no. 3, pp. 265–274, 2009.
- [78] S. Gong, X. Lu, D. T. Hoang, D. Niyato, L. Shu, D. I. Kim, and Y.-C. Liang, “Toward smart wireless communications via intelligent reflecting surfaces: A contemporary survey,” *IEEE Commun. Sur. Tutor.*, vol. 22, no. 4, pp. 2283–2314, 4th Quart. 2020.
- [79] F. Liu and *et. al.*, “Programmable metasurfaces: State of the art and prospects,” in *IEEE Inter. Symp. Circuits Syst. (ISCAS)*. IEEE, May 2018, pp. 1–5.
- [80] F. Ding, A. Pors, and S. I. Bozhevolnyi, “Gradient metasurfaces: a review of fundamentals and applications,” *Rep. Progr. Phys.*, vol. 81, no. 2, p. 026401, Dec. 2017.
- [81] S. Zhou, W. Xu, K. Wang, M. Di Renzo, and M.-S. Alouini, “Spectral and energy efficiency of IRS-assisted MISO communication with hardware impairments,” *IEEE Wireless Commun. Lett.*, vol. 9, no. 9, pp. 1366–1369, Sep. 2020.
- [82] P. K. Singya, N. Kumar, and V. Bhatia, “Mitigating NLD for wireless networks: Effect of nonlinear power amplifiers on future wireless communication networks,” *IEEE Microw. Mag.*, vol. 18, no. 5, pp. 73–90, Jun. 2017.

- [83] E. Balti and M. Guizani, “Impact of non-linear high-power amplifiers on cooperative relaying systems,” *IEEE Tran. Commun.*, vol. 65, no. 10, pp. 4163–4175, July 2017.
- [84] J. Li and J. Ilow, “Adaptive volterra predistorters for compensation of non-linear effects with memory in OFDM transmitters,” in *Commun. Netw. Services Res. Conf. (CNSR)*. IEEE, May 2006, pp. 4–pp.
- [85] E. Björnson, J. Hoydis, M. Kountouris, and M. Debbah, “Massive MIMO systems with non-ideal hardware: Energy efficiency, estimation, and capacity limits,” *IEEE Tran. Inf. Theory*, vol. 60, no. 11, pp. 7112–7139, Nov. 2014.
- [86] C. Studer, M. Wenk, and A. Burg, “MIMO transmission with residual transmit-RF impairments,” in *2010 international ITG workshop on smart antennas (WSA)*. IEEE, Apr. 2010, pp. 189–196.
- [87] H. Holma and A. Toskala, *LTE for UMTS: Evolution to LTE-advanced*. John Wiley & Sons, 2011.
- [88] A. Chaoub, M. Giordani, B. Lall, V. Bhatia, A. Kliks, L. Mendes, K. Rabie, H. Saarnisaari, A. Singhal, N. Zhang *et al.*, “6G for bridging the digital divide: Wireless connectivity to remote areas,” *IEEE Wireless Commun.*, Jul. 2021.
- [89] V. Bhatia, P. Swami, S. Sharma, and R. Mitra, “Non-orthogonal multiple access as an enabler for massive connectivity for 5G and beyond networks,” *arXiv preprint arXiv:1912.07077*, 2019.
- [90] M. Xiao, S. Mumtaz, Y. Huang, L. Dai, Y. Li, M. Matthaiou, G. K. Karagiannidis, E. Björnson, K. Yang, I. Chih-Lin *et al.*, “Millimeter wave communications for future mobile networks,” *IEEE J. Sel. Areas Commun.*, vol. 35, no. 9, pp. 1909–1935, Sep. 2017.
- [91] I. A. Hemadeh, K. Satyanarayana, M. El-Hajjar, and L. Hanzo, “Millimeter-wave communications: Physical channel models, design considerations, antenna constructions, and link-budget,” *IEEE Commun. Surveys Tut.*, vol. 20, no. 2, pp. 870–913, Apr.-Jun. 2017.

- [92] R. Mitra and V. Bhatia, "Adaptive sparse dictionary-based kernel minimum symbol error rate post-distortion for nonlinear LEDs in visible light communications," *IEEE Photonics J.*, vol. 8, no. 4, pp. 1–13, Aug. 2016.
- [93] J. Lee, G.-T. Gil, and Y. H. Lee, "Channel estimation via orthogonal matching pursuit for hybrid MIMO systems in millimeter wave communications," *IEEE Tran. Commun.*, vol. 64, no. 6, pp. 2370–2386, Jun. 2016.
- [94] R. Mitra and V. Bhatia, "Minimum error entropy criterion based channel estimation for massive-MIMO in VLC," *IEEE Tran. Veh. Technol.*, vol. 68, no. 1, pp. 1014–1018, Nov. 2018.
- [95] ———, "Precoded Chebyshev-NLMS-based pre-distorter for nonlinear LED compensation in NOMA-VLC," *IEEE Tran. Commun.*, vol. 65, no. 11, pp. 4845–4856, Nov. 2017.
- [96] Z. Guo, X. Wang, and W. Heng, "Millimeter-wave channel estimation based on 2-D beamspace MUSIC method," *IEEE Tran. Wireless Commun.*, vol. 16, no. 8, pp. 5384–5394, Aug. 2017.
- [97] V. Bhatia and B. Mulgrew, "Non-parametric likelihood based channel estimator for Gaussian mixture noise," *Signal Processing*, vol. 87, no. 11, pp. 2569–2586, Nov. 2007.
- [98] S. Srivastava, P. Sharma, S. Dwivedi, A. K. Jagannatham, and L. Hanzo, "Fast block LMS based estimation of angularly sparse channels for single-carrier wideband millimeter wave hybrid MIMO systems," *IEEE Tran. Veh. Technol.*, vol. 70, no. 1, pp. 666–681, Jan. 2021.
- [99] S. Srivastava, A. Mishra, A. Rajoriya, A. K. Jagannatham, and G. Ascheid, "Quasi-static and time-selective channel estimation for block-sparse millimeter wave hybrid MIMO systems: Sparse bayesian learning (SBL) based approaches," *IEEE Tran. Signal Process.*, vol. 67, no. 5, pp. 1251–1266, Mar. 2019.
- [100] A. H. Sayed, *Fundamentals of Adaptive Filtering*. John Wiley & Sons, 2003.

- [101] S. Srivastava, A. Mishra, A. K. Jagannatham, and G. Ascheid, “SBL-based hybrid precoder/combiner design for power and spectrally efficient millimeter wave MIMO systems,” in *2020 Int. Conf. Signal Process. Commun. (SPCOM)*. IEEE, Jul. 2020, pp. 1–5.
- [102] J. Jin, Y. Gu, and S. Mei, “A stochastic gradient approach on compressive sensing signal reconstruction based on adaptive filtering framework,” *IEEE J. Sel. Top. Signal Process.*, vol. 4, no. 2, pp. 409–420, Apr. 2010.
- [103] A. Papoulis and S. U. Pillai, *Probability, Random Variables, and Stochastic Process*. Tata Mcgraw Hill, 2002.
- [104] S. Ali, W. Saad, N. Rajatheva, K. Chang, D. Steinbach, B. Sliwa, C. Wietfeld, K. Mei, H. Shiri, H.-J. Zepernick *et al.*, “6G white paper on machine learning in wireless communication networks,” *arXiv preprint arXiv:2004.13875*, 2020.
- [105] R. Mitra and V. Bhatia, “Precoding technique for ill-conditioned massive mimo-vlc system,” in *2018 IEEE 87th Veh. Technol. Confer. (VTC Spring)*. IEEE, Jul. 2018, pp. 1–5.
- [106] M. S. Elbamby, C. Perfecto, M. Bennis, and K. Doppler, “Edge computing meets millimeter-wave enabled VR: Paving the way to cutting the cord,” in *2018 IEEE Wireless Commun. Net. Conf. (WCNC)*. IEEE, Jun. 2018, pp. 1–6.
- [107] S. Rangan, T. S. Rappaport, and E. Erkip, “Millimeter-wave cellular wireless networks: Potentials and challenges,” *Proceedings of the IEEE*, vol. 102, no. 3, pp. 366–385, Feb. 2014.
- [108] A. I. Sulyman, A. T. Nassar, M. K. Samimi, G. R. MacCartney, T. S. Rappaport, and A. Alsanie, “Radio propagation path loss models for 5G cellular networks in the 28 ghz and 38 GHz millimeter-wave bands,” *IEEE Commun. Mag.*, vol. 52, no. 9, pp. 78–86, Sep. 2014.
- [109] T. Kim and D. J. Love, “Virtual AoA and AoD estimation for sparse millimeter wave MIMO channels,” in *2015 IEEE 16th Int. Workshop on Signal Process. Advances Wireless Commun. (SPAWC)*, Aug., pp. 146–150.

- [110] J. Rodríguez-Fernández, N. González-Prelcic, K. Venugopal, and R. W. Heath, “Frequency-domain compressive channel estimation for frequency-selective hybrid millimeter wave MIMO systems,” *IEEE Tran. Wireless Commun.*, vol. 17, no. 5, pp. 2946–2960, May 2018.
- [111] A. Bishnu and V. Bhatia, “Iterative time-domain-based sparse channel estimation for ieee 802.22,” *IEEE Wireless Commun. Lett.*, vol. 6, no. 3, pp. 290–293, Jun. 2017.
- [112] —, “A zero attracting natural gradient non-parametric maximum likelihood for sparse channel estimation,” in *GLOBECOM 2017-2017 IEEE Global Commun. Confer.* IEEE, Jan. 2017, pp. 1–6.
- [113] —, “Sparse channel estimation for interference limited ofdm systems and its convergence analysis,” *IEEE Access*, vol. 5, pp. 17 781–17 794, Sep. 2017.
- [114] L. Wan, K. Liu, and W. Zhang, “Deep learning-aided off-grid channel estimation for millimeter wave cellular systems,” *IEEE Tran. Wireless Commun.*, vol. 21, no. 5, pp. 3333–3348, May. 2022.
- [115] L. Wan, K. Liu, Y.-C. Liang, and T. Zhu, “DOA and polarization estimation for non-circular signals in 3-D millimeter wave polarized massive MIMO systems,” *IEEE Tran. Wireless Commun.*, vol. 20, no. 5, pp. 3152–3167, May. 2021.
- [116] V. B. Shukla, R. Mitra, and V. Bhatia, “Adaptive sparse aware algorithm based channel estimation for mmwave hybrid MIMO system,” in *2021 IEEE Intern. Conf. Advanced Networks and Telecommun. Systems (ANTS)*. IEEE, 2021, pp. 290–295.
- [117] —, “Millimeter wave hybrid MIMO system channel estimation using variable step size zero attracting lms,” in *2022 IEEE Inter. Conf. Signal Process. Commun. (SPCOM)*. IEEE, 2022, pp. 1–5.
- [118] H. Wang, P. Xiao, and X. Li, “Channel parameter estimation of mmwave mimo system in urban traffic scene: a training channel-based method,” *IEEE Tran. Intell. Transp. Syst.*, 2022.

- [119] H. Wang, L. Xu, Z. Yan, and T. A. Gulliver, “Low-complexity MIMO-FBMC sparse channel parameter estimation for industrial big data communications,” *IEEE Tran. Indus. Inf.*, vol. 17, no. 5, pp. 3422–3430, May. 2020.
- [120] X. Xia, D. Zhang, K. Xu, W. Ma, and Y. Xu, “Hardware impairments aware transceiver for full-duplex massive MIMO relaying,” *IEEE Tran. Signal Process.*, vol. 63, no. 24, pp. 6565–6580, Aug. 2015.
- [121] X. Zhang, M. Matthaiou, E. Björnson, M. Coldrey, and M. Debbah, “On the MIMO capacity with residual transceiver hardware impairments,” in *2014 IEEE Int. Conf. Commun. (ICC)*. IEEE, Aug. 2014, pp. 5299–5305.
- [122] X. Dai, R. Zou, S. Sun, and Y. Wang, “Transceiver impairments on the performance of the LMMSE-PIC iterative receiver and its mitigation,” *IEEE Commun. Lett.*, vol. 17, no. 8, pp. 1536–1539, Jul. 2013.
- [123] T. Schenk, *RF imperfections in high-rate wireless systems: impact and digital compensation*. Springer, 2008.
- [124] A. Khansefid, H. Minn, N. Al-Dhahir, H. Huang, and X. Du, “Pilot designs and compensation scheme for severe RF distortions in millimeter-wave massive MIMO systems,” in *2016 IEEE Globecom Workshops (GC Wkshps)*. IEEE, Feb. 2016, pp. 1–6.
- [125] H. Minn, Q. Zhan, N. Al-Dhahir, and H. Huang, “In-phase and quadrature timing mismatch estimation and compensation in millimeter-wave communication systems,” *IEEE Tran. Wireless Commun.*, vol. 16, no. 7, pp. 4317–4331, Apr. 2017.
- [126] Y. Wu, Y. Gu, and Z. Wang, “Efficient channel estimation for mmwave MIMO with transceiver hardware impairments,” *IEEE Tran. Veh. Technol.*, vol. 68, no. 10, pp. 9883–9895, Aug. 2019.
- [127] K. Shi and X. Ma, “Transform domain LMS algorithms for sparse system identification,” in *2010 IEEE International Conf. on Acoustics, Speech and Signal Process.* IEEE, Jun. 2010, pp. 3714–3717.

- [128] S. S. Haykin, *Adaptive filter theory*. Pearson Education India, 2008.
- [129] Y. Wu, Y. Gu, and Z. Wang, “Channel estimation for mmwave MIMO with transmitter hardware impairments,” *IEEE Commun. Lett.*, vol. 22, no. 2, pp. 320–323, Nov. 2017.
- [130] A. Ghosh et al., “Millimeter-wave enhanced local area systems: A high-data-rate approach for future wireless networks,” *IEEE J. Sel. Areas Commun.*, vol. 32, no. 6, pp. 1152–1163, Jun. 2014.
- [131] V. B. Shukla, R. Mitra, O. Krejcar, V. Bhatia, and K. Choi, “Performance analysis of sparse channel estimators for millimeter wave hybrid mimo systems with non-ideal hardware,” *IEEE Tran. Veh. Technol.*, pp. 1–11, Apr. 26, 2023.
- [132] Q. Wu and R. Zhang, “Towards smart and reconfigurable environment: Intelligent reflecting surface aided wireless network,” *IEEE Commun. Mag.*, vol. 58, no. 1, pp. 106–112, 2019.
- [133] L. Zhang, Y. Wang, W. Tao, Z. Jia, T. Song, and C. Pan, “Intelligent reflecting surface aided MIMO cognitive radio systems,” *IEEE Tran. Vehi. Technol.*, vol. 69, no. 10, pp. 11 445–11 457, 2020.
- [134] E. Basar, M. Di Renzo, J. De Rosny, M. Debbah, M.-S. Alouini, and R. Zhang, “Wireless communications through reconfigurable intelligent surfaces,” *IEEE Access*, vol. 7, pp. 116 753–116 773, 2019.
- [135] A. Taha, M. Alrabeiah, and A. Alkhateeb, “Enabling large intelligent surfaces with compressive sensing and deep learning,” *IEEE Access*, vol. 9, pp. 44 304–44 321, 2021.
- [136] D. Mishra and H. Johansson, “Channel estimation and low-complexity beamforming design for passive intelligent surface assisted MISO wireless energy transfer,” in *ICASSP 2019-2019 IEEE Int. Conf. Acoustics, Speech and Signal Processing (ICASSP)*. IEEE, 2019, pp. 4659–4663.
- [137] T. L. Jensen and E. De Carvalho, “An optimal channel estimation scheme for intelligent reflecting surfaces based on a minimum variance unbiased esti-

- mator,” in *ICASSP 2020-2020 IEEE International Conference on Acoustics, Speech and Signal Processing (ICASSP)*. IEEE, 2020, pp. 5000–5004.
- [138] P. Wang, J. Fang, H. Duan, and H. Li, “Compressed channel estimation for intelligent reflecting surface-assisted millimeter wave systems,” *IEEE Signal Process. Letters*, vol. 27, pp. 905–909, 2020.
- [139] S. Liu, Z. Gao, J. Zhang, M. Di Renzo, and M.-S. Alouini, “Deep denoising neural network assisted compressive channel estimation for mmwave intelligent reflecting surfaces,” *IEEE Tran. Veh. Technol.*, vol. 69, no. 8, pp. 9223–9228, 2020.
- [140] Z. Chen, J. Tang, X. Y. Zhang, D. K. C. So, S. Jin, and K.-K. Wong, “Hybrid evolutionary-based sparse channel estimation for IRS-assisted mmwave mimo systems,” *IEEE Tran. Wireless Commun.*, vol. 21, no. 3, pp. 1586–1601, 2021.
- [141] T. Lin, X. Yu, Y. Zhu, and R. Schober, “Channel estimation for IRS-assisted millimeter-wave MIMO systems: Sparsity-inspired approaches,” *IEEE Tran. Commun.*, vol. 70, no. 6, pp. 4078–4092, Jun. 2022.
- [142] Z. Tan, P. Yang, and A. Nehorai, “Joint sparse recovery method for compressed sensing with structured dictionary mismatches,” *IEEE Tran. Signal Process.*, vol. 62, no. 19, pp. 4997–5008, 2014.
- [143] R. H. Kwong and E. W. Johnston, “A variable step size LMS algorithm,” *IEEE Tran. Signal Process.*, vol. 40, no. 7, pp. 1633–1642, Jul. 1992.
- [144] C. R. Berger, Z. Wang, J. Huang, and S. Zhou, “Application of compressive sensing to sparse channel estimation,” *IEEE Commun. Mag.*, vol. 48, no. 11, pp. 164–174, 2010.
- [145] X. Ma, Z. Chen, W. Chen, Z. Li, Y. Chi, C. Han, and S. Li, “Joint channel estimation and data rate maximization for intelligent reflecting surface assisted terahertz MIMO communication systems,” *IEEE Access*, vol. 8, pp. 99 565–99 581, 2020.

- [146] Ö. Özdoğan, E. Björnson, and E. G. Larsson, “Intelligent reflecting surfaces: Physics, propagation, and pathloss modeling,” *IEEE Wireless Commun. Lett.*, vol. 9, no. 5, pp. 581–585, May. 2019.
- [147] Z.-Q. He and X. Yuan, “Cascaded channel estimation for large intelligent metasurface assisted massive MIMO,” *IEEE Wireless Commun. Lett.*, vol. 9, no. 2, pp. 210–214, 2019.
- [148] G. Zhou, C. Pan, H. Ren, P. Popovski, and A. L. Swindlehurst, “Channel estimation for RIS-aided multiuser millimeter-wave systems,” *IEEE Tran. Signal Process.*, vol. 70, pp. 1478–1492, Mar. 2022.
- [149] K. Zhi and et al., “Two-timescale design for reconfigurable intelligent surface-aided massive MIMO systems with imperfect CSI,” *IEEE Tran. Inf. Theory*, vol. 69, no. 5, pp. 3001–3033, May. 2023.
- [150] K. Zhi, C. Pan, G. Zhou, H. Ren, M. ElKashlan, and R. Schober, “Is RIS-aided massive MIMO promising with ZF detectors and imperfect CSI?” *IEEE J. Sel. Areas Commun.*, vol. 40, no. 10, pp. 3010–3026, Oct. 2022.
- [151] Q. Wu and R. Zhang, “Intelligent reflecting surface enhanced wireless network via joint active and passive beamforming,” *IEEE Tran. Wireless Commun.*, vol. 18, no. 11, pp. 5394–5409, 2019.
- [152] Y. Ding and B. D. Rao, “Dictionary learning-based sparse channel representation and estimation for FDD massive MIMO systems,” *IEEE Tran. Wireless Commun.*, vol. 17, no. 8, pp. 5437–5451, Aug. 2018.
- [153] S. S. Haykin, *Adaptive filter theory*. Pearson Education India, 2002.
- [154] J. Weston, A. Elisseeff, B. Schölkopf, and M. Tipping, “Use of the zero norm with linear models and kernel methods,” *J. Machine Learning Research*, vol. 3, pp. 1439–1461, 2003.
- [155] K. Zhi, C. Pan, H. Ren, K. K. Chai, and M. ElKashlan, “Active RIS versus passive RIS: Which is superior with the same power budget?” *IEEE Commun. Lett.*, vol. 26, no. 5, pp. 1150–1154, Mar. 2022.

List of Publications

Patent:

1. **V.B. Shukla** and V. Bhatia “System for Channel Estimation and Method Thereof” Indian Patent application No. 202421031952, Apr. 2024.

Journal Papers:

1. **V.B. Shukla**, R. Mitra, O. Krejcar, V. Bhatia, and K. Choi “Performance Analysis of Sparse Channel Estimators for Millimeter Wave Hybrid MIMO Systems With Non-Ideal Hardware”, *IEEE Trans. Veh. Technol.*, vol. 72, no. 9, pp. 11913-11923, Sep. 2023. **DOI:** 10.1109/TVT.2023.3270240 [**Impact Factor - 6.8**].
2. **V.B. Shukla**, V. Bhatia, and K. Choi, “Cascaded Channel Estimator for IRS-Aided mmWave Hybrid MIMO System”, *IEEE Wireless Commun. Lett.*, vol. 13, no. 3, pp. 622-626, Mar. 2024. **DOI:** 10.1109/LWC.2023.3337289 [**Impact Factor - 6.3**].
3. **V.B. Shukla**, V. Bhatia, and K. Choi, “Estimation of Cascaded Sparse Channel for IRS-Assisted Millimeter Wave Hybrid MIMO System”, *IEEE Commun. Lett.*, pp. 1-1, Feb. 2024. **DOI:** 10.1109/LCOMM.2024.3370257 [**Impact Factor - 4.1**].
4. A. Sharma, **V.B. Shukla**, and V. Bhatia, “ZA-LMS based sparse channel estimator in multi-carrier VLC system,” *Photonic Net. Commun.*, vol. 47, no. 1, pp. 30-38, Feb. 2024. **DOI:** 10.1007/s11107-023-01009-w [**Impact Factor - 1.9**].
5. **V.B. Shukla**, V. Bhatia, and K. Choi, “Adaptive sparse channel estimator for IRS-assisted mmwave hybrid MIMO system,” *IEEE Tran. Cogn. Commun. Net.*, under major revision. [**Impact Factor - 8.6**].

6. **V.B. Shukla**, A. Sharma, and V. Bhatia, "ZA-LMS based Sparse Channel Estimator for Mobility-Impaired Multi-carrier VLC Systems," *IEEE Open J. Comm.*, submitted. [**Impact Factor - 7.9**].

Conference Papers:

1. **V.B. Shukla**, R. Mitra, and V. Bhatia, “Adaptive Sparse Aware Algorithm Based Channel Estimation for mmWave Hybrid MIMO System”, *IEEE Adv. Net. Telecommun. Syst. (ANTS)*, pp. 290-295, Dec. 2021. **DOI:**10.1109/ANTS52808.2021.9936938.
2. **V.B. Shukla**, R. Mitra, and V. Bhatia, “Millimeter Wave Hybrid MIMO System Channel Estimation Using Variable Step Size Zero Attracting LMS”, *IEEE International Conf. Signal Process. Commun. (SPCOM)*, pp. 1-5, Jul. 2022. **DOI:** 10.1109/SPCOM55316.2022.9840854.
3. **V.B. Shukla** and V. Bhatia, “Variable Step-size Zero Attractor LMS based Channel Estimator for Millimeter Wave Hybrid MIMO System with Hardware Impairments”, *National Conf. Commun. (NCC)*, pp. 1-6, Mar. 2023. **DOI:** 10.1109/NCC56989.2023.10067962.
4. **V.B. Shukla**, A. Kaushik, and V. Bhatia, “Channel estimation and hybrid precoding design for joint radar communication”, *IEEE Adv. Net. Telecommun. Syst. (ANTS)*, pp. 1-6, Mar. 2024. **DOI:**10.1109/ANTS59832.2023.10469408.
5. A. Sharma, **V.B. Shukla**, and V. Bhatia, “ZA-LMS based Sparse Channel Estimator for VLC-OTFS”, *IEEE Adv. Net. Telecommun. Syst. (ANTS) WIE*, pp. 1-6, Dec. 2022. **DOI:** 10.1109/ANTS56424.2022.10227775.
6. J. Dsouza, **V.B. Shukla**, V. Bhatia, and S.K. Pandey, “Enhancing Classification of Traffic Sign using Multi-Technique Data Augmentation”, *IEEE 7th Conf. Inf. Commun. Technol. (CICT)*, pp. 1-6, Mar. 2024. **DOI:** 10.1109/CICT59886.2023.10455608.
7. S. Jain, P. K. Singya, **V.B. Shukla**, S. Majhi, and V. Bhatia, “Nonlinear Sparse Channel Estimator for Hybrid MIMO Millimeter Wave Communication”, *IEEE Personal, Indoor and Mobile Radio Commun. (PIMRC)*, pp. 1-6, Apr. 2024, Accepted.